FATIGUE MECHANISMS UNDER THE LOW AND HIGH CYCLE FATIGUE REGIMES IN NICKEL MICROBEAMS UNDER EXTREME STRESS GRADIENTS

A Dissertation
Presented to
The Academic Faculty

by

Alejandro Barrios

In Partial Fulfillment
of the Requirements for the Degree
Doctor of Philosophy in the
George W. Woodruff School of Mechanical Engineering

Georgia Institute of Technology
August 2020

FATIGUE MECHANISMS UNDER THE LOW AND HIGH CYCLE FATIGUE REGIMES IN NICKEL MICROBEAMS UNDER EXTREME STRESS GRADIENTS

Approved by:

Dr. Olivier N. Pierron, Advisor
George W. Woodruff School of
Mechanical Engineering
Georgia Institute of Technology

Dr. Richard W. Neu
George W. Woodruff School of
Mechanical Engineering
Georgia Institute of Technology

Dr. Shuman Xia
George W. Woodruff School of
Mechanical Engineering
Georgia Institute of Technology

Dr. Josh Kacher
School of Materials Science and
Engineering
Georgia Institute of Technology

Dr. Gustavo M. Castelluccio
Cranfield University

Date Approved: August 10, 2020

To my family

ACKNOWLEDGEMENTS

I want to thank my past and current lab mates: Dr. Kyungjin Kim, Dr. Saurabh Gupta, Gabe Cahn and Sandra Stangebye. Saurabh was a mentor at the start of my PhD and I thank him for our long and valuable research discussions.

Additionally, I would like to sincerely thank all friends I have made during these past years who gave me their full support, especially Esteban, Sam, Alex, Patrick, Antonio, David, Mike, Gaurav, Hemanth and many others who walked along with me and helped me overcome any obstacle I faced. I also want to thank all other students with whom I have interacted and everyone from the GT Catholic Center who provided an indispensable environment for my spiritual growth these past years.

Lastly, I want to wholeheartedly thank my entire family for their immense patience, understanding and support. Especially my parents, Enrique and Diana, and my siblings, Enrique, Daniela and Fernando, for their unconditional love and unwavering support to reach my goals.

Totus tuus ego sum, et omnia mea tua sunt

TABLE OF CONTENTS

LIST OF TABLES

LIST OF FIGURES

xii

LIST OF SYMBOLS AND ABBREVIATIONS

Abbreviations

MEMS	Microelectromechanical Systems
HCF	High Cycle Fatigue
VHCF	Very High Cycle Fatigue
SEM	Scanning Electron Microscope
FIB	Focused Ion Beam
EBSD	Electron Backscatter Diffraction
LCF	Low Cycle Fatigue
S-N	Stress-Life Curve
PSB	Persistent Slip Bands
FE	Finite Elements
EDS	Energy-dispersive X-ray Spectroscopy
UFG	Ultrafine Grained
IPF	Inverse Pole Figure

Symbols

η	Stress gradient
f_o	Resonance frequency
θ_o	Angle of rotation of resonator
σ_a	Maximum stress amplitude of the microbeam
ε_a	Maximum strain amplitude of the microbeam
ε_{pa}	Maximum plastic strain amplitude of the microbeam
N_f	Fatigue life, cycles to reach failure threshold
b	Basquin coefficient
c	Coffin Manson coefficient

SUMMARY

In the past years, fatigue investigations of micro- and nanoscale structural metals have become of great significance due to the prominent and extensive use of microelectromechanical systems (MEMS) and metallic thin films. Many MEMS and thin films consist of movable small-scale components that are subjected to a large number of loading cycles throughout their lifetimes and exhibit a strong influence from size effects that deviates their behavior from bulk size materials. Therefore, there is a need to investigate and understand the fatigue behavior and properties of small-scale metals under loading conditions relevant to their applications. This dissertation investigates the fatigue behavior of Ni microbeams subjected to size effects (extreme stress/strain gradients and microstructurally small cracks) under fully reversed loadings.

A previously reported microresonator technique used to investigate the High Cycle/Very High Cycle Fatigue (HCF/VHCF) regime of the microbeams was adapted to run *in situ* scanning electron microscope (SEM) fatigue tests. The *in situ* tests consist of MEMS microresonators that are driven at resonance inside the SEM at a frequency of ~8 kHz. The stress-life fatigue curve obtained inside the SEM (vacuum conditions) highlights over three orders of magnitude increase in fatigue life with respect to the fatigue curve obtained in laboratory air. The average crack propagation rates on the surface of the microbeam are extremely low and of the order of 10^{-12} m/cycle in air and 10^{-14} m/cycle in vacuum. Focused Ion Beam (FIB) cross-sections revealed that the nanoscale fatigue mechanism in the HCF/VHCF regime does not follow the conventional mechanism of crack tip stress intensification. Instead, the nucleation and propagation mechanisms are

controlled by the nucleation of voids (resulting from vacancy condensation processes) underneath extrusions or ahead of the crack tip. Electron backscatter diffraction (EBSD) revealed the transgranular nature of the voids associated with transgranular cracking. This void dominated fatigue mechanism is a consequence of the reduction in driving force for crack growth caused by the effects of extreme stress gradients. Therefore, the loading conditions applied in HCF/VHCF are below a threshold limit for the conventional mechanisms to operate.

In order to investigate the Low Cycle Fatigue (LCF) behavior of the Ni microbeams, a micromechanical external actuation technique was developed to test microbeams at higher applied strain amplitudes and lower fatigue lives. Results highlight significant differences in the slope of stress and strain-life behavior (Basquin's coefficient $b = -0.078$ and Coffin Manson coefficient $c = -0.57$ for LCF and $b = -0.038$ and $c = -0.30$ for HCF/VHCF) and crack propagation rates that differ from an average of 10^{-12} m/cycle in HCF/VHCF to an average of 10^{-8} m/cycle in LCF. Frequency effects were investigated contrasting the microresonator technique with the external actuation technique (8 kHz and 0.5 Hz, respectively), highlighting no frequency effects in microbeams tested at a similar stress/strain. These results, in addition to FIB cross-sections, suggest that the mechanisms follow the conventional mechanisms of crack tip stress intensification in the LCF regime, which is in stark contrast to the void controlled mechanisms in the HCF/VHCF regime. Additionally, these results demonstrate that the transition in governing mechanisms from void controlled to conventional mechanisms is highly influenced by the size effects present in the microbeams. Therefore, the application of larger strains

amplitudes (larger driving force) to these microbeams results in a transition in the governing fatigue mechanisms to the conventional fatigue mechanisms.

This dissertation also presents the investigation of fatigue-induced grain coarsening in the ultrafine grained region of the Ni microbeams (bottom 2.5 µm). EBSD tomographies reveal that microbeams which exhibit a (001) texture microstructure show abnormal grain growth after fatigue tests conducted at maximum strain amplitudes ranging from 0.18 to 0.85% and cycles ranging from 10^3 to 10^8. Results highlight cycle dependent growth of grains which exhibit a near (001) orientation along the microbeam's length direction and average grain growth rates ranging from 10^{-4} to 1 nm/cycle. Finite Element Simulations of synthetic models of the same microstructure reveal that the main driving force for grain growth is the reduction in elastic strain energy, although the strain energy density of the coarser grains is not at the minimum. Additionally, the apparent Schmid factor of the coarser grains tends to be larger suggesting that plastic deformation enables grain growth.

CHAPTER 1.   BACKGROUND AND MOTIVATION

1.1   Introduction and Motivation

Over the past 30 years, the study of the fatigue behavior of small-scale materials has become of great importance due to the technological drive to transition from bulk traditional engineering structures to micro/nano structures [1-3]. Many of these micrometer-scale structures and metallic films have been prominently used in recent years and encompass a wide range of applications. For example, microelectromechanical systems (MEMS) have been used as a variety of sensors, ranging from accelerometers and gyroscopes to biotechnology and chemical sensors [3-8]. More specifically, fatigue failure is of paramount importance to these structures due to the high number of movable components that are exposed to repeated loadings for a great number of cycles.

Silicon is the main structural material employed in commercial MEMS devices, although it is very brittle (fracture toughness around 1 MPa m$^{1/2}$). However, due to the increasing demand for the usage of MEMS in more rigorous environments, such as high temperature environments (Figure 1.1a) [4], other structural materials, including metals, are likely to be widely used in the near future, especially where brittle materials may not be suitable [4, 9]. For example, metallic MEMS films, such as the one shown in Figure 1.1b, with an excellent thermal and mechanical stability were recently synthesized, and are promising candidates for the next generation of metal MEMS devices [4, 10].

Fatigue mechanisms in bulk materials are mostly well understood [11, 12] but small-scale materials exhibit a particular behavior due to the presence of size effects. Hence, more advanced and specific techniques are needed to study their fatigue behavior.

In addition, the quantitative evaluation of the reliability of metallic microcomponents under different conditions is imperative for the design of MEMS

Therefore, new studies are required to characterize the fatigue damage and its size effects at the nanoscale in metallic microcomponents under cyclic mechanical loadings conditions relevant to MEMS devices. It is necessary to investigate the influence of environment and of applied loadings in the fatigue behavior of metallic MEMS. Furthermore, it is important to understand the underlying physical mechanisms that produce fatigue damage in order to design processing and application procedures to increase the reliability and the fatigue life of such devices.
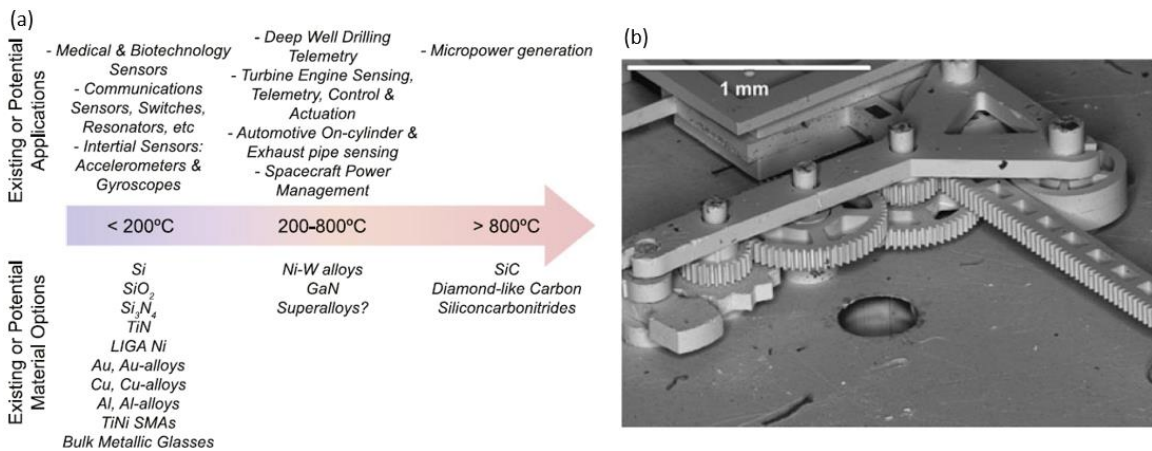
Figure 1.1 – (a) MEMS materials and application for rigorous environments; (b) Example of a metallic MEMS [4]

1.2   Background Information

1.2.1   Classical Fatigue Behavior and Mechanisms

Total life fatigue behavior studies are generally summarized in a stress or strain-life curve (S-N curves), such as the one shown in Figure 1.2a. The figure highlights two points along the curve: one in the Low Cycle Fatigue (LCF) regime, where stresses are

high enough to cause plastic deformation, and another in the High Cycle Fatigue (HCF) regime, where stresses are low and the material mainly deforms elastically. Fatigue lives are usually divided into two terms, the initiation life (N_i) and propagation life (N_p). As demonstrated in the figure, in LCF, the fatigue life is dominated by N_p (shown by the green rectangle) while having a relatively short N_i (yellow rectangle) and in HCF, the life is dominated by N_i while having a relatively short N_p [12, 13].
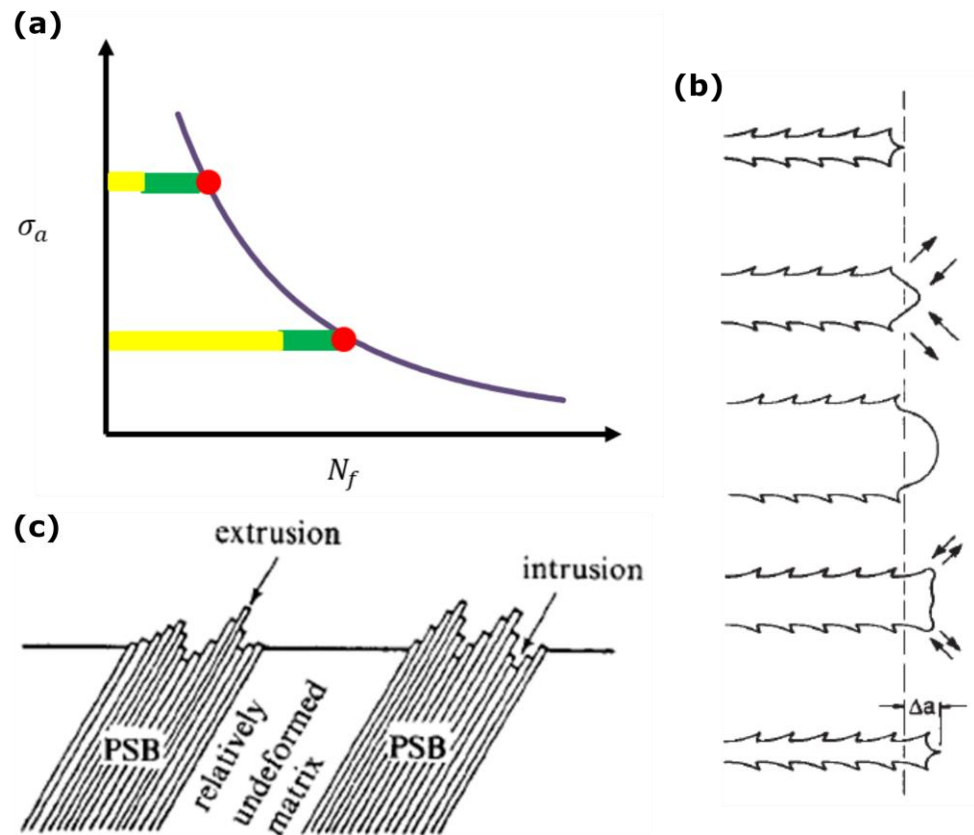
Figure 1.2 – (a) S-N fatigue behavior; (b) Classical fatigue crack initiation mechanisms [12]; (c) Classical fatigue crack propagation mechanisms [13]

Classical fatigue initiation mechanisms in ductile metals are mediated through the roughening of the free surface in the form of extrusion/intrusions caused by irreversible deformations (microplasticity) along Persistent Slip Bands (PSB), as shown in Figure 1.2c. The repeated cyclic straining causes the irreversible slip-unslip that, in turn, causes

stress/strain concentration effects near PSBs, facilitating fatigue crack nucleation. One of the most used theories for the origin of irreversibilities is the generation of many vacancies caused by the annihilation of dislocations gliding along the PSBs [12, 14].

Fatigue propagation mechanisms are usually characterized by crack tip opening displacements (CTOD) caused the opening and blunting of the crack tip followed by the resharpening of the tip, as shown in Figure 1.2b. The localized deformation caused by the slip along the plastic zone around the crack causes the crack to extend and become blunt as the maximum load is applied. Then, the crack is resharpened as the applied load is decreased. Crack growth is highly influenced by the stress concentration effects at the crack tip during cyclic loadings [13, 15].

1.2.2   *Size effects (Stress gradients and microstructurally small cracks)*

Normalized stress gradients are calculated by Equation 1.1. Typical values for these stress gradients in bulk materials under bending are about 10% mm^{-1} (a 10% decrease in stress for every millimeter away from the free surface). In the presence of sharp notches in bulk materials, the stress gradients are of the order of 1-2% μm^{-1} [16, 17] and the fatigue behavior of such structures is mostly well understood [12]. However, the stress gradients experienced by microscale structures can be about an order of magnitude larger (extreme stress gradients) under bending and can have a great influence on the fatigue properties and mechanisms. Many studies have investigated size effects in the fatigue of microscale structures but the majority of them utilized micro-tensile fatigue tests to understand the influence of grain size and specimen thickness on the fatigue properties and mechanisms under the absence of extreme stress gradients [18-22]. More recent studies have explored the fatigue behavior in microbeams under extreme stress gradients [9, 23, 24], using

4

bending loadings which are more appropriate to certain applications of MEMS devices. The extreme stress gradients have a great influence in the crack propagation rates and fatigue lives since they decrease the driving force for crack extension and possibly arrest cracks.

$$\eta = \frac{1}{\sigma}\frac{d\sigma}{dx}$$
Equation 1.1

Another factor that contributes to the changes in the fatigue behavior of small-scale components is that only microstructurally small cracks are present due to the limited dimensions of the components. These cracks are about the same order of magnitude of the microstructure's characteristic length, and present a very particular behavior that cannot be analyzed with linear elastic fracture mechanics (LEFM) nor with the elastic plastic fracture mechanics (EPFM) frameworks. Fatigue crack growth is generally divided into two groups: Stage I crack growth, which correspond to microstructurally small cracks, and Stage II crack growth, which correspond to long cracks that cover many grains. Stage I cracks do not follow the conventional fatigue mechanisms and have non uniform crack growth rates [25], while Stage II cracks usually follow the conventional fatigue behavior and mechanisms highlighted in Section 1.2.1.

Figure 1.3 demonstrates the crack growth behavior of Stage I and Stage II cracks in the absence of stress gradients. Small cracks exhibit much faster growth rates compared to long cracks (propagation rates of the order of 10^{-9} m/s to 10^{-6} m/s) that decrease with increasing crack size [26]. The decreasing rates are explained by the absence of crack closure effects and by the interaction of the crack tip with barriers along the crack path such as grain boundaries [27].
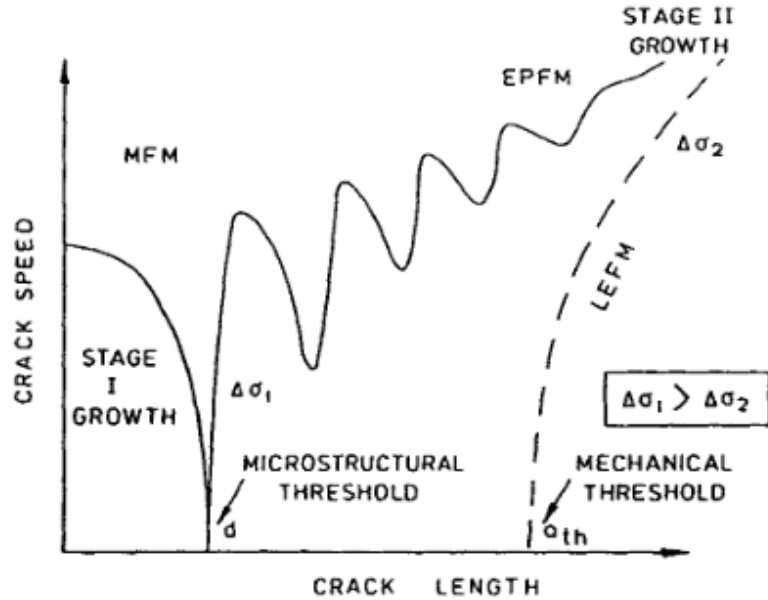
Figure 1.3 – Crack growth of stage I and stage II cracks for $\eta = 0\%$ μm^{-1} [25]

Therefore, both the extreme stress gradients and the microstructurally small cracks highly influence the fatigue behavior of MEMS and more advanced micro and nanomechanical techniques must be developed to investigate these size effects in microcomponents in conditions relevant to their applications.

1.2.3 Review of Micro Scale Behavior in Nickel Thin Films

Among the metallic materials used in the MEMS industry, Nickel is one most widely used ones for rigorous applications, as it has good ductility and fracture toughness. Generally, electrodeposited Ni thin films are used as the mechanical components in MEMS which can sustain a high number of cycles throughout their lifetime. The usage of Ni electrodeposition as a fabrication method allows for the creation of structures which have high strength and high aspect ratio.

Previous investigations have studied the fatigue behavior of Nickel thin films under tensile fatigue to study several size effects. Yang *et al.* developed a tensile fatigue technique

6

to study microstructurally small cracks that nucleate at notches in Ni thin films. They have found that the microstructure plays an important role in the stress-life behavior of Ni MEMS by raising the endurance limit and the MEMS fatigue life when the grain size is decreased from 270 μm to 70 μm [18]. The same research group also reports that fatigue crack propagation mechanisms in these thin films demonstrate large amounts of plastic deformation even at low stresses [19]. Cho *et al.* have investigated the tensile S-N curves of Nickel thin films. They addressed how the decrease in sample width further decrease the mechanical strength and fatigue resistance of the Ni micro specimens [20]. Additional investigations have looked at the fatigue resistance and crack growth behavior as a function of the Ni microstructure grain size and concluded that in general, grain refinement increases the fatigue live of the Ni samples [21, 22].

Even though a great number of these studies have investigated the size effects of grain size and growth of microstructurally small cracks, they have not observed how fatigue properties and mechanisms change under conditions more relevant to certain MEMS applications which experience the effects of extreme stress gradients.

Boyce *et al.* have examined the high cycle behavior of a Ni micro cantilever beam with extreme stress gradients. They utilized a servohydraulic load frame to apply a fully reversed bending loading to the beam and that allowed them to run displacement control fatigue tests [9]. They reported a high cycle fatigue behavior that had similar trends as to that of bulk Ni asserting that there were no perceivable size scale effects in the Ni beam that possessed a stress gradient of about $\eta = 7\%$, although some effect would be expected. They also investigated the role of oxygen in slip band crack initiation during fatigue loading, highlighting that environmental effects are important to the study of MEMS under

fatigue loadings. They asserted that oxygen present in the environment affects crack initiation because of the formation of brittle oxides on slip band surfaces [9]. Baumert *et al.* have also studied a similar oxygen assisted fatigue crack initiation mechanisms in Ni microbeams under extreme stress gradients, highlighting the coupled size and environmental effects [28, 29].

1.2.4 Review of High and Very High Cycle Fatigue of Ni microbeams under bending

Pierron's research group has developed an electrostatic resonance technique to extensively study the High and Very High Cycle Fatigue (HCF/VHCF) behavior of Ni microbeams under bending loadings. The technique is described in more detail in Section 2.2. During a fatigue test, these microbeams experience extreme stress gradients and exhibit microstructurally small cracks once fatigue damage develops.

Baumert and Pierron first introduced the resonance technique and studied the fatigue damage evolution, which can be correlated with the decrease in resonance frequency (f_o), in a notched microbeam with an extreme stress gradient of $\eta = 36\%$. They studied non-propagating cracks and possible mechanisms for crack initiation. The fatigue damage could be evaluated with the Scanning Electron Microcopy (SEM) *postmortem* analysis of the extrusion/intrusion at the microbeams' sidewalls [28]. Sadeghi-Tohidi and Pierron have studied the fatigue crack propagation in Ni microbeams under extreme stress gradients utilizing the same HCF/VHCF technique. They used a combination of experimental and a 2D Finite Elements (FE) model to calculate the crack growth rates of two different beam geometries, one unnotched with $\eta = 17\%$ μm^{-1} and a second notched beam with $\eta = 50\%$ μm^{-1} and under two environments, a mild (30 °C, 50% RH) and a harsh (80 °C, 90% RH) environments. Figure 1.4 shows the results of the fatigue damage

and f_o decrease of some of tested specimens. They calculated average rates that are extremely small (from 10^{-15} to 10^{-11} m/cycle) with faster rates for the samples with the smaller stress gradients and little influence of the studied environments. They postulated that the extreme stress gradients are likely to cause the ultra-slow propagation rates [23].
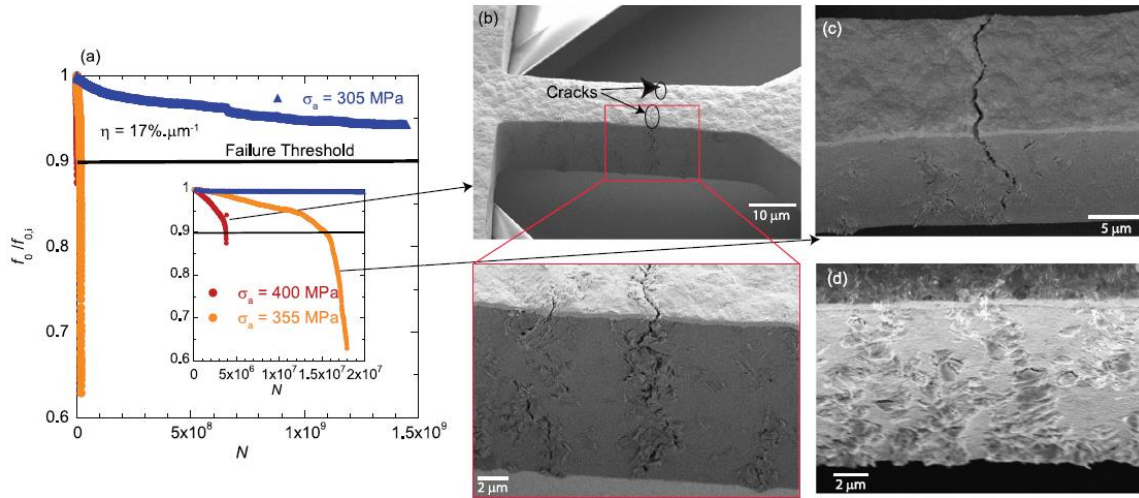
Figure 1.4 – Frequency evolution curve and *postmortem* SEM images of microbeams tested in the HCF/VHCF regime [23]

They have also studied the VHCF fatigue life and behavior of notched microbeams with $\eta = 36\%$ µm^{-1} under the environments highlighted above. They report samples with extensive fatigue damage along the notch root with extrusions/intrusions and 3D stage I cracks that form 2D cracks as the damage increases [30]. The extrusion height, measured from SEM images, of samples ran in the harsh environments are higher and are possibly explained by the formation of thicker oxides along slip bands [29]. In addition, a higher concentration of oxygen in EDS scans is observed along the fatigue damage in these regions. Another possible explanation for these observations is the nucleation of voids rich in oxygen. They reported that the fatigue limit of these notched microbeams is about 450 MPa, significantly larger than in bulk Ni, and that the fatigue curves have unusually low

Basquin and Coffin-Manson coefficients. They also observed that the change of environment from mild to harsh has little effect on the fatigue life of the microbeams. In addition, they investigated the crack propagation rates using the same 2D FE model and found similar ultra-slow propagation rates that decrease with increasing crack size. The extreme stress gradients not only play a role in reducing the crack growth rate but also on deaccelerating the crack rate as the crack increases [30].

Furthermore, Sadeghi-Tohidi and Pierron have compared the effect of HCF/VHCF fatigue life and crack propagation rates of two different normalized extreme stress gradients on a notched microbeam of $\eta = 36\%$ μm^{-1} and on an unnotched beam of $\eta = 17\%$ μm^{-1}. They again reported ultraslow propagation rates, shallow stress-life curves and little difference of fatigue life in harsh and mild environments for each stress gradient. The fatigue life of microbeams with $\eta = 36\%$ μm^{-1} was three orders of magnitude higher than microbeams with $\eta = 17\%$ μm^{-1} for a particular stress or strain amplitude (shown in Figure 1.5a and b), highlighting the significant role that extreme stress gradients play on the propagation of microstructurally small cracks. They also reported about an order of magnitude higher propagation rates in the $\eta = 17\%$ μm^{-1} stress gradient (Figure 1.5c and d). They highlighted the need to run *in situ* SEM tests in vacuum conditions to have a better understanding of the effects of the environment in the fatigue mechanisms [31].
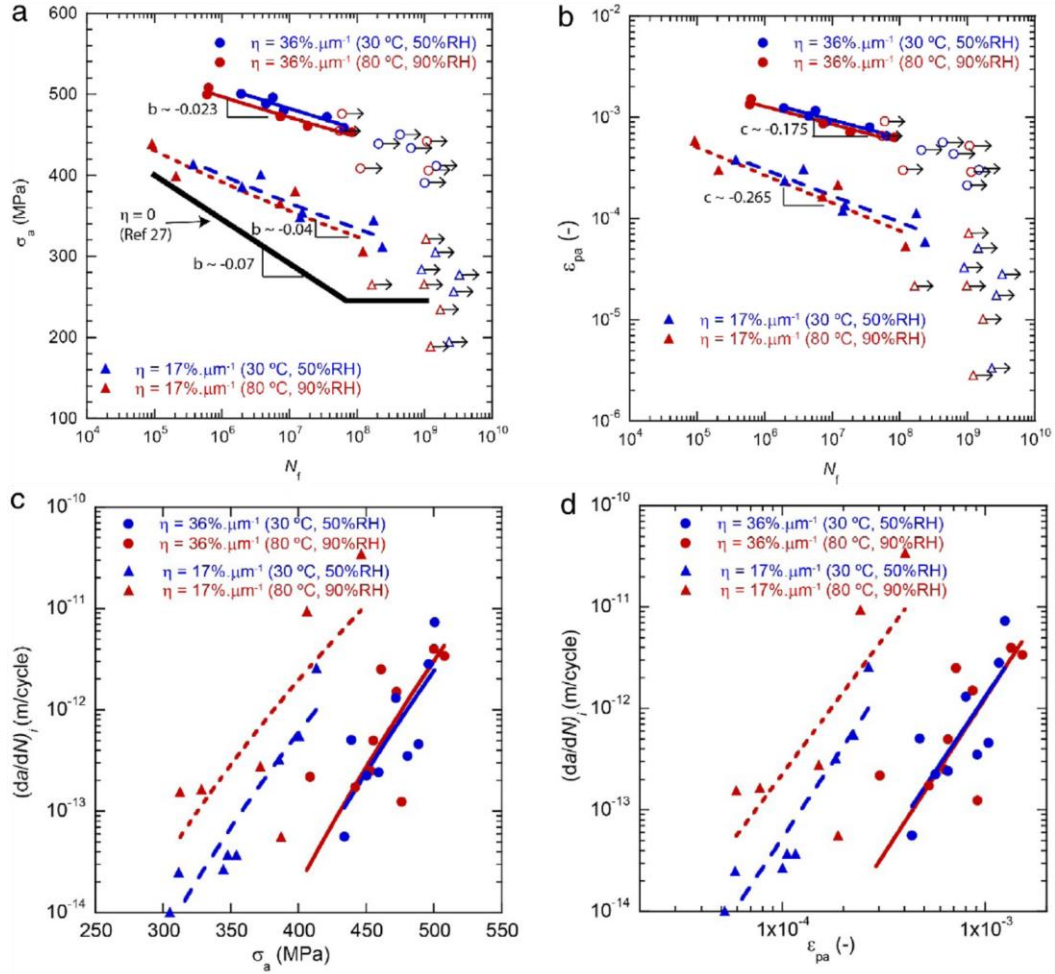
Figure 1.5 – (a) S-N curves and (b) plastic strain amplitude vs cycles curves of Ni microbeams for η = 17 and 36% μm^{-1}; Calculated crack propagation rates as a function of (c) stress amplitude and (d) plastic strain amplitude [31]

1.3   Scope of Present Work: Objectives and Governing Hypothesis

The study of fatigue behavior of small-scale metals is of great importance. Many techniques have been adopted to study size effects in Ni, mostly focusing on the effects of grain size, sample width and the growth of microstructurally small cracks [18-22]. However, fewer studies have investigated the combination of effects of extreme stress gradients and microstructurally small cracks in the fatigue behavior of Ni micrometer-scale structures [23, 28-31]. These effects are widely present in many MEMS applications (for

example, any application that involves repeated bending loadings) and, therefore, there is a need to characterize the fatigue damage and mechanisms under these size effects.

The main objective of this work is to understand the underlying nanoscale crack nucleation and propagation mechanisms of microstructurally small cracks in Ni microbeams under extreme stress gradients at the High Cycle Fatigue and Low Cycle Fatigue regimes. Based on previous results showing ultraslow crack propagation rates, we hypothesize that the extreme stress gradients greatly reduce the driving force for fatigue crack growth, causing the unusual fatigue behavior in the HCF/VHCF. However, the application of a larger driving force (higher strain amplitudes) in the LCF regime is expected to change the fatigue behavior of the microbeams and reduce the influence of the extreme stress gradients.

Therefore, this work investigates the mechanisms, fatigue behavior (S-N curves, propagation rates) and the fatigue crack characteristics (intergranular or transgranular) in the two regimes. Additionally, environmental effects are investigated in the HCF/VHCF regime, while frequency effects are investigated by tracing comparisons of tests performed at significantly different frequencies. Lastly, fatigue-induced grain coarsening is observed and studied in the ultrafine grained region of the microbeam.

Hence, this work is divided into three main chapters:

i. High and Very High Cycle Fatigue Behavior

In chapter 3, this thesis explores the use of an existing microresonator technique for HCF/VHCF and its adaptation to run *in situ* Scanning Electron Microscopy (SEM) fatigue tests. Through *in situ* SEM testing, unprecedented levels of detail on fatigue damage are

observed and the role of the environment on fatigue damage and life is investigated. The fatigue behavior, properties and the average propagation rates are also investigated with the *in situ* technique. Additionally, Focused Ion Beam (FIB) cross sections are performed in order to evaluate the fatigue crack nucleation and propagation mechanisms in this regime. Finally, fatigue crack path characteristics are investigated with 3D Electron Backscatter Diffraction (EBSD) scans.

ii. Low Cycle Fatigue Behavior

The mechanisms found in the HCF/VHCF contrasted the conventional fatigue mechanisms and therefore, the previous results led to infer that tests were done below a threshold limit for the conventional mechanisms to act. In chapter 4, this work explores the design of a technique for LCF (higher strain amplitudes) to investigate propagation mechanisms, crack propagation rates and fatigue behavior in this regime. Frequency effects are also explored by comparing samples ran at similar stress amplitude ranges but at different frequencies (8 kHz and 0.5 Hz) and 3D EBSD scans were also performed.

iii. Fatigue-Induced Grain Growth

Chapter 5 explores the grain coarsening in the ultrafine grained region of the microbeam (bottom 1.5 µm) under cyclic bending loadings. The *postmortem* EBSD scans gathered from the 3D EBSD procedure allowed for the characterization of grain size and orientations in this region of the microbeam. Results highlight abnormal grain coarsening in samples tested over strain amplitudes ε_a ranging from 0.15 to 0.85 % and fatigue lives ranging from 10^2 to 10^9. This chapter also explores the origins of the thermodynamics driving force and kinetics of this fatigue driven grain growth.

CHAPTER 2.   EXPERIMENTAL PROCEDURES

This chapter presents the experimental samples and techniques used in the study of the fatigue properties and behavior of small-scale metallic components under extreme stress gradients. In addition, the chapter presents fractography and microstructural characterization techniques for the in-depth study of nanoscale fatigue mechanisms and microstructural variation along the fatigue crack paths.

2.1   Microresonators and Microbeam Description

The MEMS microresonator used in this study is shown in Figure 2.1(a) and consists of a free-standing Ni microbeam fixed to the substrate on one side and connected to two arms of interdigitated fingers (comb structures) on the other side. These microresonators were originally designed for the study of HCF/VHCF and to be actuated at their resonance frequency (~8 kHz).
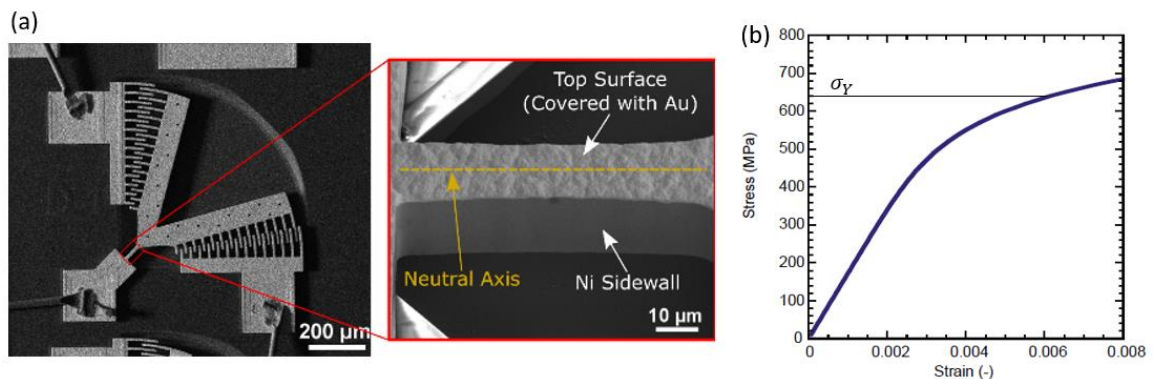
Figure 2.1 – (a) Microresonator and microbeam [32]; (b) Monotonic stress-strain curve for electroplated Ni [30]

These devices were fabricated with the MetalMUMPs process from MEMSCAP [33]. The microresonator is composed of Ni and possesses a ~0.5-µm thick Au layer on the

14

top and a ~0.5-μm thick Cu layer on the bottom [28]. Although the presence of the Au layer makes the top surface rough, the sidewall of the microbeam (where fatigue damages accumulates) has negligible surface roughness. The electroplating was performed using a conventional, additive-free sulphamate bath (including 405 g/L nickel sulfamate, 7.5 g/L nickel bromide, 97.5 g/L nickel, 37 g/L boric acid) at 30°C, pH = 4, using a direct current (DC) density of 20 mA/cm^2 [34-37].

The electroplated Ni microbeam has a columnar microstructure, with a grain height of 5-10 μm and a diameter of approximately 1−2 μm with equiaxed grains in between columnar grains, and a strong (001) out of plane texture [31]. The microstructure varies along the thickness of the microbeam, starting with an ultrafine grained region in the bottom 1.5 μm (See Section 2.6) and exhibiting the columnar grains in the top. The mechanical monotonic tensile properties have been previously measured using microtensile tests of dog bone shaped specimens, are summarized in Table 2.1 and the stress-strain curve is shown in Figure 2.1b [28]. The microbeam has dimensions of approximately $60 \times 12 \times 20$ μm and exhibits a normalized stress/strain gradient of $\eta = 17\%$ μm^{-1}.

Table 2.1 – Mechanical Properties from microtensile tests [28]

Mechanical Properties	Young's Modulus [GPa]	0.2% Yield Strength, σ_y [MPa]	Tensile Strength, σ_{UTS} [MPa]
Nickel thin film	166±19	656±70	873±26

2.2 Resonance fatigue tests and *in situ* SEM tests

The high cycle fatigue experimental procedure has been used extensively by Pierron and co-workers [23, 28, 30, 31, 38], and therefore only an overview will be presented here.

The microresonator allows for the electrostatic actuation through the comb structures (via a high sinusoidal input voltage) resulting in a cyclic in-plane fully reversed bending of the microbeam which is electrically grounded [31]. The actuation of the microresonator is dictated by its resonance frequency f_o (about 8 kHz) and, therefore, can be used to characterize the HCF/VHCF behavior of microscale materials, requiring about 3.5 h to accumulate 10^8 cycles [32] . The other set of comb structures is used as a sensing circuit through a capacitive current and allows for the identification of the device's resonance frequency. As the fatigue damage starts to develop in the microbeam's sidewalls in the form of extrusion/intrusion and cracks, the stiffness and, consequently, the resonance frequency decrease. The decrease in f_o is tracked periodically throughout a fatigue test and is used as a metric to define fatigue damage. An optical calibration is needed to measure the angle of rotation (θ_o) which, through Equation 2.1 (captured by FE models) [31], is related to the maximum stress amplitude (σ_a) that the microbeam exhibits at the sidewall during a fatigue test [30]. The optical calibration consists of measuring the distance between the edge of a comb's finger at rest (when no load is applied) and the edge of a comb's finger vibrating at the resonance frequency. In order to estimate the applied strain amplitude, the cyclic response was assumed to be similar to the monotonic response which was captured by microtensile tests, and fitted through Ramberg-Osgood's model, as shown

in Equation 2.2 with the properties in Table 2.2, where ε_{pa} is the plastic strain amplitude [30].

$$\sigma_a = 24.54 \times 10^3 \theta_o - 2.23 \times 10^5 \theta_o^2 \qquad \text{Equation 2.1}$$

$$\sigma_a = H\varepsilon_{pa}^n \qquad \text{Equation 2.2}$$

Table 2.2 – Parameters for Ramberg-Osgood's Equation [30]

Ramberg-Osgood Parameters	Strength Coefficient, H [MPa]	Strain Hardening Exponent, n
From Ni microtensile tests	1451	0.136

For the microbeams tested under this technique, the fatigue life, N_f, is defined as the number of cycles to reach a 10% decrease in f_o, which has been shown to correlate to a 2-µm-long crack on each side of the microbeam [23]. Unlike bulk ultrasonic fatigue testing, the small specimen size and large surface-to-volume ratio prevent any significant heating of the microbeam at resonance, which would be captured by a large measured reversible change in f_o (a 50 °C increase in temperature leads to a decrease in f_o of ∼1%) [28, 30]. This fatigue technique is therefore perfectly suited to investigate size effects relevant to the long-term reliability (HCF/VHCF) of small-scale metallic components, such as the nucleation and growth of microstructurally small fatigue cracks under extreme stress gradients [32].

This technique has been successfully adapted to perform HCF/VHCF fatigue tests inside a SEM thereby providing unprecedented levels of details regarding the fatigue damage of microbeams and a robust quantification of the role of air on the nucleation and growth of these small cracks [32]. The *in situ* SEM fatigue tests allow for a more in-depth

observation of the evolution of fatigue damage (fatigue crack formation and evolution of the crack shape along the sidewalls) throughout a fatigue experiment and its relation to the decrease in f_o, whereas the previous fatigue tests would mainly allow for *postmortem* SEM examinations [31]. The *in situ* SEM fatigue tests are performed in a FEI Nova Nanolab 200 FIB/SEM, using electrical feedthroughs to apply the electrostatic force onto the actuation comb drive, and to sense the induced current from the sensing comb (Figure 2.2a and b).
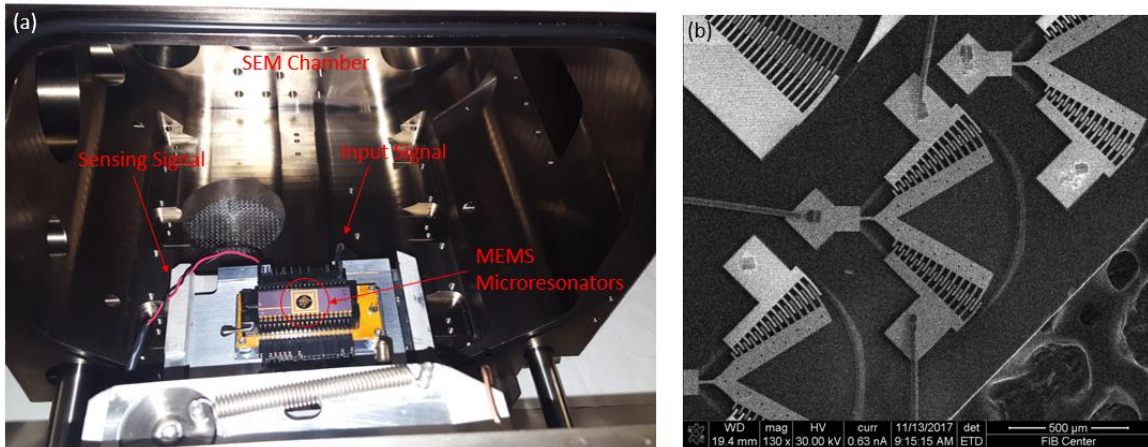
Figure 2.2 – (a) *In situ* SEM Fatigue Test Setup, (b) Microresonator being tested in vacuum

Figure 2.3 shows the frequency sweeps of two samples (one in air and another in vacuum) performed at the beginning of a fatigue test in order to find the f_o of the microresonators. As mentioned before, sweeps similar to the ones shown are repeated periodically throughout a fatigue test to keep track of the f_o evolution. f_o is highly dependent on the amplitude of the input voltage and there is usually a relatively small variation across samples, accounting for small variations on the dimensions of the microresonators. The figure shows the different voltage output responses for the two cases, highlighting the slight increase in quality factor, Q, for the frequency sweep ran in vacuum. The quality factor is calculated by Equation 2.3, where Δf represents the full width at half power (the amplitude

at half-power points is approximately 70.7% of the peak voltage response of the sweep curve) [28]. The slight increase in the microresonator's quality factor arises from the decrease in damping forces caused by the absence of air damping, although the quality factor is still dominated by dislocation damping at that range of input voltage amplitude [28, 32].
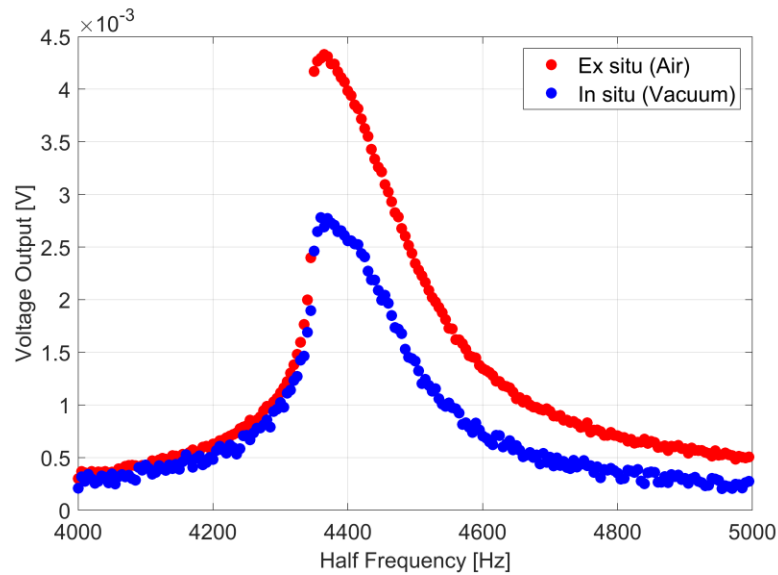
Figure 2.3 – Frequency sweeps for microresonators in air and in vacuum with a 200 V amplitude input voltage

$$Q = \frac{f_o}{\Delta f}$$
Equation 2.3

As mentioned before, an optical calibration is performed at the beginning of each fatigue test to find θ_o by measuring the distance traveled by the fingers. The input of a high voltage in the SEM causes the electron image to become blurry, adding some uncertainty to the θ_o measurement. The uncertainty is found by measuring the blur of the stationary combs in the SEM images, shown by the red arrow in Figure 2.4b, and typical values are around 1 mrad. The uncertainty in σ_a is ~20 MPa, based on the uncertainty in the angle of

rotation at resonance (see Figure 2.5a). Figures 2.5b and c provide the overall trend in the measured θ_o and corresponding σ_a (estimated from Equation 2.1), respectively, as a function of the amplitude of input voltage for all tests performed in air and vacuum. The larger values in vacuum (comparing from 200 to 300 V) result again from the slight increase in the microresonator's quality factor [32].
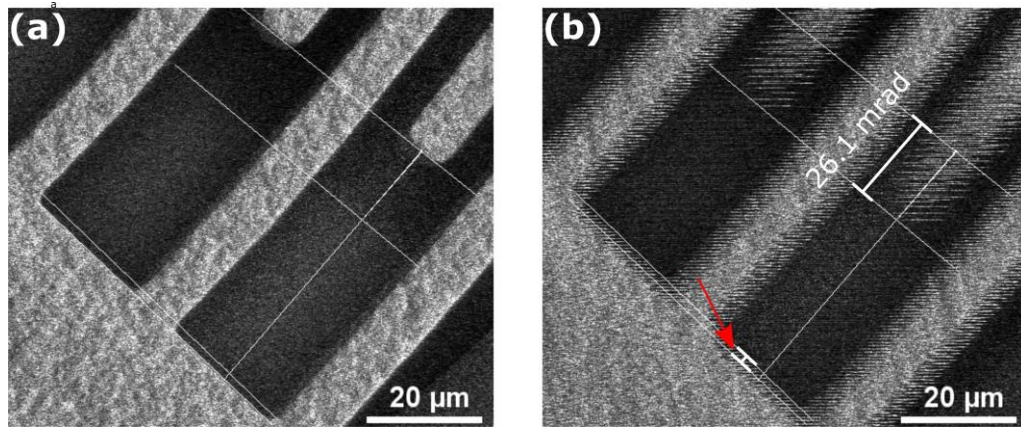
Figure 2.4 – SEM images of the combs for the optical calibration when the device is (a) at rest and (b) vibrating at its resonance frequency [32]

Due to limitations on the design of the microresonator and of the fatigue test ("fixed" resonance frequency of the microresonator, instrument ranges for input voltages), as well as the damping behavior of the resonators, this technique only allows for a maximum applied stress amplitude of about 500 MPa, equivalent maximum applied ε_a of about 0.3%, well below the yield stress of the material, and, consequently, low plastic strain amplitudes of $\varepsilon_{pa} < 10^{-3}$ [32]. Figure 2.6 demonstrates the ranges in applied strain amplitude, ε_a, in which the electrostatic technique can be applied. Therefore, in order to increase the applied ε_a to test metallic components at significantly higher ε_{pa} (above their yield strength) a new external actuation technique was developed.
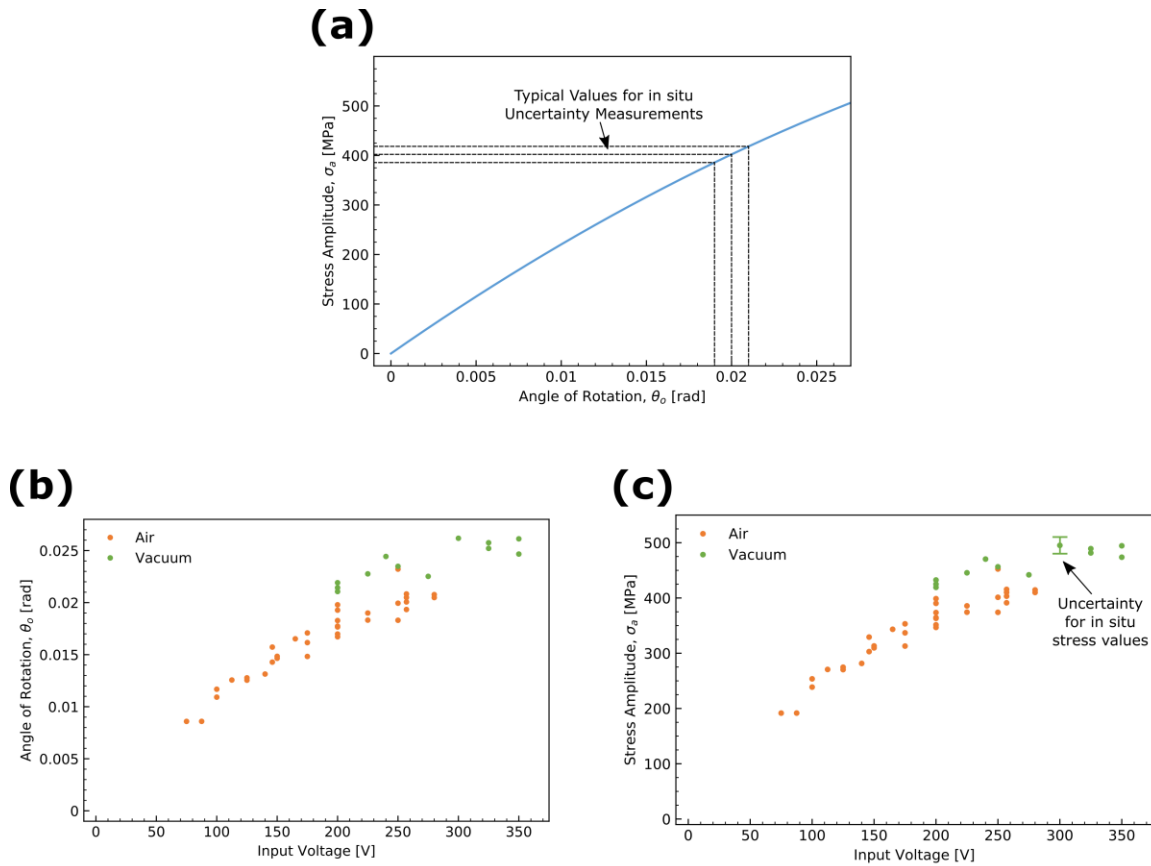
Figure 2.5 – (a) Finite element modeling relationship between angle of rotation and stress amplitude, highlighting the uncertainty for the *in situ* measurements; Relationship between input amplitude voltage and (b) the angle of rotation and (c) the stress amplitude of fatigue tests done in air and in vacuum
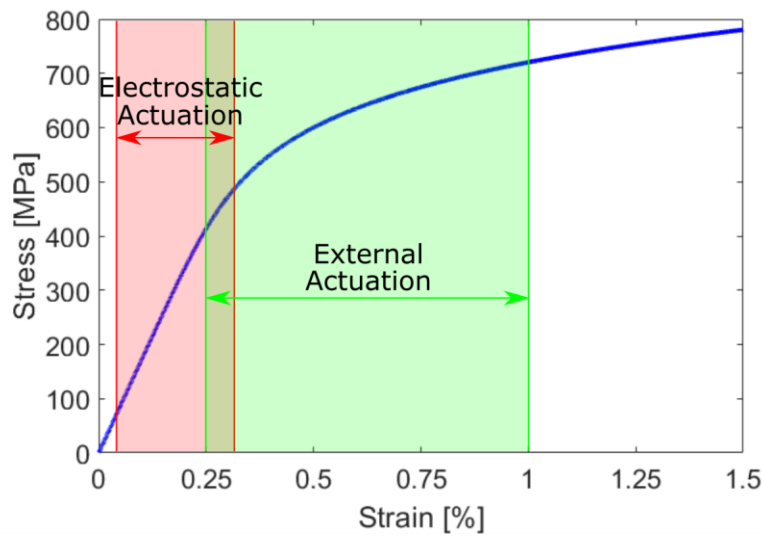
Figure 2.6 – Strain amplitude ranges for fatigue micromechanical techniques

2.3   External Actuation Tests

Since the electrostatic technique would only allow for nominally elastic loadings, a new technique was designed in order to study the fatigue behavior of the same microbeams at higher strain amplitudes under the LCF regime.

The external actuation system is depicted in Figure 2.7 and uses the same microresonator device described in Section 2.1. The setup consists of a piezoelectric X-direction positioning stage (PI P-611.1) that allows for movement in only one direction. The microresonator is mounted on top of the positioning stage and a Tungsten micromanipulator tip (~0.5 μm in diameter) is placed and centered between the arms of the microresonator using a manual XYZ positioning stage (Edmund Optics Positioning Stages). The micromanipulator is fixed in space and attached to a calibrated strain-gauge load cell (Transducer Techniques GSO-10) which allows for the measurement of the force required to displace the microresonator. The microresonator and micromanipulator are observed through an optical microscope for initial alignment.

The actuation of the microresonator consists of the input of a low sinusoidal voltage into a piezo servo controller (PI E-660) in order to actuate the piezoelectric positioning stage. Once the stage is actuated (along with the microresonator mounted on top), the micromanipulator comes into contact with one arm of the microresonator displacing it by a certain angle of rotation. As the voltage varies and the stage moves in the opposite direction, the micromanipulator releases contact with the arm and, after a short delay, contacts the second arm of the microresonator, also displacing it. Concurrently, the load cell measures the tensile force required to displace the first arm and the compressive force

required to displace the second arm. The actuation of the microresonator for half a cycle is

shown in Figure 2.8.
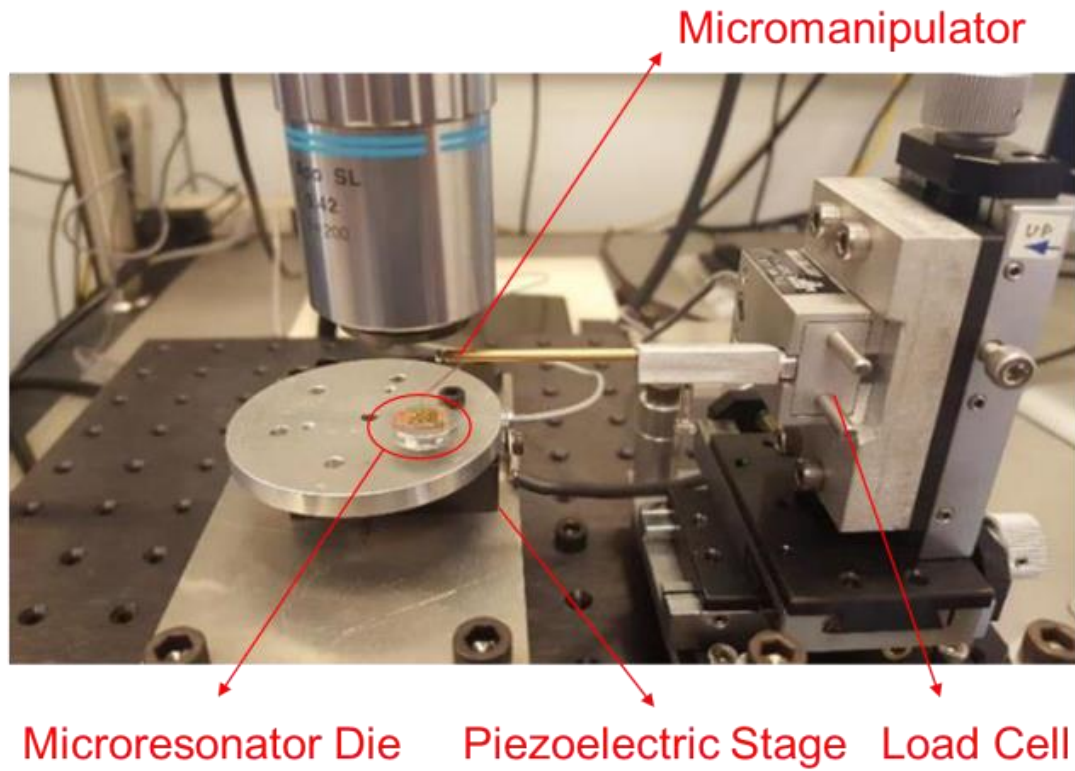
Figure 2.7 – Setup for external actuation technique
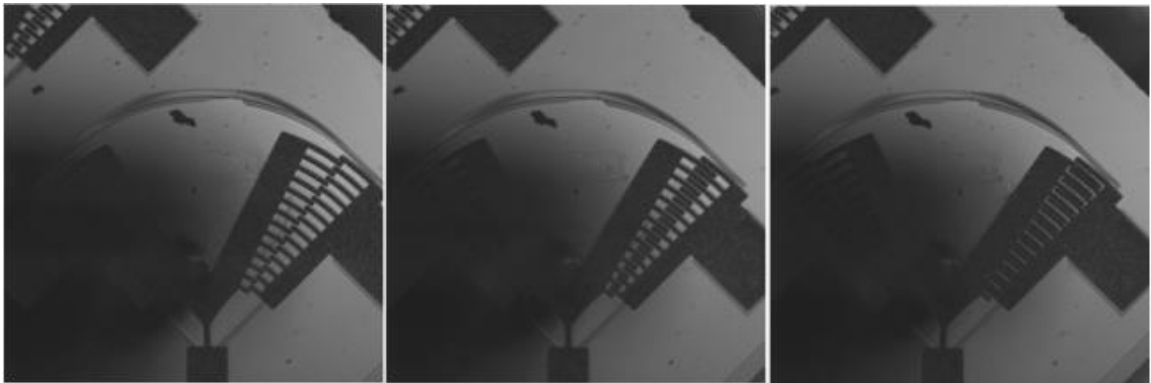
Figure 2.8 – Micromanipulator actuating the microresonator, causing bending fatigue at
the microbeam

Before a fatigue test is performed, a few cycles are conducted at a very low frequency and strain amplitude in order to properly align the micromanipulator with the microresonator and ensure symmetric bending loadings on the microbeam. Once a full cycle exhibits the same amplitude for the tensile and compressive forces, the fatigue test is performed at a frequency of 0.5 Hz and at a specified angle of rotation which is measured with the optical microscope (same optical calibration performed in the electrostatic technique) [30]. Therefore, the microbeam attached to the microresonator experiences fully reversed bending fatigue. As the fatigue damage starts to build in the microbeam, the stiffness and, consequently, the measured load amplitude required to displace the microresonator decrease, creating a metric to quantify fatigue damage. The fatigue life, N_f, is defined as the number of cycles to reach a 20% decrease in load amplitude (and therefore rotational stiffness k_θ), which is related to the resonance frequency f_o by Equation 2.3, where J_θ is the polar moment of inertia. Hence, a 20% decrease in stiffness is equivalent to a 10% decrease in resonance frequency which is the failure threshold used for the electrostatic technique [32]. The maximum stress and strain amplitudes experienced by the microbeam are then calculated from the measured angle of rotation through Equations 2.1 and 2.2 [30].

$$f_o = \frac{1}{2\pi}\sqrt{\frac{k_\theta}{J_\theta}}$$
<div align="right">Equation 2.4</div>

This technique allows for much higher applied ε_a up to an upper limit of about 1%, as shown in Figure 2.6. The limit is established by the maximum achievable angle of rotation restricted by the space between the fingers (See Figure 2.8). This allows for the investigation of metallic components under loadings pertaining to their nominally plastic

regime. Therefore, this technique is ideal to study the LCF of small-scale metallic components. The technique can also be used for different R-ratios and at different frequencies ranging from 0.01 Hz to about 200 Hz, although in the current study, only fully reversed loadings and a frequency of 0.5 Hz were used. Additionally, the external actuation allows for the study of the bending fatigue in microbeams at around $\varepsilon_a = 0.3\%$ with 0.5 Hz and comparison with microbeams tested at about the same ε_a but with ~8 kHz (electrostatic technique) in order to evaluate frequency effects.

2.4 Fractography (SEM, FIB cuts, FIB slices)

In order to understand the crack path and growth behavior of tested specimens, sub-surface observations are needed. FIB cross sections of specimens that only had extrusions/intrusions and others that had reached fatigue failure were performed for samples fatigued under the two techniques described above. These observations allow for the interpretation of the underlying physical mechanisms needed to nucleate and propagate a microstructurally small crack in the Ni microbeams.

A dual beam FIB/SEM (FEI Nova Nanolab 200) was used to characterize the extent of fatigue damage in the microbeams. Before the FIB cuts for cross-sectioning, a thin 1 µm layer of Pt was deposited in order to avoid damage to the area of interest and to avoid the curtaining effect from the FIB cut. The deposition was done at 30 kV a current of 0.3 nA. Rough milling of the microbeam with the ion beam was conducted at a current of 1 nA and polishing milling, at a current of 0.3 nA. Three different orientations of FIB cross-sections in relation to the microbeam were performed (vertical, horizontal and transverse) according to Figure 2.9 [32]. The vertical and transverse cuts were done with the microbeam still

25

attached to the base. For the horizontal cut, the microbeam itself was cut from the base and from the two arms and rotated using a manipulator. Then it was attached to the substrate using Pt and finally a FIB cross-section was performed [39].
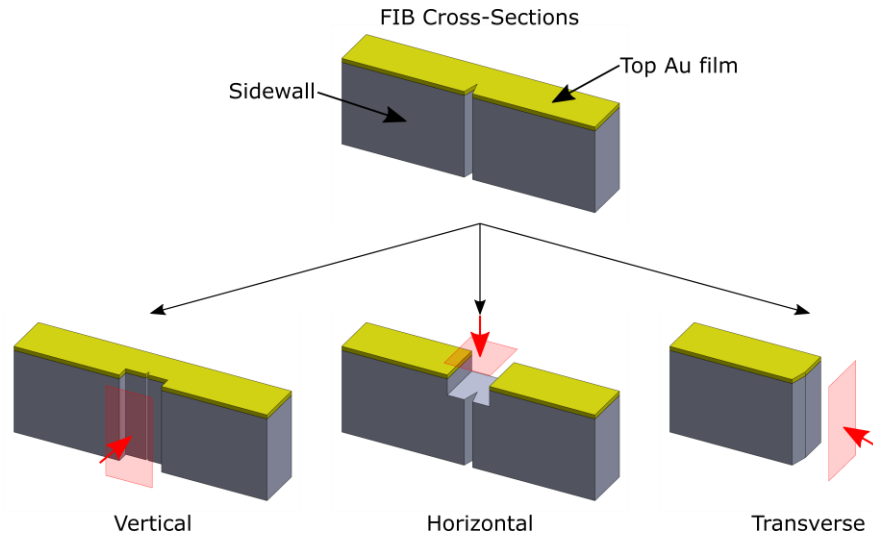
Figure 2.9 – Orientation of FIB cuts [32]

2.5 Microstructural Characterization and 3D FIB-EBSD Procedure

The characterization of the microstructure of the entire microbeam is essential to understand crack growth behavior under the different applied strain amplitudes and environmental conditions. Therefore, a 3D EBSD procedure was performed using a Tescan Lyra3 FIB-SEM and an Oxford Instruments Symmetry EBSD camera.

The microbeam beam sidewall where the fatigue damage is located was first covered with Pt to avoid any damage to the surface. A horizontal FIB cut was performed at the top of the microbeam and spanned the width of the beam. The cross-section was done with a FIB current of 2 nA for a depth of 1.5 µm. The cross sectioned surface was then polished by a FIB current of 0.2 nA to obtain a flat surface. The sample was previously placed on a 70⁰ pre-tilt holder and the EBSD camera was inserted into the system. The 2D

26

EBSD scans where performed with a step size of 0.1 µm and on an area of 45 µm x 15 µm extending across the center part of the microbeam where fatigue damage occurs. The microbeam was cross-sectioned again by another 1.5 µm in depth and the 3D EBSD procedure was repeated until the whole microbeam was characterized (about 13 cross-sections spanning the entire microbeam thickness, 20 µm). Figure 2.10 shows the microbeam at three different cross-sections right before EBSD scans were performed.
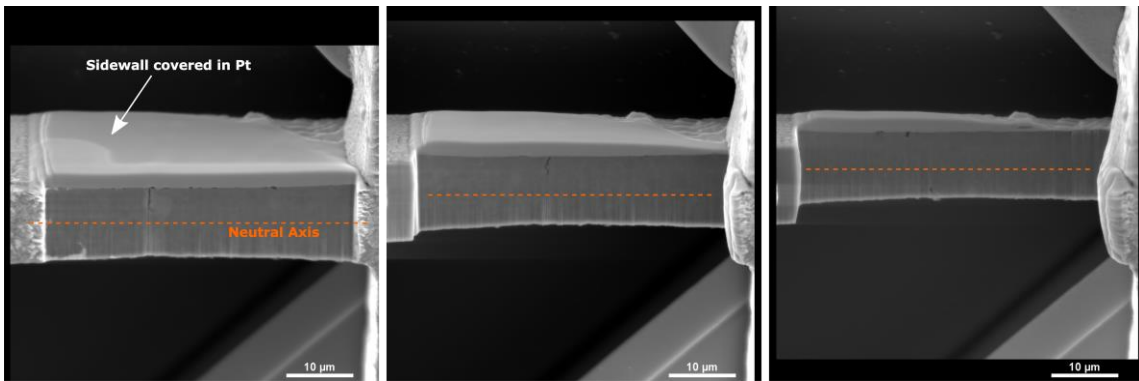
Figure 2.10 – Images of the microbeam at three different slices of the 3D EBSD procedure

2.6 Microstructure of the Microbeam

The 3D FIB-EBSD procedure also allowed for the microstructural characterization of an untested microbeam along its entire thickness. The EBSD grain orientation maps in the out-of-plane (Z) and along the beam's length (X) directions of an untested microbeam were obtained from a horizontal cut halfway through the Ni layer thickness (Z = 10 µm), see Figures 2.11a and b. The distance Z presented here is the distance from the lower surface of the microbeam with Z=0 µm at the bottom and Z = ~20 µm at the top. As mentioned before, the microstructure of the microbeam varies along the thickness, with the smaller equiaxed grains in the bottom and exhibiting columnar grains in the top. This can be clearly seen the ion contrast image of a vertical FIB cross-section of the Ni layer (see

Figure 2.11f) where the first 2.5 µm of the electrodeposited layer have an ultrafine grained

equiaxed microstructure. Figures 2.11c and d show the EBSD maps of an untested

microbeam from a horizontal cut at Z = 2.5 µm, also indicating a (001) fiber texture in the

surface normal direction. The corresponding grain size distribution plots for Z = 1, 2.5, and

10 µm are shown in Figure 2.11e. The maximum grain size is 600 nm for Z =1 µm, and

1.5 µm for Z = 2.5 µm, clearly showing that a gradient in grain size exists along the Z

direction, due to the transition from equiaxed to columnar microstructure.
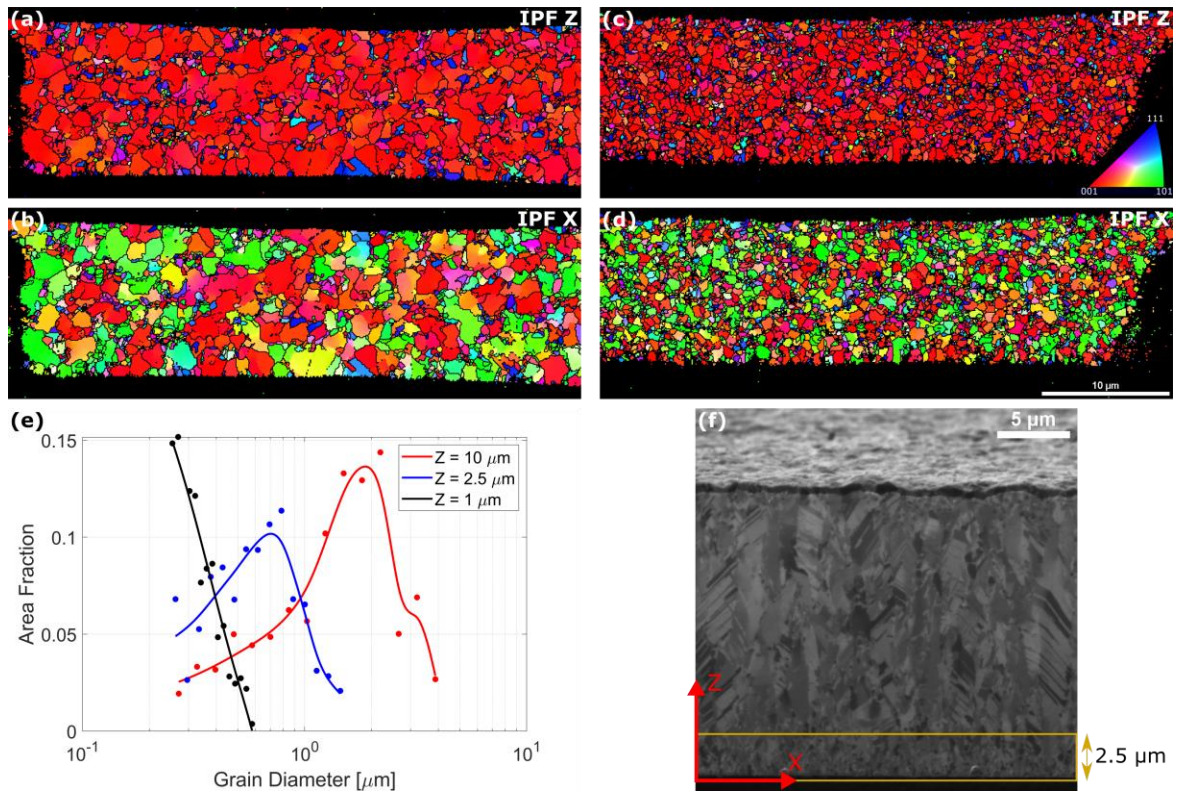
Figure 2.11 – (a) and (b) Grain orientation maps in the out-of-plane (Z) direction and in
the beam's length (X) direction, respectively, of an untested microbeam obtained from a
horizontal FIB cut halfway through the Ni layer thickness (Z = 10 µm); (c) and (d) Grain
orientation maps in the Z and X directions, respectively, of the same untested microbeam
obtained from a horizontal FIB cut ~2.5 µm from the bottom of the Ni layer (Z = 2.5
µm); (e) Grain size distributions from 3 cuts at Z = 1, 2.5, and 10 µm; (f) FIB cross-
section SEM image of the 20-µm-thick Ni layer, highlighting evolution of grain
morphology from ultrafine equiaxed grains at the bottom to microsized columnar grains.

CHAPTER 3.   HIGH AND VERY HIGH CYCLE FATIGUE

BEHAVIOR

In this chapter, the Ni microbeam HCF/VHCF behavior was investigated by performing fatigue tests with the electrostatic technique (Section 2.2). The *in situ* technique allowed for the evaluation of environmental effects on fatigue lives as well as the measurement of average crack propagation rates. The fractography observations allowed for the study of the nanoscale fatigue crack nucleation and propagation mechanisms in this fatigue regime.

3.1   *In situ* SEM Test Results

Figure 3.1a shows the evolution of f_o during an *in situ* SEM fatigue test performed at $\sigma_a = 470$ MPa and $\varepsilon_a = 0.30\%$ ($N_f = 5.6 \times 10^7$ cycles), compared to that of an *ex situ* test performed in air at $\sigma_a = 400$ MPa and $\varepsilon_a = 0.24\%$ ($N_f = 3.7 \times 10^6$ cycles). The σ_a and ε_a values presented here are the maximum values that the microbeam experiences at the sidewall when tested, estimated from Equations 2.1 and 2.2. A series of SEM images taken throughout the vacuum fatigue test (Figure 3.1b-i) capture the evolution of fatigue damage along the sidewalls, which correlates to the corresponding decrease in f_o in Figure 3.1a. The f_o evolution curve in a vacuum shows a very slow and steady decrease over the first $\sim 3 \times 10^7$ cycles that is not observed in air, which instead presents a significant decrease in f_o from the onset of the test despite being ran at a lower σ_a. Fatigue extrusions/intrusions are observed after 8.2×10^5 cycles (Figure 3.1c). Between 8.2×10^5 and 3.2×10^7 cycles, the number of extrusions along the sidewall increases significantly (Figure 3.1c-g). Some intrusions (or fatigue crack embryos) develop as well at the edges of extrusions (arrows in

Figures 3.1c-g), resulting in a relatively slow decrease in f_o (Figure 3.1a). Only after

4.3×10^7 cycles, corresponding to a 4% decrease in f_o, can a clear fatigue crack be observed

(arrow in Figure 3.1h). The nucleation of the fatigue crack occurred between 1.4 and

3.2×10^7 cycles, corresponding to a decrease in f_o between 1 and 2% [32]. The comparison

of the curves shown in Figure 3.1a strongly suggest that the air accelerates the fatigue crack

nucleation process by at least 1 order of magnitude since for the test ran in air, a 4%

decrease in f_o happens only after just 2.3×10^6 cycles [32].
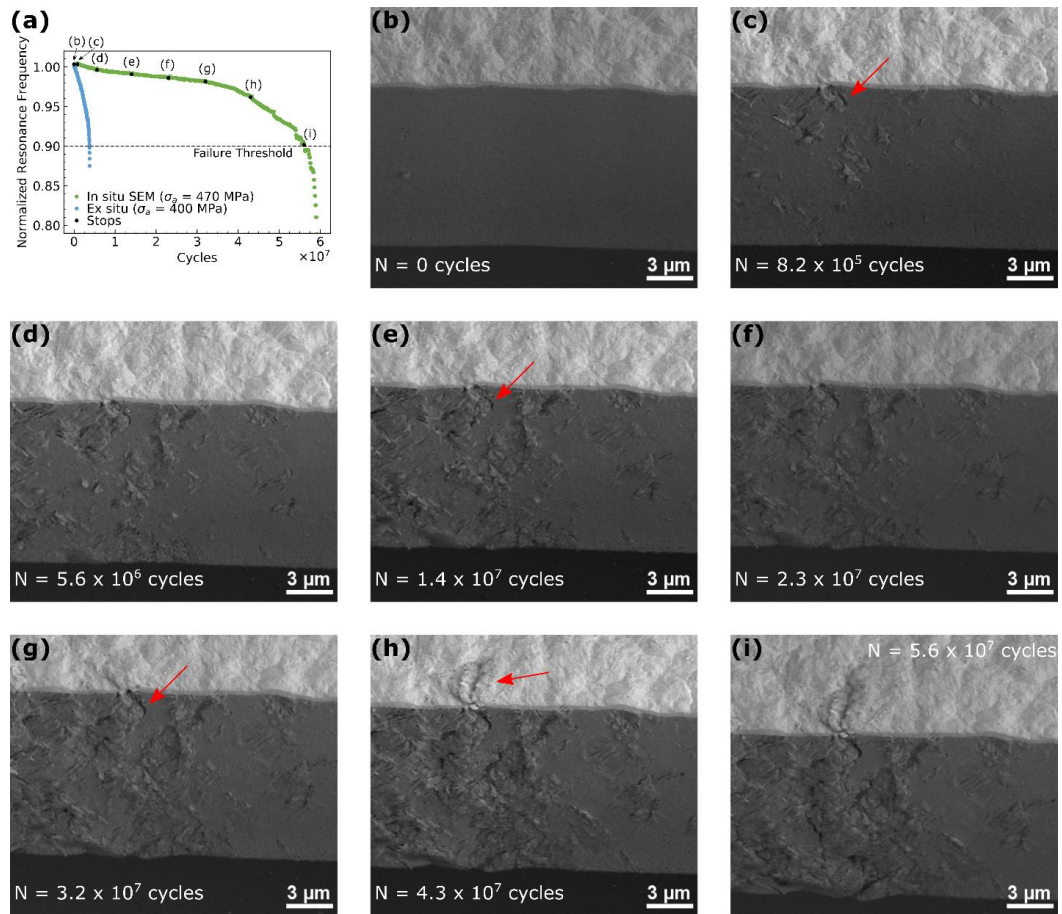
Figure 3.1 – (a) Normalized resonance frequency evolution ($\frac{f_o}{f_{o,i}}$) during an *in situ* SEM test performed at σ_a = 470 MPa (ε_a = 0.30%) and an ex situ test in air at σ_a = 400 MPa (ε_a = 0.24%). (b−i) SEM images showing the evolution of the damage along the microbeam sidewall, at an increasing number of cycles [32]

Figure 3.2a also highlights the influence of stress and strain between microbeams ran in air and in vacuum. The sample in Figure 3.2b was tested in air at $\sigma_a = 365$ MPa and $\varepsilon_a = 0.21\%$ for $N_f = 4.1 \times 10^7$ cycles, while the sample in Figure 3.2c was tested in vacuum at $\sigma_a = 485$ MPa and $\varepsilon_a = 0.32\%$ for $N_f = 4.3 \times 10^7$ cycles. The stress amplitude applied in the microbeam tested in vacuum was about 33% higher than the one tested in air in order for both to fail at approximately the same number of cycles. Looking at the shape of the curves, the resonance frequency of the microbeam tested in air decreases steadily until a ~6% decrease in f_o and then decreases rapidly until failure due to the fast crack propagation. The f_o evolution curve for the microbeam tested in vacuum also decreases steadily, although at a slower rate, until a 3% decrease and then shows either portions of fast or slow decreases in f_o until the rapid decrease at around 6%. This comparison again suggests the influence of the air in accelerating crack nucleation and decreasing fatigue lives. Additionally, the quasi-continuous observation of the fatigue damage along the sidewall (Figures 3.1b-i) provides information regarding the evolution of the crack shape, from a 3D, "penny-shaped" crack to a longer crack that, in most cases, spans the entire thickness of the microbeam (2D crack), as seen in Figures 3.2b and c.
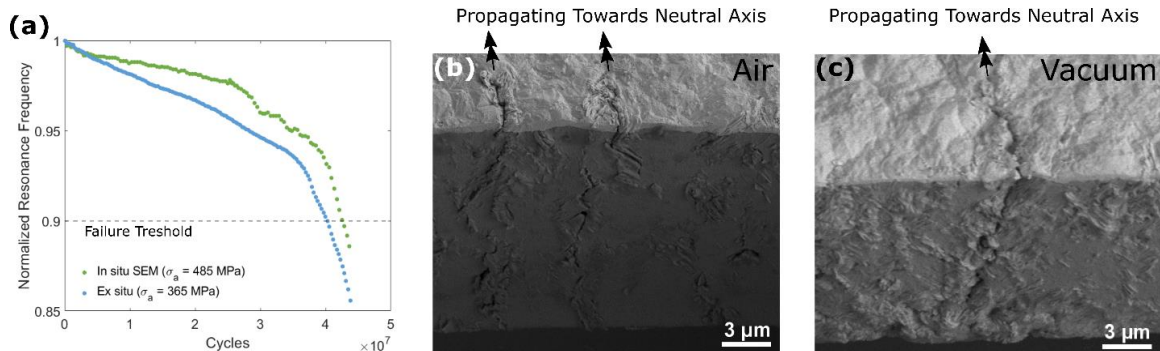
Figure 3.2 – Normalized resonance frequency evolution during an *in situ* SEM test performed at $\sigma_a = 485$ MPa and $\varepsilon_a = 0.32\%$ and an ex situ test in air at $\sigma_a = 365$ MPa and $\varepsilon_a = 0.21\%$; (b) Sidewall images of the sample tested in air after failure; (c) Sidewall images of the sample tested in vacuum after failure

The test shown in Figure 3.3 confirms these findings and consists of cycling a microbeam first in a vacuum at $\sigma_a = 420$ MPa and $\varepsilon_a = 0.25\%$ for $6.4{\times}10^7$ cycles, followed by cycling in air at $\sigma_a = 360$ MPa and $\varepsilon_a = 0.21\%$ for $\sim 1.5{\times}10^7$ cycles, and further cycling again in a vacuum (at $\sigma_a = 420$ MPa). SEM images at the end of each segment were taken to observe crack initiation and growth. Figure 3.3a shows that f_o does not decrease in a vacuum for the first $6{\times}10^7$ cycles, at which point the SEM image (Figure 3.3c) shows that extrusions were formed, but no fatigue cracks, which is consistent with a constant f_o. During the fatigue test in air, despite at a lower σ_a, f_o decreases 4%, which correlates with the initiation and growth of a fatigue crack (arrow in Figure 3.3d). This crack initiated next to an extrusion formed while cycling in a vacuum. (See Figure 3.3c). Upon further testing in a vacuum, the crack grew further, as evidenced by the decrease in f_o shown in Figure 3.3a and the arrows in Figure 3.3e. Overall, these results indicate that air plays a crucial role in the formation of fatigue cracks [32].
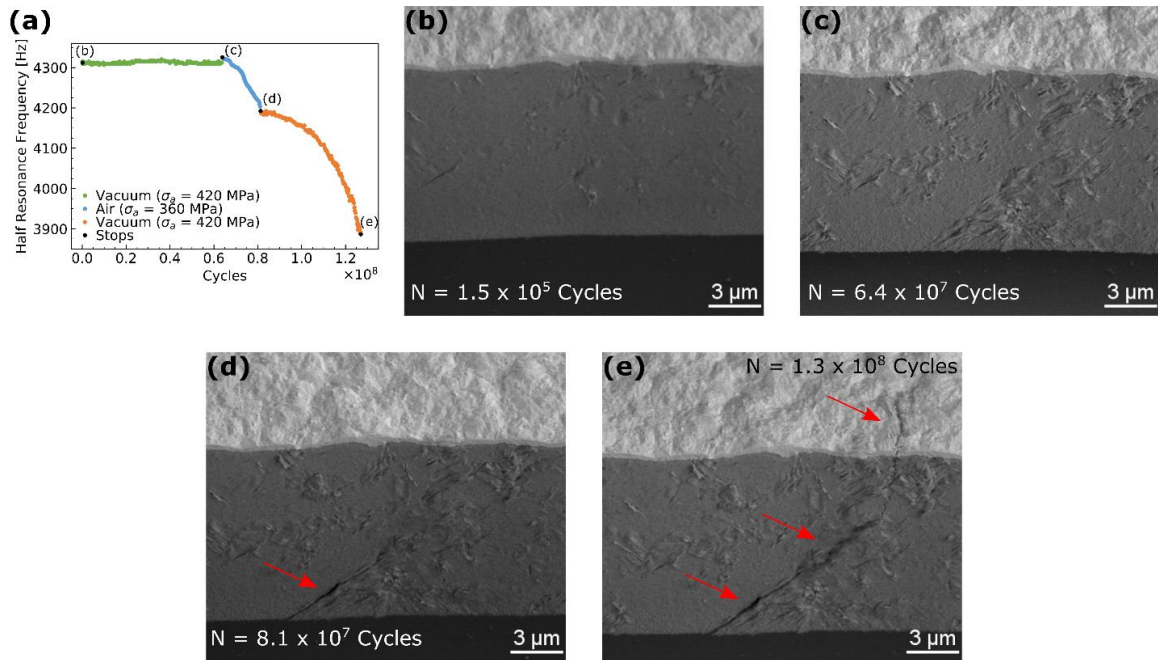
Figure 3.3 – (a) Frequency evolution during an *in situ* SEM test performed at $\sigma_a = 420$ MPa and $\varepsilon_a = 0.25\%$ followed by *ex situ* testing in air at $\sigma_a = 360$ MPa and $\varepsilon_a = 0.21\%$ and back to a vacuum at $\sigma_a = 420$ MPa. (b−e) Inclined SEM images showing the evolution of the damage along the microbeam sidewall [32].

3.2   Stress-Life Curves

Through the repetition of several tests like the ones shown above, it was possible to develop stress-life and strain life curves to study the HCF/VHCF behavior. Figure 3.4a shows the S-N fatigue curves for the Ni microbeams tested in a vacuum (*in situ* SEM experiments) and in air (*ex situ*, at 30 °C, 50% RH and 80 °C, 90% RH), while Figure 3.4b shows the strain-life curve [31]. The empty symbols denote runouts, while the solid ones represent fatigue failure. As can be seen when tracing a horizontal line at $\sigma_a = 450$ MPa in Figure 3.4a, the curves highlight 3 orders of magnitude longer fatigue lives in vacuum ($N_f \sim 10^8$ cycles in a vacuum vs $\sim 10^5$ cycles in air). Below a stress level of 420 MPa, specimens tested in a vacuum do not fail, while the ones tested in air have N_f ranging from 10^5 to 10^8 cycles for σ_a ranging from 450 to 300 MPa. No fatigue failure was observed in

air below σ_a = 300 MPa (runouts >3 ×10^9 cycles). The *in situ* SEM fatigue experiments unambiguously demonstrate that the longer N_f measured in a vacuum is both due to the significant role of air in both fatigue crack nucleation and propagation [32].
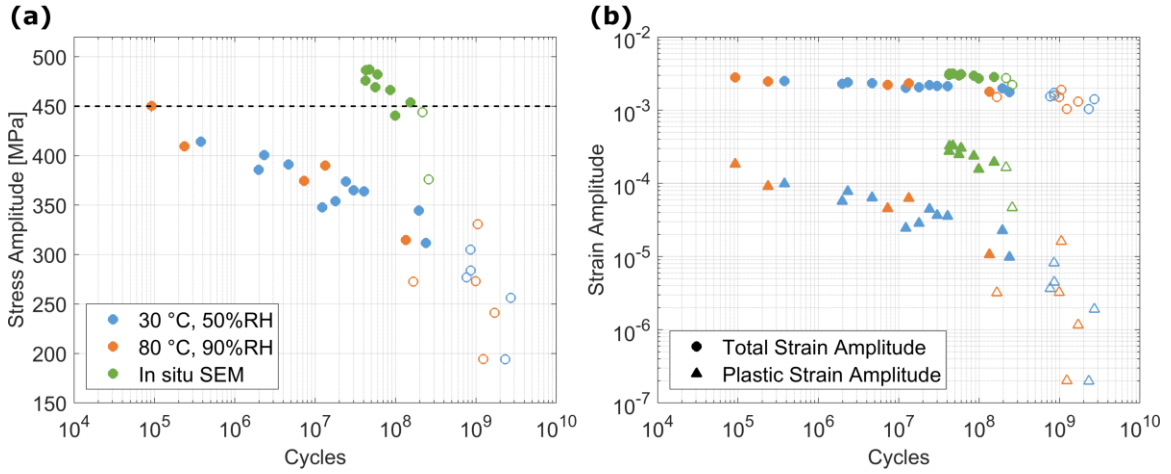
Figure 3.4 – (a) Stress-life and (b) strain-life curves for *in situ* (vacuum) and *ex situ* (air) fatigue tests [32]

3.3 Fatigue Crack Growth Rates

The *in situ* technique also allowed for the further investigation into crack propagation rates. The effect of air on fatigue crack propagation rates for these microbeams was quantified through the following series of experiments. Figure 3.5a shows the f_o evolution plot of a fatigue test consisting of cycling a specimen at σ_a = 400 MPa (ε_a = 0.24%) in air for 9.3×10^6 cycles, followed by cycling in a vacuum until 1.3×10^8 cycles, first at σ_a = 350 MPa (ε_a = 0.20%) and then at σ_a = 385 MPa (ε_a = 0.23%). Two 2D cracks (i.e., SEM examination of the sidewalls confirmed the cracks spanned through the microbeam's thickness), one on each side of the microbeam, developed in air during the first portion of the test (Figure 3.5b). Based on the measured total crack length at the surface, 2a, where a is the crack length, the average surface crack growth rate in air is

34

3×10^{-13} m/cycle. This rate is extremely low and indicates strong size effects associated with the fatigue behavior of these microbeams. The crack did not extend in a vacuum at σ_a = 350 MPa, but at σ_a = 385 MPa, the crack grew as shown in Figure 3.5d-e. The average surface crack growth rate in vacuum is 5.5×10^{-15} m/cycle, which is about 50 times slower than in air [32].
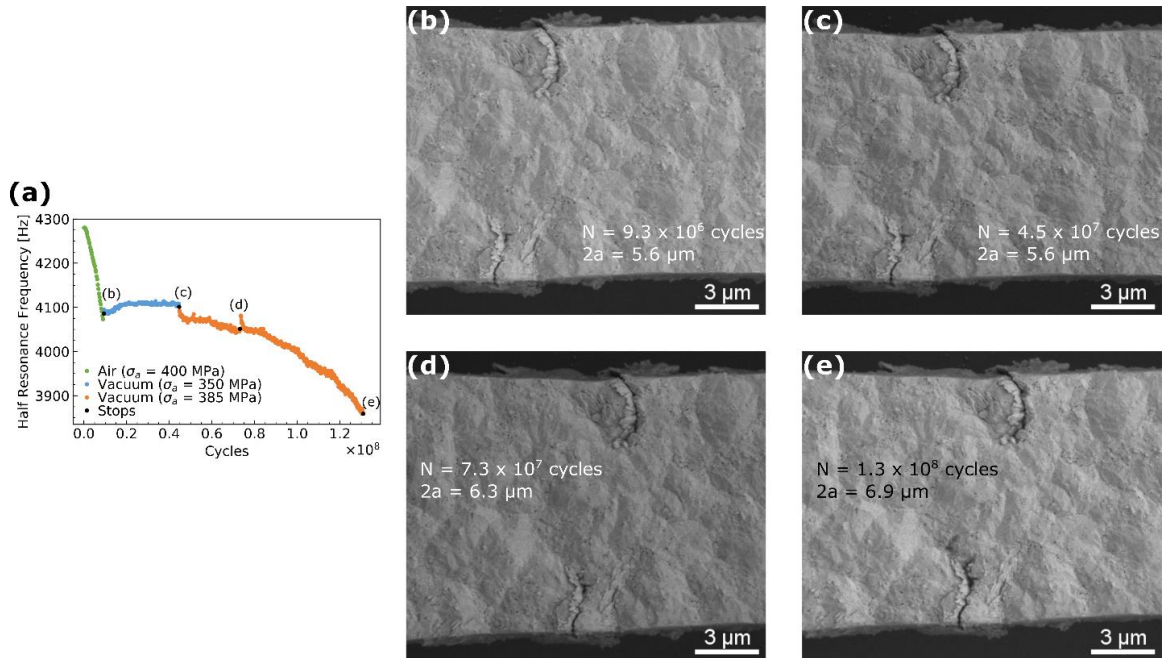
Figure 3.5 – (a) HCF test ran partially in air and then in vacuum, (b)-(e) Top images of the cracked microbeam throughout the test [32]

In a similar experiment, Figure 3.6a shows the f_o evolution plot of a fatigue test consisting of cycling a specimen at σ_a = 390 MPa (ε_a = 0.23%) in air for 4.8×10^6 cycles, followed by cycling in vacuo until 7.4×10^7 cycles at σ_a = 360 MPa (ε_a = 0.21%). Two cracks, one on each side of the microbeam, developed in the portion of test ran in air. Between stops (b) and (c) (see Figure 3.6a), the crack grows (compare Figures 3.6b and c), based on the surface crack length, at an average rate of 2.0×10^{-12} m/cycle. The crack did not extend in vacuo at σ_a = 360 MPa between stops (c) and (d), but extended between (d)

and (f) (See corresponding SEM images in Figure 3.6) at a rate of 3.7×10^{-14} m/cycle. The average crack growth in vacuum is, again, about 50 times lower than the average rate in air.
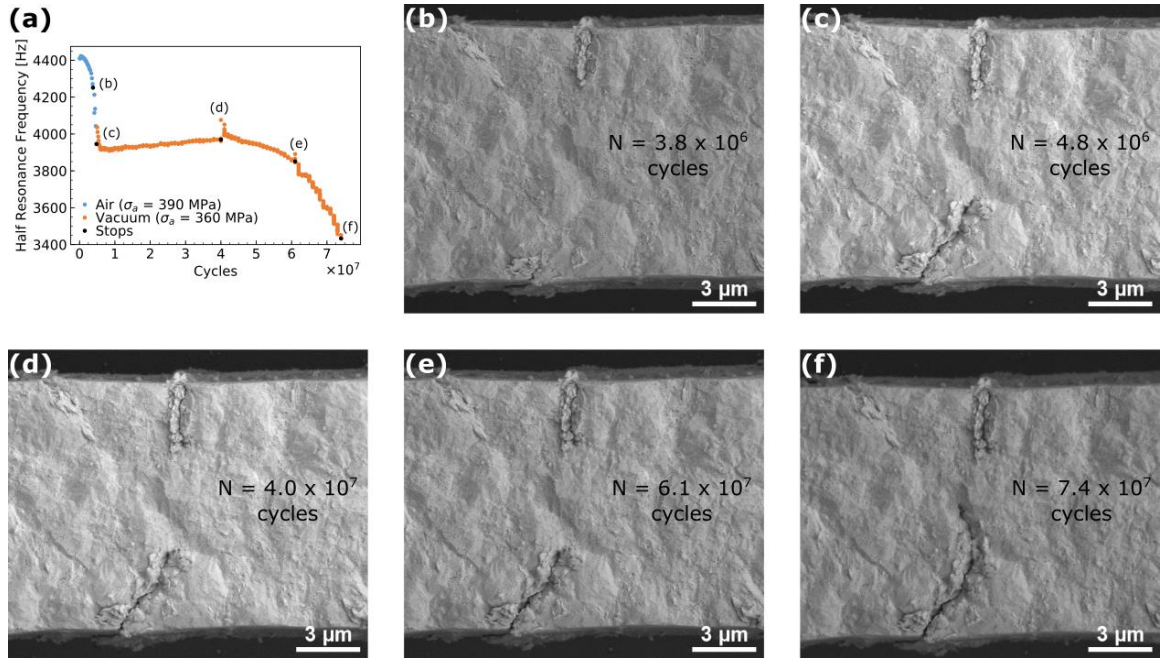
Figure 3.6 – (a) HCF test ran partially in air and then in vacuum, (b)-(e) Top images of the cracked microbeam throughout the test [32]

Figure 3.7a summarizes all of the measured crack growth rates in air and a vacuum, based on the crack length measurements (ranging between 1 and 3 μm) with the SEM images (providing a resolution of ~10 nm), as a function of σ_a, confirming the ultralow rates and highlighting the roughly 2 orders of magnitude larger rates in air compared to a vacuum. Figure 3.7b shows the crack growth rates as a function of measured crack length. These ultralow crack growth rates were only measured for fatigue cracks that spanned the microbeam's thickness (2D cracks), thanks to the *in situ* SEM technique that allowed meticulous observation of the crack shape evolution. While this crack growth rate measurement technique does not follow the traditional fatigue dimensional requirements,

it is based on the direct measurement of the crack size and therefore provides an accurate measurement of the local crack growth rates (at the surface), which are not expected to be much different from the overall crack growth rates of the 2D cracks given the fairly uniform crack fronts observed *postmortem*. Importantly enough, these rates are of the same order of magnitude as the rates previously calculated based on finite element models linking the decrease in f_o to an increase in crack size [23, 31]. However, these new rates are more accurate since they are based on the direct measurement of crack size (for 2D cracks), whereas the previously calculated rates relied on simplifying assumptions (such as the assumption of a single crack on each size of the microbeam contributing to the measured decrease in f_o). Overall, these rates are several orders of magnitude lower than that typically measured on macroscopic specimens. Nonetheless, they can be measured thanks to the large testing frequency and to the microscopic size of the specimens (in 1 min of testing, a rate of 10^{-14} m/cycle would lead to ~5 nm crack extension). Being significantly less than one interatomic spacing (~2.5×10^{-10} m) per cycle, these rates suggest that crack growth is not a continuous process but instead occurs in between incubation periods. For example, at an average rate of 10^{-14} m/cycle, it would take 25 000 cycles (3 s of testing) to grow the crack by one interatomic spacing. The fractography results shown in Section 3.5 highlight a new fatigue mechanism accounting for this ultraslow fatigue crack growth [32].
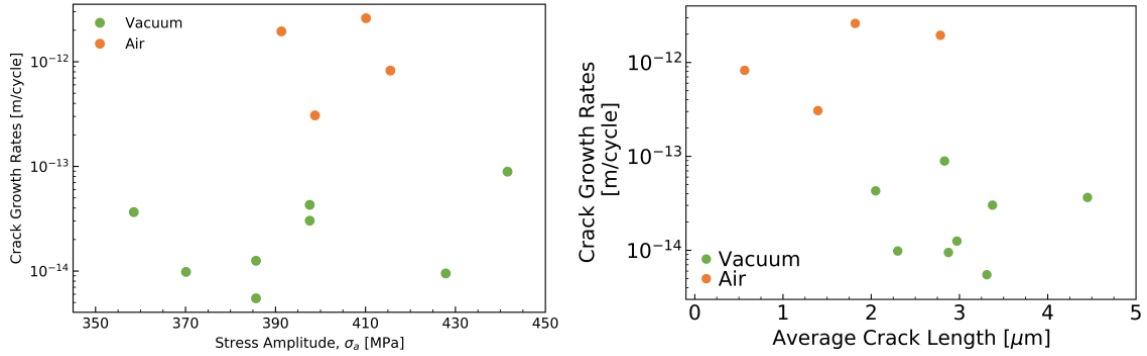
Figure 3.7 – Average surface crack growth rates (a) as a function of stress amplitude and (b) as a function of average crack size [32]

3.4   Extrusions Characterization

The *in situ* technique also allowed for the characterization of fatigue extrusions on the microbeams' sidewalls as cycling increased. High resolution images of the extrusions at different stages of a fatigue test were analyzed for both vacuum and air environments. The extrusion heights were measured by analyzing top view SEM images of the extrusions in fatigued microbeams. Figure 3.8a shows the top view images of a microbeam tested in vacuum at σ_a = 490 MPa (ε_a = 0.32%), highlighting selected extrusions (extrusion #1 and #2) for the characterization study. Figure 3.8b shows the evolution of the extrusion height as cycling increased. Each data point in Figure 3.8b represents an interruption on the *in situ* test for characterization of the extrusions. The expected fatigue life at this stress/strain according to the S-N curve is ~4×10^7 cycles. The precision on the extrusion height measurements from top view images is ± 30 nm. Extrusion #1 increased to a maximum height of 300 nm after ~1.7×10^5 cycles, after which the extrusion stopped growing in height. In contrast, extrusion #2 continued to increase in height as cycling continued, reaching a height of ~480 nm after ~4×10^6 cycles. Figures 3.8c-e show high magnification images of extrusion #1 at different stages of the test. Although the extrusion height remains

at a maximum, intrusions are clearly deepening into the microbeam as cycling increases. A crack eventually forms near extrusion #2, highlighted in Figure 3.8f. The crack can be observed on the sidewall after 4×10^6 cycles, which is consistent with Figure 3.1, while extrusions starts growing after only 1×10^5 cycles.

A similar analysis was performed on a microbeam tested in air at $\sigma_a = 395$ MPa ($\varepsilon_a = 0.24\%$) and on another microbeam tested in vacuum at $\sigma_a = 380$ MPa ($\varepsilon_a = 0.22\%$) to compare the environmental effects on extrusion formation on microbeams tested at similar stress amplitudes. Two extrusions were selected, extrusion #3 in the sample tested in air (Figure 3.9a and b) and extrusion #4 in the sample tested in vacuum (Figure 3.9c and d). Figure 3.9e shows the extrusion heights as a function of cycling for the two selected extrusions. Extrusions with recognizable heights are observed in both samples after $\sim1\times10^6$, however the rate at which extrusions grow is much faster in air. The extrusion in air takes 2.6×10^6 cycles to reach a height of 0.4 µm, while the extrusion in vacuum takes at least an order of magnitude longer. This result highlights once more the influence of air in accelerating crack nucleation.
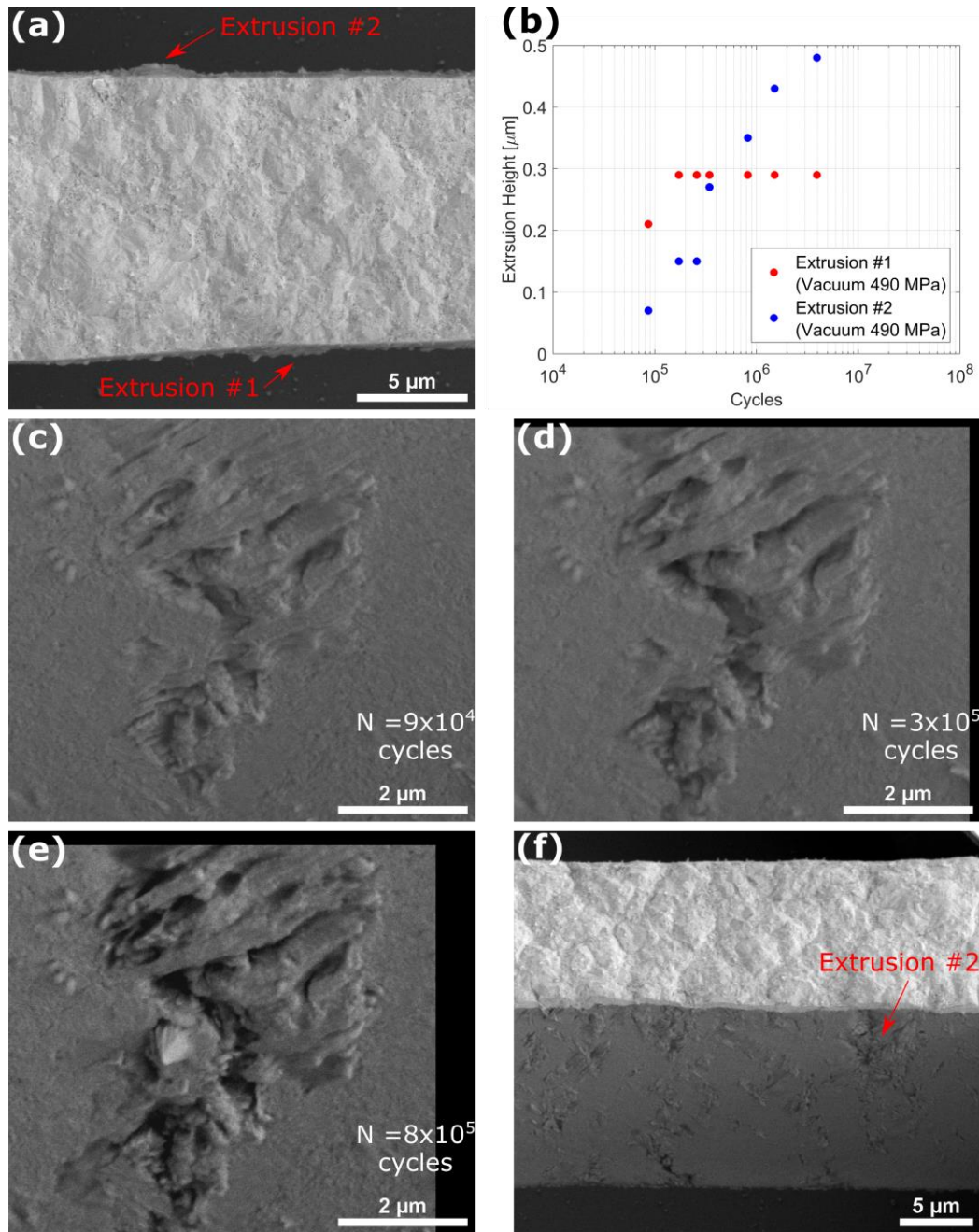
Figure 3.8 – (a) Top view of extrusion #1 and 2; (b) Extrusion height evolution as a function of cycling; (c)-(e) Inclined SEM images of extrusion #1 at different stages of fatigue test; (f) Crack near extrusion #2 after 4×10^6 cycles
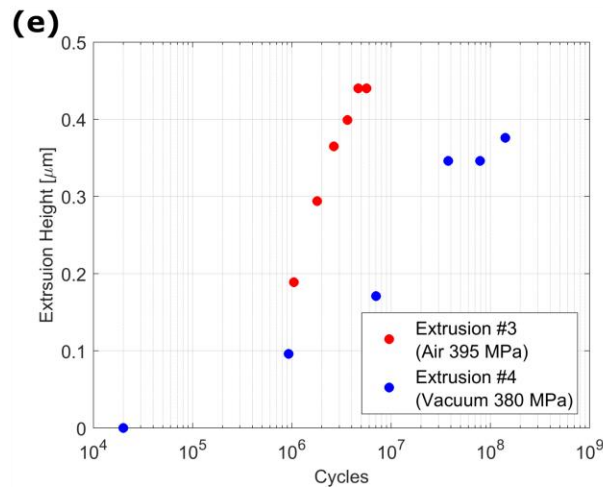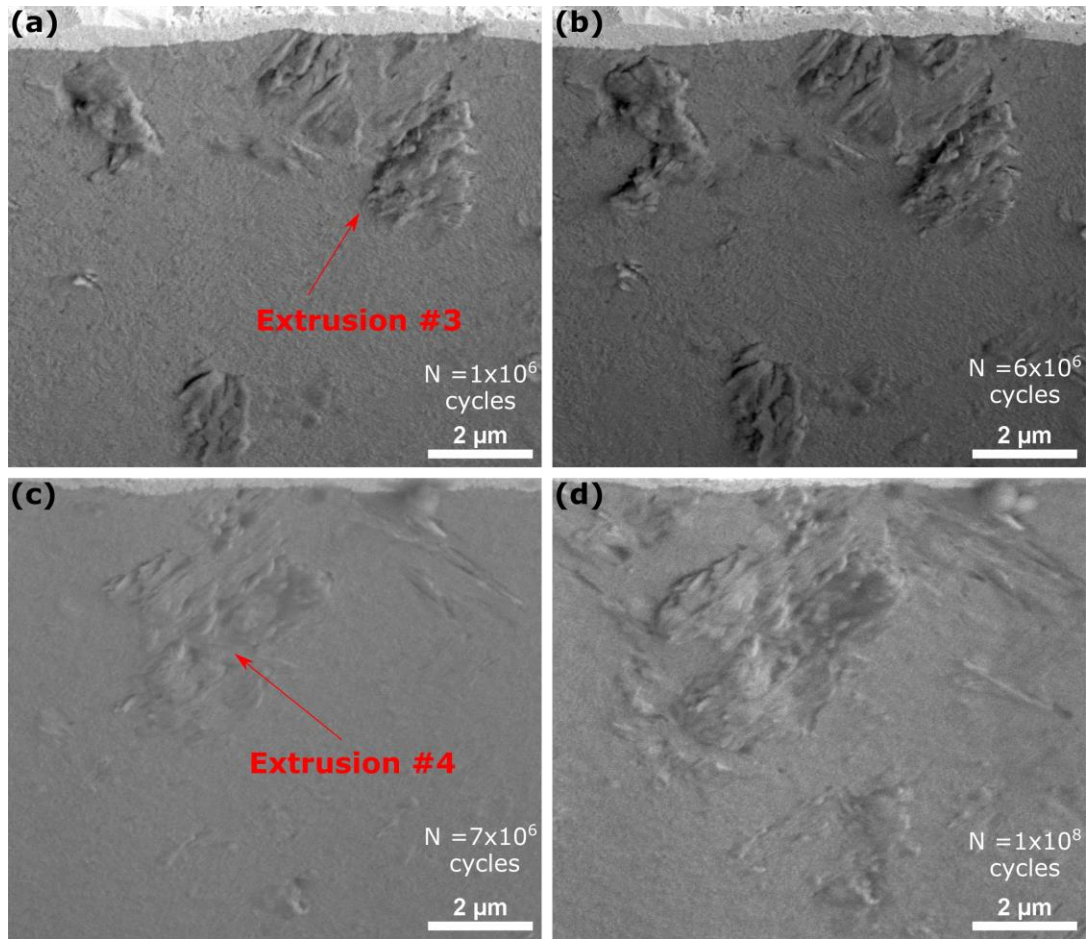
Figure 3.9 – (a) and (b) Extrusion #3 of microbeam tested in air at σ_a = 395 MPa (ε_a = 0.24%); (c) and (d) Extrusion #4 of microbeam in vacuum at σ_a = 380 MPa (ε_a = 0.22%); (e) Extrusion height evolution as a function of cycling

3.5   Fractography

3.5.1   FIB Cuts and Voids

To further understand the mechanisms responsible for the ultralow crack growth rates, a series of FIB cross sections (orientations of the cuts in Figure 3.10a) was performed on five specimens: three fatigued in air and two in a vacuum. For both testing environments, these FIB cross sections reveal a tortuous crack path consisting of voids (ranging in size from ~10 to ~500 nm) that are linked together by straight crack paths. Voids are either observed in the vicinity of the cracks (within ~1 μm; examples in Figure 3.10b, c, i) or in the subsurface underneath the extrusions (also within ~1 μm of the surface; Figure 3.10k−m). Figure 3.10d clearly shows two cuboid voids, each ~10 nm in size, formed ~500 nm ahead of the main crack tip, at a 45° angle with respect to the main crack. A very thin crack appears to be linking the main crack tip to the two voids. Very similar observations can be made at the location of the extrusions, where fatigue cracks nucleate. For example, Figure 3.10l shows small voids developing underneath the extrusions and thin cracks linking them together. For the specimens tested in air, there are many more voids along the crack path (Figure 3.10h and i), as a result of which the crack faces appear to be rougher. Oxygen maps using EDS have clearly identified the voids to be oxygen rich for the tests in air (example in Figure 3.10j), which is not observed for the tests in a vacuum, implying that oxygen or water play a significant role in the formation of these voids.

Figure 3.11 shows the low magnification SEM images of a series of parallel horizontal FIB cuts (at different distances from the top surface) performed on the microbeam ran in vacuum which are also shown in higher magnification in Figure 3.10d,

e, g, k and l. Figure 3.11 demonstrates the 3D aspect of the crack and shows that the main cracks at the end of these fatigue tests are fairly uniform through the thickness of the microbeam. Similarly, Figure 3.12 shows low magnification images of a series of parallel vertical FIB cuts (at different distances from the sidewall) for another microbeam tested in vacuum. Higher magnification images of the cracks are shown in Figure 3.10b and c. The crack is through the entire microbeam's thickness in Figure 3.12d-g, up to ~2 μm from the sidewall. In Figure 3.12h and i (closer to the neutral axis), the crack is present only in the top half of the microbeam's thickness.

Additionally, Figure 3.13a shows the location of a progression of transverse FIB cuts (at different distances from the microbeam's base) near a crack of a microbeam tested in air at $\sigma_a = 360$ MPa ($\varepsilon_a = 0.21\%$) for 4.4×10^6 cycles. Figure 3.13b-f show a void that grows as the FIB cuts get closer to the crack.in the sidewall. The spacing in between the transverse cuts is a few nm. The progression of transverse cuts highlights the complex 3D nature of the voids in the vicinity of cracks.
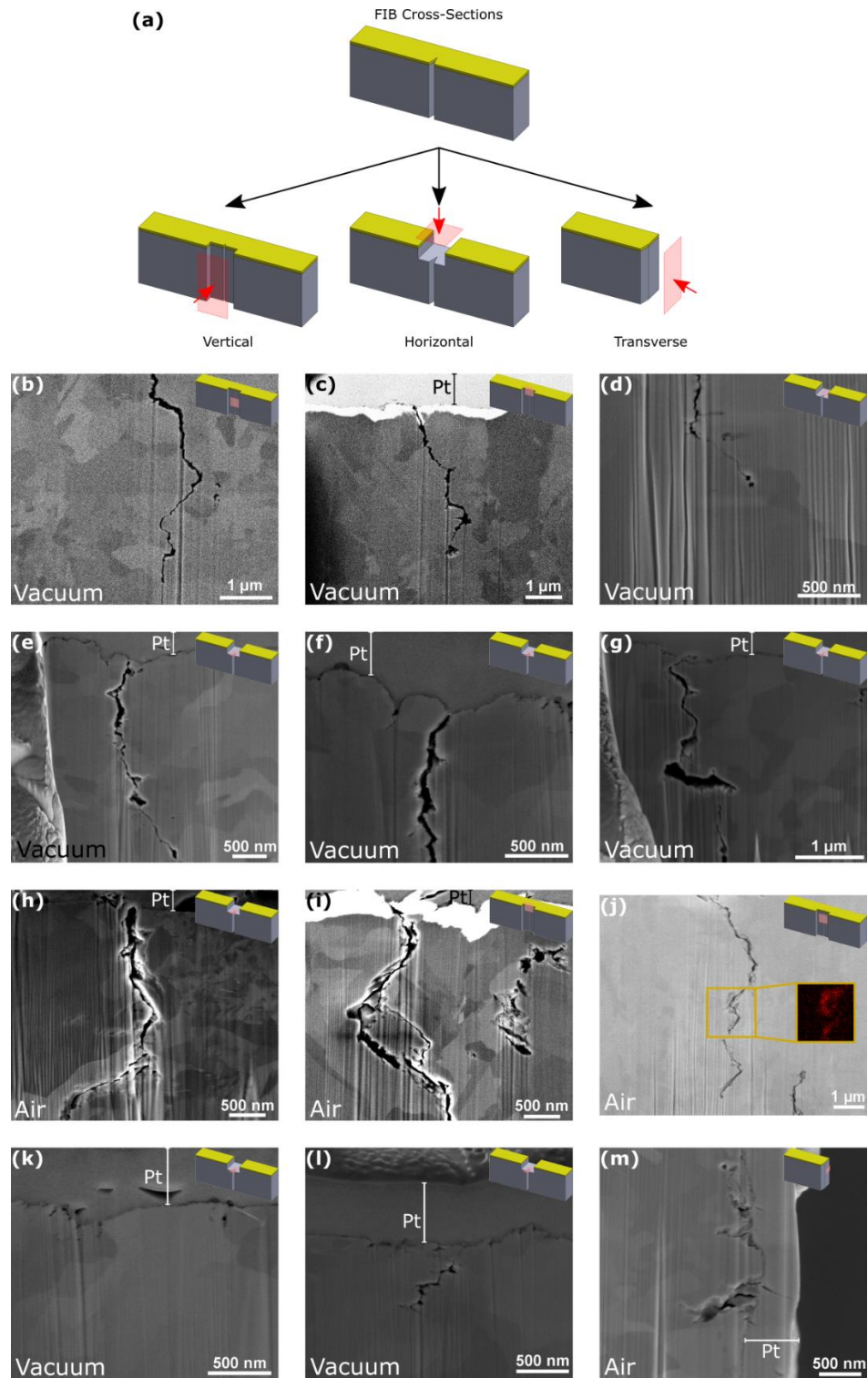
Figure 3.10 – (a) Schematic details presenting the different types of FIB cross sections. (b−g) Cracks and voids for *in situ* SEM tests. (h−i) Cracks and voids for tests in air. (j) Results of oxygen concentration from EDS scans along the crack of a specimen tested in air
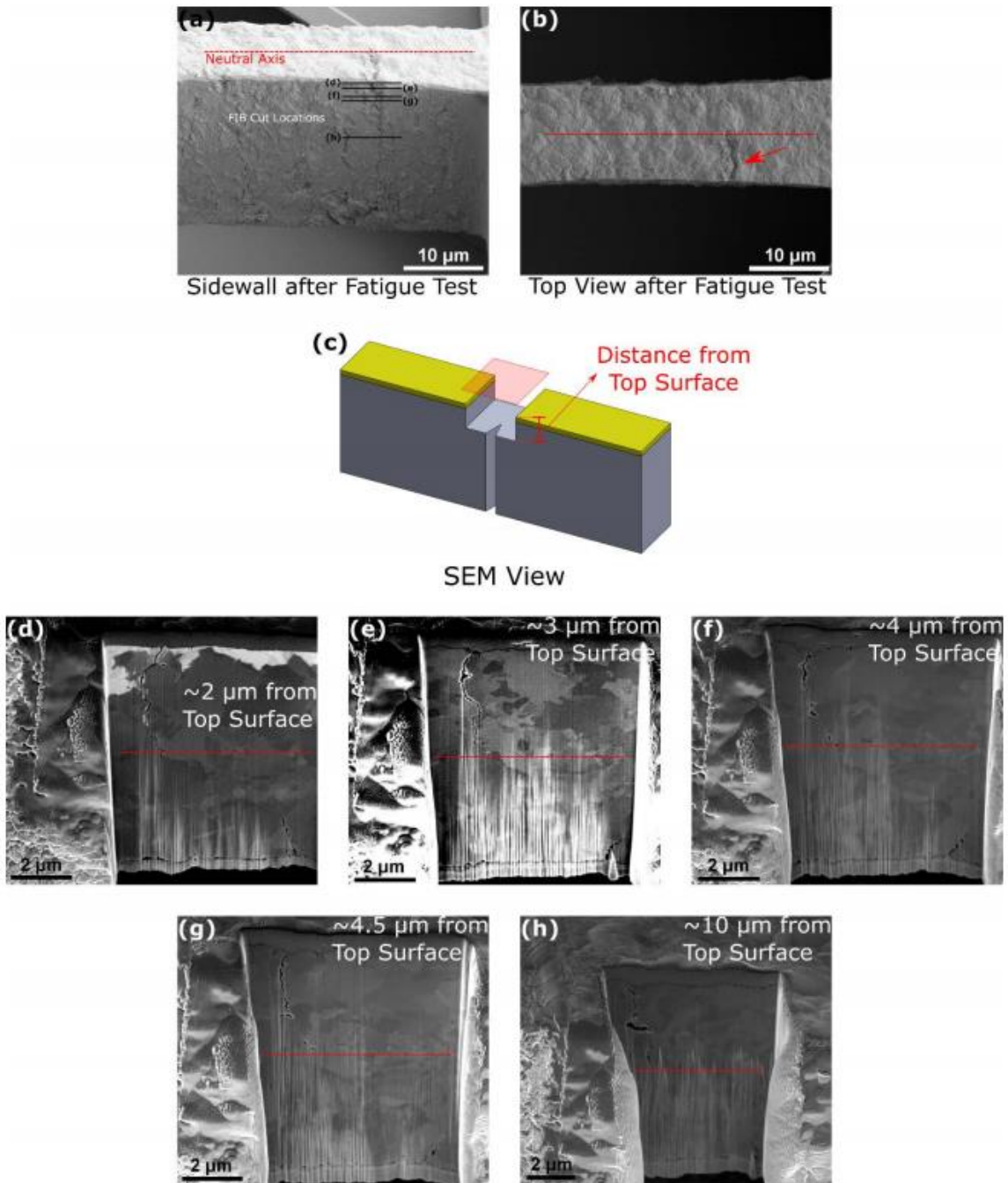
Figure 3.11 – (a) Location of horizontal FIB cuts along sidewall; (b) Top view image of microbeam after fatigue test. The red arrow indicates the location of the fatigue cracks. The red dotted line is the neutral axis; (c) Schematic showing the definition of distance from top surface; (d)-(h) SEM images showing the overall shape of the fatigue crack at the various locations
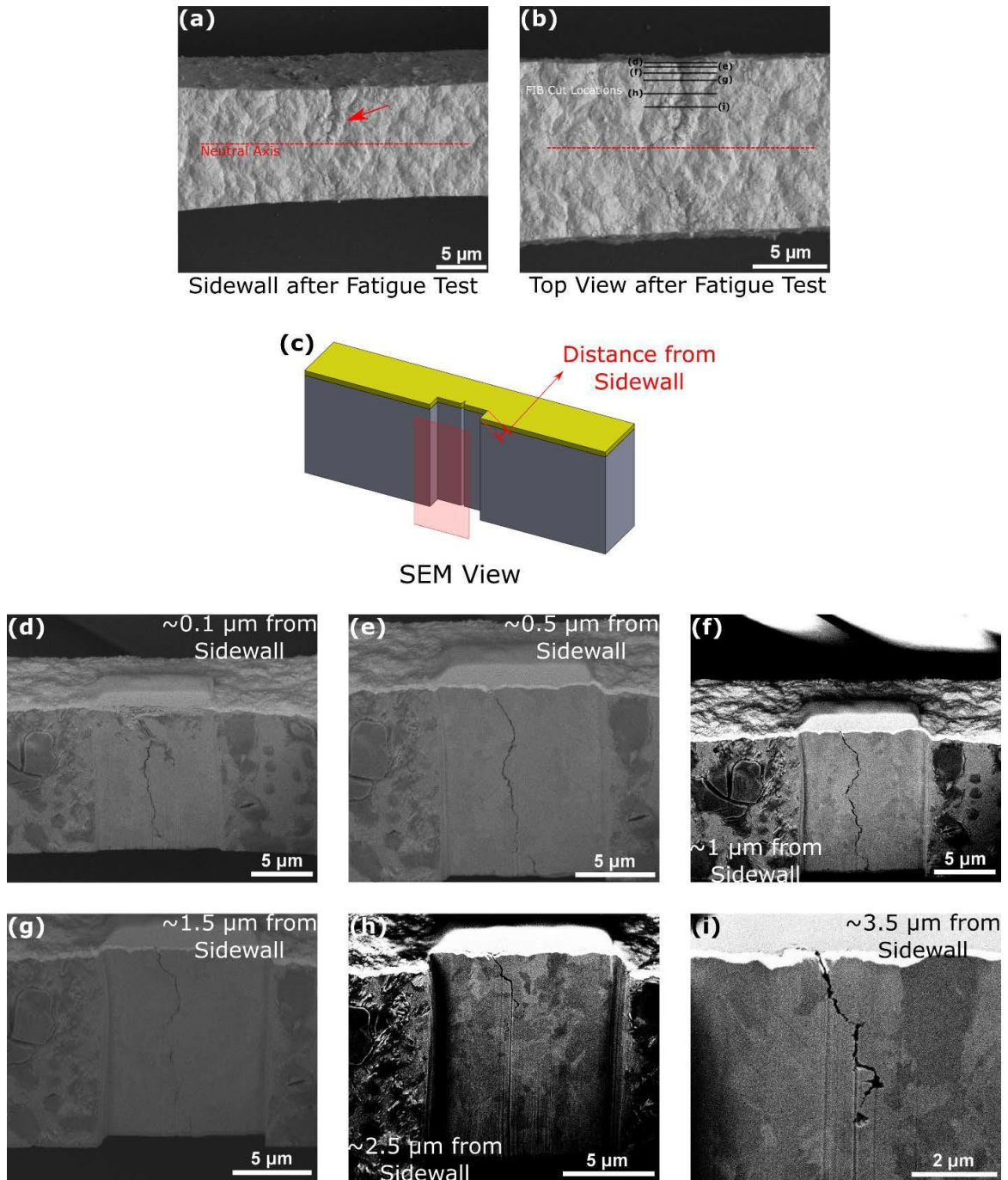
Figure 3.12 – (a) Inclined SEM image after fatigue test; red arrow indicates fatigue crack location; (b) Top view SEM image of microbeam after fatigue test with location of vertical FIB cuts. The red dotted line is the neutral axis; (c) Schematic showing the definition of distance from sidewall; (d)-(i) SEM images showing the shape of the fatigue crack at the various locations.
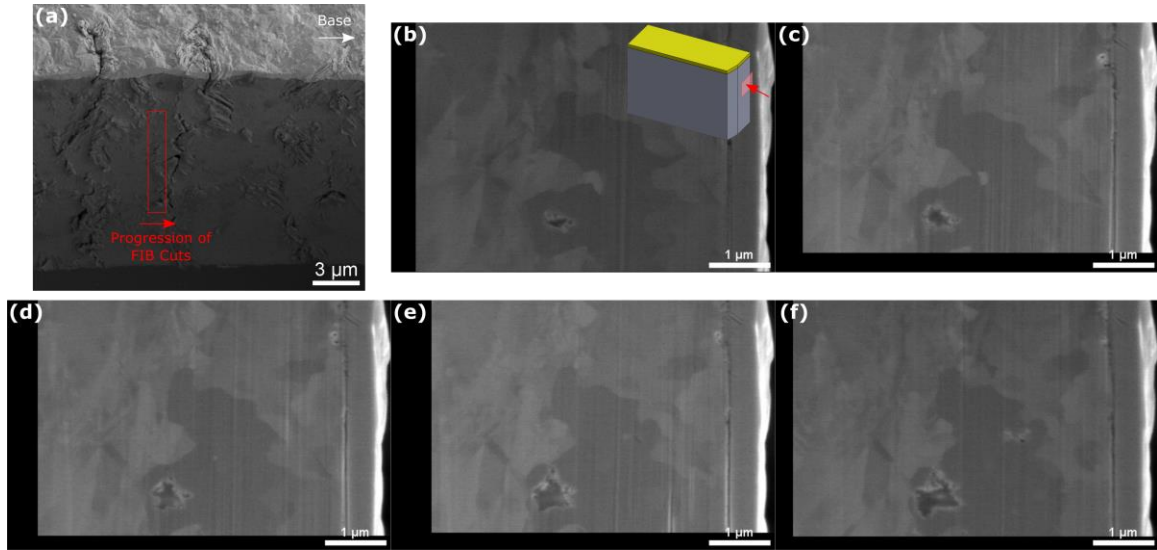
Figure 3.13 – (a) Location of serial transverse FIB cuts, (b)-(f) SEM images showing the shape and growth of a single void as it approaches a fatigue crack

3.5.2   FIB Slices and Crack Growth Path

In order to investigate the characteristics of the path of the fatigue cracks in the microbeams, the 3D FIB-EBSD procedure (see Section 2.5) was used to obtain crack and grain information through the entire thickness of the microbeam.

Figure 3.14 shows the top view and sidewall of a microbeam tested in vacuum at $\sigma_a = 470$ MPa ($\varepsilon_a = 0.30\%$) and cycled for 6×10^7 cycles (same sample tested in vacuum shown in Figure 3.1). The images also show the selected coordinate system for the evaluation of the slices. In the 3D FIB-EBSD procedure slices are taken parallel to the top surface at different heights. The height along the Z-axis is measured from the bottom of the microbeam (e.g. $Z = 0$ µm at the bottom and $Z = \sim 20$ µm at the top of the microbeam). The locations of selected slices are also shown in Figure 3.14b.

47
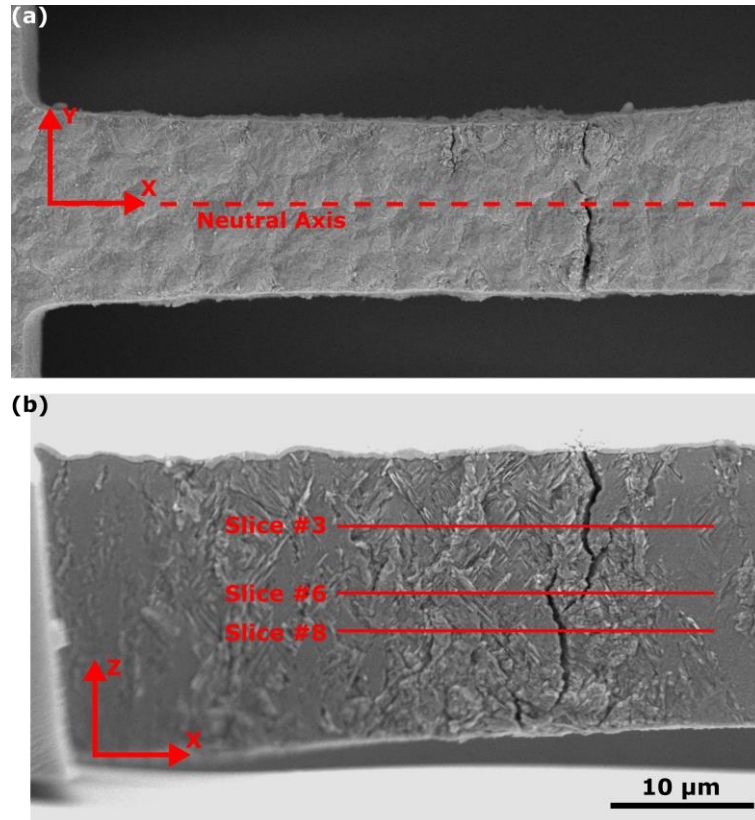
Figure 3.14 – (a) Top view and (b) sidewall of microbeam tested in vacuum at $\sigma_a = 470$ MPa ($\varepsilon_a = 0.30\%$) for 6×10^7 cycles

Figure 3.15 shows the SEM images, the Band Contrast and the Inverse Pole Figure (IPF) in the out-of-plane direction (IPF Z) of the selected slices shown in Figure 3.14b. Since the microbeam had been tested past the failure threshold, cracks spanned the entire thickness of the microbeam and at some points also the entire width with cracks growing across the neutral axis (Figure 3.15c). Some cracks are rugged and appear to change directions as they encounter barriers to their growth, although other cracks are more straight in nature. The crack path characteristics are easily identifiable using the EBSD information. Figure 3.15a highlights three cracks. The two cracks on the left sidewall are transgranular cracks, while the one on the right sidewall is intergranular. Figures 3.15b and c also show cracks with both intergranular and transgranular natures. Overall, analyzing all

slices, about half of the cracks were intergranular and half were transgranular in the microbeam tested in vacuum at a relatively high stress/strain amplitude.
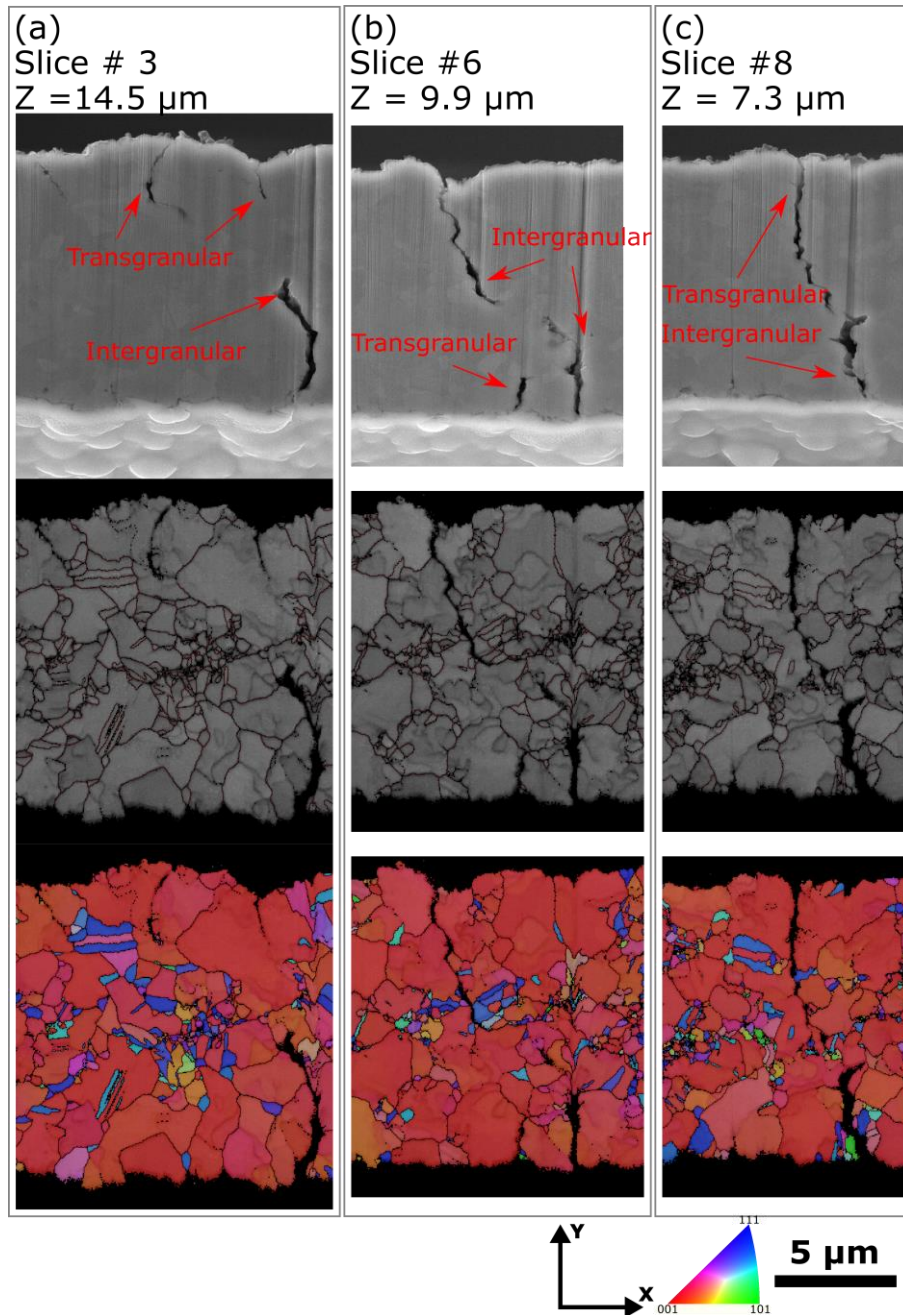
Figure 3.15 – (a)-(c) SEM, band contrast and IPF Z images of selected slices of microbeam of microbeam tested in vacuum at $\sigma_a = 470$ MPa ($\varepsilon_a = 0.30\%$) for 6×10^7 cycles

Comparatively, the same procedure and analysis were performed on a microbeam tested in air at σ_a = 315 MPa (ε_a = 0.18%) for 1.3×10^8 cycles. Figure 3.16 shows the *postmortem* images of the microbeam, while Figure 3.17 shows the EBSD information for selected slices. After analyzing all slices, almost all cracks are transgranular. Voids are also clearly observed in each of the slices and almost all of them formed in within the grains.
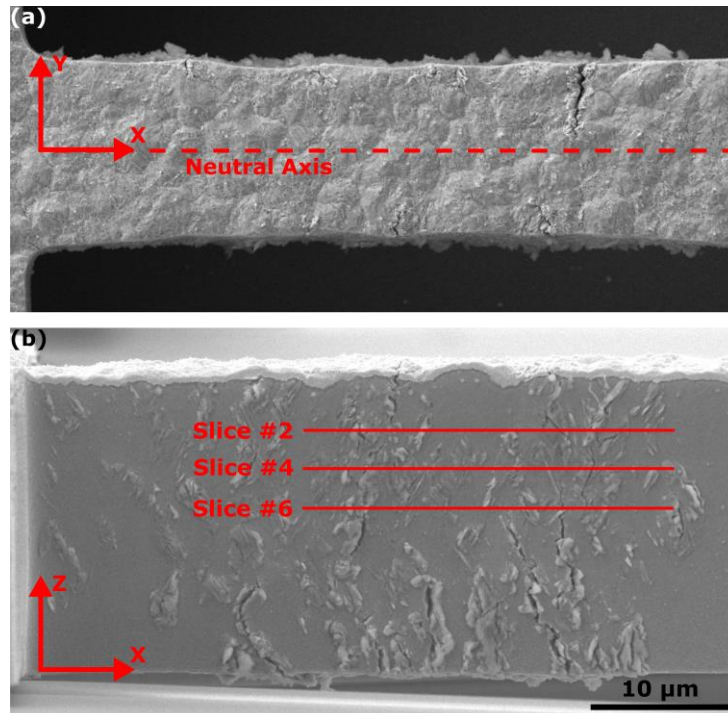
Figure 3.16 – (a) Top view and (b) sidewall of microbeam tested in air at σ_a = 315 MPa (ε_a = 0.18%) for 1.3×10^8 cycles
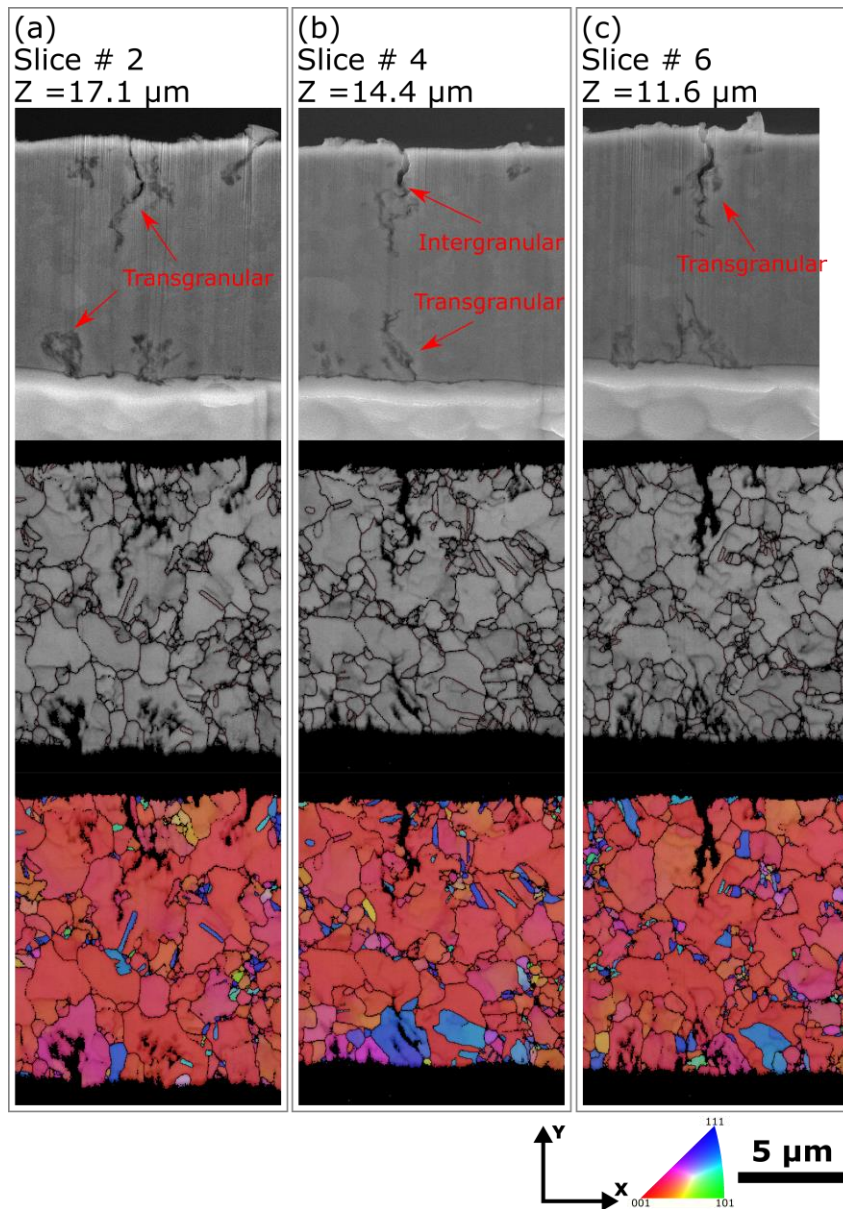
Figure 3.17 – (a)-(c) SEM, band contrast and IPF Z images of selected slices of microbeam of microbeam tested in in air at σ_a = 315 MPa (ε_a = 0.18%)

Analyzing another microbeam tested in air at σ_a = 410 MPa (ε_a = 0.25%) for 2.4 × 10^5 cycles (see Figures 3.18 and 3.19), most cracks were transgranular although thinner and shorter cracks were intergranular.
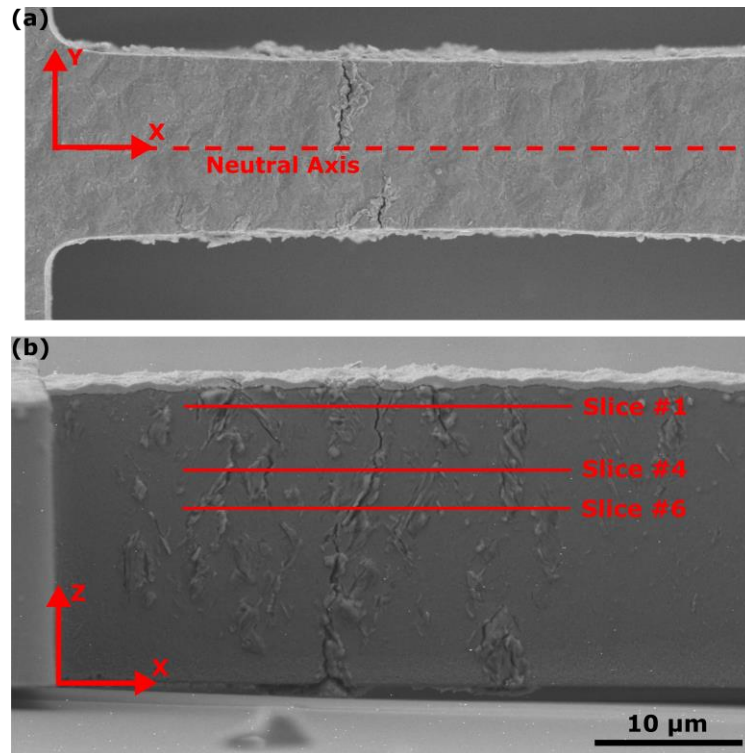
Figure 3.18 – (a) Top view and (b) sidewall of microbeam tested in air at $\sigma_a = 410$ MPa ($\varepsilon_a = 0.25\%$) for 2.4×10^5 cycles

The results from the crack path analysis demonstrate that microbeams tested at relatively lower stress/strain amplitudes have cracks that are transgranular in nature, while microbeams tested at higher stress/strain amplitudes present mixed cracking, with increased intergranular cracking. Additionally, voids found in the vicinity of cracks are observed to nucleate inside the grains.
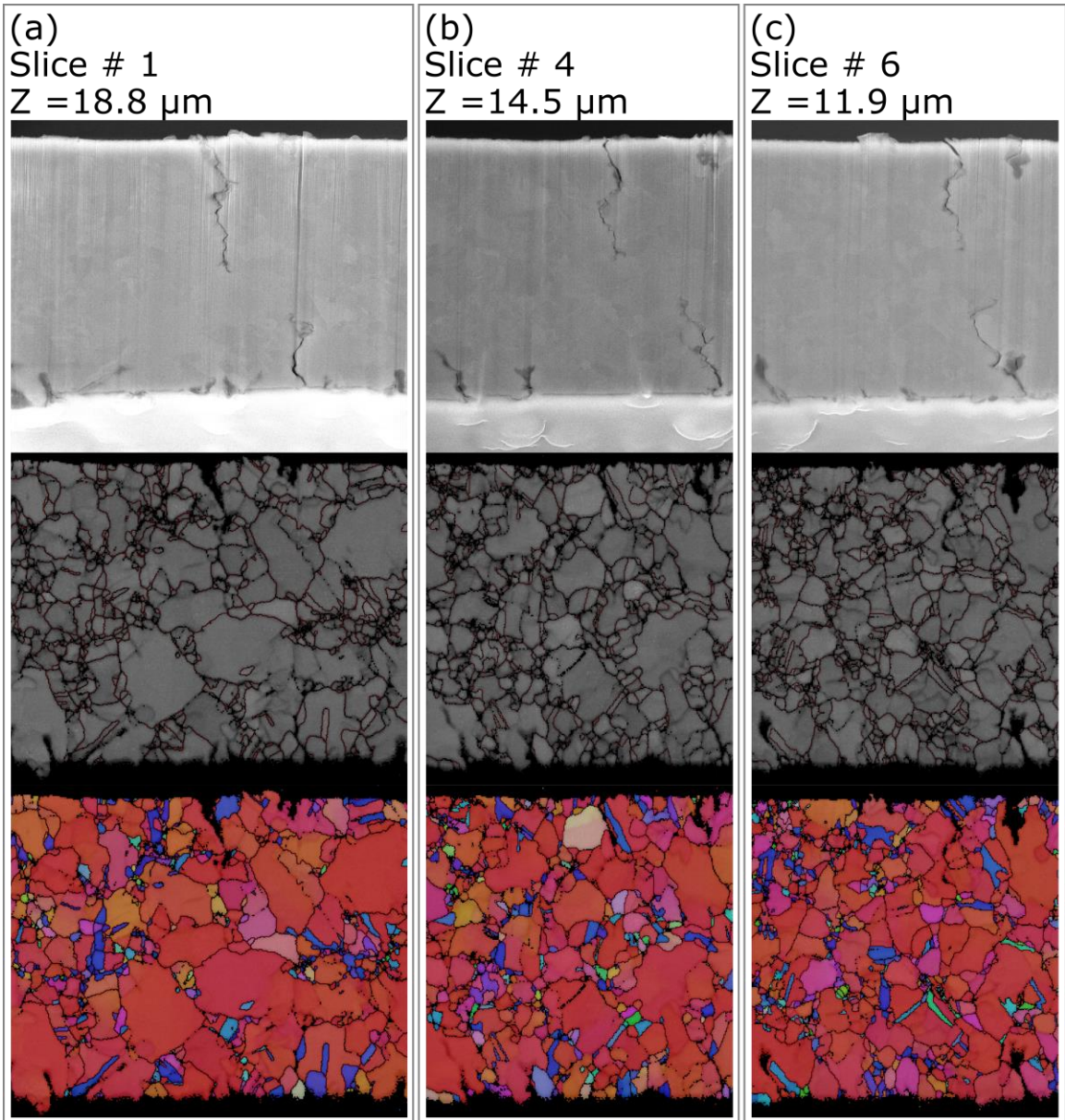
Figure 3.19 – (a)-(c) SEM, band contrast and IPF Z images of selected slices of microbeam of microbeam tested in in air at σ_a = 410 MPa (ε_a = 0.25%)

3.6 Discussion

These results highlight that fatigue crack nucleation and propagation are controlled by the formation of voids in the HCF/VHCF regime, either underneath surface extrusions or ahead of the crack tip, and are associated with ultraslow crack growth ($\sim 10^{-14}$ m/cycle in a vacuum, 10^{-12} m/cycle in air). The formation of voids at room temperature has already been documented in the fatigue studies of bulk metals [40, 41] as well as of metallic thin films on substrates [42-44] and results from the condensation of vacancies that form in the active slip bands under cyclic loading. In the particular case of metallic thin films on a substrate, the voids preferentially form at the film/substrate interface, presumably because that interface does not act as a sink for vacancies [44]. In persistent slip bands (PSBs), vacancies usually arise from the irreversible plastic deformation either by jog dragging on screw dislocations moving in the channels or annihilation of edge dislocation dipoles in the walls [14, 45-47]. Several fatigue crack initiation mechanisms have been proposed based on the presence of these excess vacancies within the PSBs, invoking either the formation of critical-radius voids [48], stress concentration developing at the surface near the edges of the extrusions [49], or the formation of intrusions resulting from vacancy-diffusion-related residual stresses [50]. Void-controlled fatigue crack nucleation has also been observed in ultrafine grained (UFG) Cu in the HCF/VHCF regime as shown in Figure 3.20 [51, 52]. In that case, the cyclic slip of an individual slip band led to the formation of voids along that band, especially in the VHCF regime. Our results suggest a fatigue crack nucleation mechanism similar to that invoked for VHCF of UFG Cu, relying on void formation along individual slip bands underneath the extrusions.
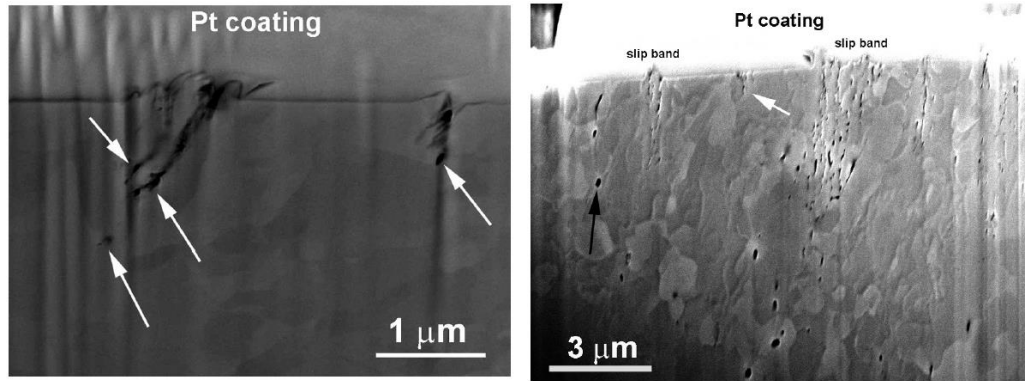
Figure 3.20 – Voids in UFG Cu [52]

The governing fatigue mechanism in the Ni microbeams in the HCF/VHCF regime is unlikely to be associated with large enough cyclic plastic deformation at the crack tip (associated with irreversible emission of dislocations). In fact, the FIB cross-section SEM images suggest crack growth controlled by void formation ahead of the crack tip and linkage of these voids with the main crack. This ultraslow crack growth mechanism is a direct consequence of size effects governing the fatigue behavior of these Ni microbeams. It is likely that the stress concentration effect at the tip of a growing fatigue crack is greatly reduced by the effect of the extreme stress gradients thereby preventing any significant cyclic crack tip opening displacement. Hence, it is logical to assume that the driving force for the fatigue crack extension in the microbeams is drastically reduced with an increasing crack size. As a result, the limited amount of cyclic slip ahead of the crack tip may only allow vacancy formation. Therefore, the ultraslow rates are likely the result of an incubation time required between crack growth events to aggregate and condensate vacancies into voids of a critical size. This explanation is consistent with the significant effect of normalized stress gradients (i.e., microbeam geometry) on the resulting S-N curves [31].

These results also emphasized the critical effect of air on the fatigue properties, with 1 order of magnitude longer fatigue crack initiation life, 2 orders of magnitude slower crack growth rates and 1 order of magnitude longer life to reach extrusions of the same height in a vacuum. For stage I crack growth associated with the common crack opening mode, the reported environmental effects are associated with mechanisms involving chemisorbed oxygen at the surface of the newly exposed slip steps that increase the slip irreversibility at the crack tip, thereby preventing rewelding [53-55]. Instead, in this study, both fatigue crack nucleation and propagation are dominated by void formation, and the surface of the voids was shown to be oxygen rich for the tests in air. Irradiation studies (that introduce large concentrations of vacancies) of metals at large temperatures have shown that oxygen stabilizes void nucleation compared to the other vacancy cluster defects, by decreasing the void surface energy through a chemisorption process [56-60]. Therefore, a similar scenario is expected during the fatigue damage of the Ni microbeams. In air, the formation of voids is facilitated by the presence of oxygen (which is consistent with the observation of large oxygen concentrations at the location of the voids), resulting in faster extrusion height growth and faster crack growth rates. The void formation is likely to be limited to the surface regions and near the crack tip due to the small diffusion distance for oxygen at room temperature. In a vacuum, oxygen is present at much lower concentrations (either on the surface of the specimens or as impurities in the electroplated Ni), requiring longer times or a larger concentration of vacancies to stabilize the voids and resulting in much lower extrusion height and crack growth rates.

Voids seem to form preferentially inside the grains at regions in the vicinity of cracks or underneath extrusions and are associated with condensation of vacancies inside

a grain due the limited cyclic plasticity. The transgranular cracking present in microbeams tested in the HCF/VHCF is associated with the void dominated mechanism. In the microbeams tested at higher stress/strain amplitudes, the dominating mechanism is still the formation of voids ahead of the crack tip, however, the mixed intergranular and transgranular cracking suggests that the void controlled mechanism is not the only mechanism at play in fatigue crack propagation.

3.7   Conclusions

The *in situ* technique allowed for the detailed study of the HCF/VHCF behavior in Ni microbeams. Environmental effects were studied highlighting the strong influence of air on fatigue behavior in comparison with tests ran in vacuum. The air accelerates fatigue crack nucleation by decreasing fatigue initiation life by at least one order of magnitude and the S-N curve highlights fatigue lives that are three orders of magnitude longer in vacuum at the same stress/strain amplitudes. Additionally, ultraslow crack propagations rates were measured (10^{-14} m/cycle in a vacuum, 10^{-12} m/cycle in air) and extrusion heights were analyzed throughout a fatigue test, with extrusions growing faster in microbeams tested in air.

The fractography results revealed that the fatigue crack nucleation and propagation in the HCF/VHCF regime are controlled by the formation of voids underneath extrusions or ahead of the crack tip, justifying the non-continuous crack growth with ultraslow rates. In microbeams tested in air, the voids are shown to be rich in oxygen, which facilitates their formation and accelerates crack nucleation and propagation. The voids seem to

preferentially form in a transgranular nature and are associated with transgranular cracking in the microbeams.

This void dominated fatigue process is thought to be a consequence of the effects of extreme stress gradients in the microbeams. The driving force for the fatigue crack extension in the microbeams is drastically reduced with an increasing crack size. However, the limited amount of cyclic slip ahead of the crack tip only allows for vacancy nucleation, with subsequent formation of voids allowing the nucleation and propagation of fatigue cracks.

CHAPTER 4.   LOW CYCLE FATIGUE BEHAVIOR

As mentioned in the previous chapter, the void dominated fatigue mechanism found in Ni microbeams under bending in HCF/VHCF is considered to be a consequence of the reduction in driving force for crack growth caused by the effects of extreme stress gradients. Hence, we hypothesize that the conditions applied in HCF/VHCF are below a threshold limit for the conventional mechanisms to operate. Consequently, the application of larger strains amplitudes (larger driving force) to these microbeams is expected to result in a transition in the governing fatigue mechanisms. Additionally, in the HCF/VHCF regime, the strong environmental effects and the observation of voids in subsurface areas and near the crack tip suggest that the diffusion of oxygen or water is essential for the formation of voids.

In this chapter, the fatigue behavior of the same Ni microbeams are further investigated under the Low Cycle Fatigue (LCF) regime. The micromechanical external actuation technique (Section 2.3) was used in order to test microbeams at higher applied strain amplitudes and lower fatigue lives than what was possible using the resonance method. The propagation rates, fatigue properties and nanoscale mechanisms were analyzed over a wide range of applied strain amplitudes and comparisons were traced between the LCF and the HCF/VHCF regimes. In addition, the study of frequency effects on the fatigue lives of the microbeams was investigated by contrasting results at similar strain amplitudes from the two techniques which employ significantly different frequencies.

4.1 LCF Test Results

The change in load amplitude throughout a fatigue test was evaluated for a number of microbeams. Figure 4.1a shows the evolution in load amplitude needed to displace the microbeam as function of cycles for a test performed at $\sigma_a = 715$ MPa and $\varepsilon_a = 0.96\%$. Again, the σ_a and ε_a values presented here are the maximum values that the microbeam experiences at the sidewall when tested. The load amplitude decreases steadily until ~600 cycles (15% decrease in load amplitude) and then shows a rapid decrease due to the propagation of cracks, reaching the failure threshold at $N_f = 680$ cycles. The *postmortem* images of the microbeam are shown in Figure 4.1b and c, where through thickness cracks and extrusions/intrusions are observed on both sides of the microbeam.
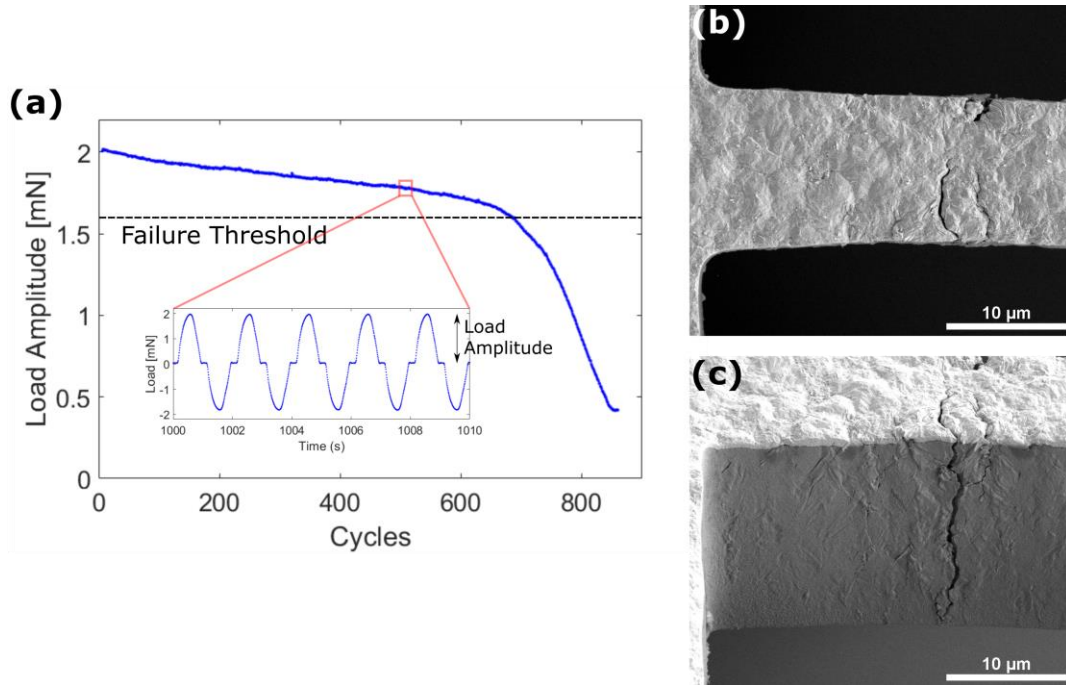
Figure 4.1 – (a) Load amplitude evolution of a test performed at $\sigma_a = 715$ MPa and $\varepsilon_a = 0.96\%$; (b) and (c) Top and side views of failed microbeam

Figure 4.2 shows results from another microbeam tested at $\sigma_a = 430$ MPa, $\varepsilon_a = 0.26\%$ and $N_f = 3.4 \times 10^5$ cycles. Only the first 150 cycles are shown here. Both the load

amplitude and the angle of rotation stay constant suggesting that there is no perceivable cyclic hardening or softening behavior. This confirms assumptions in past works [28, 31] that the monotonic and cyclic behavior of these Ni microbeams is similar in the HCF/VHCF regime.
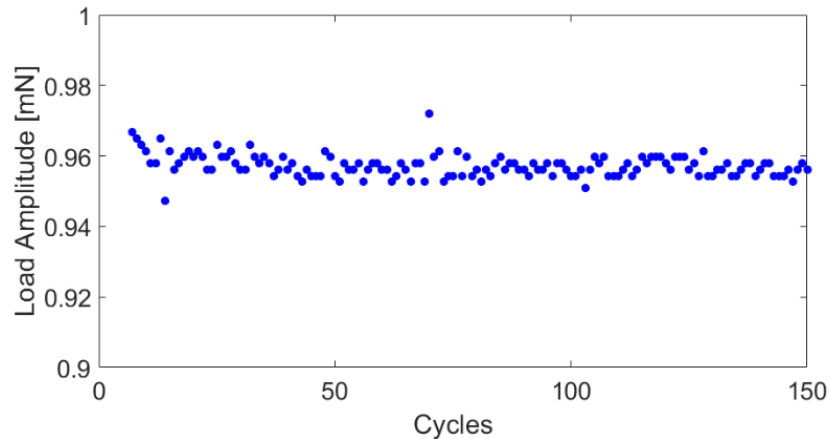
Figure 4.2 – First 150 cycles of microbeam tested at σ_a = 430 MPa and ε_a = 0.26%

In the microbeam tested at ε_a = 0.26%, the nucleation of a fatigue crack is expected to occur after ~ 2.5×10^5 cycles in air, based on previous observations of crack nucleation in the HCF/VHCF regime (2-4% decrease in f_o or 4-8% decrease in load amplitude) [32]. However, in the sample tested at ε_a = 0.96%, an 8% decrease in load amplitude happens at only ~300 cycles, revealing that cracks nucleate much faster in the LCF regime.

4.2   Stress and Strain-Life Curves

The stress and strain life curves were evaluated for both studied regimes and are shown in Figure 4.3a and b, respectively. The external actuation technique allowed for fatigue tests to be performed ranging from 400 to 715 MPa in σ_a and from 0.25% to 0.96% in ε_a, while previously reported tests with the electrostatic technique range from 200 to 450 MPa in σ_a and from 0.01% to 0.28% in ε_a. Therefore, with the two techniques the

microbeams were tested over six orders of magnitude in fatigue lives. In Figure 4.3, empty symbols denote the runout specimens and solid symbols represent fatigue failure.
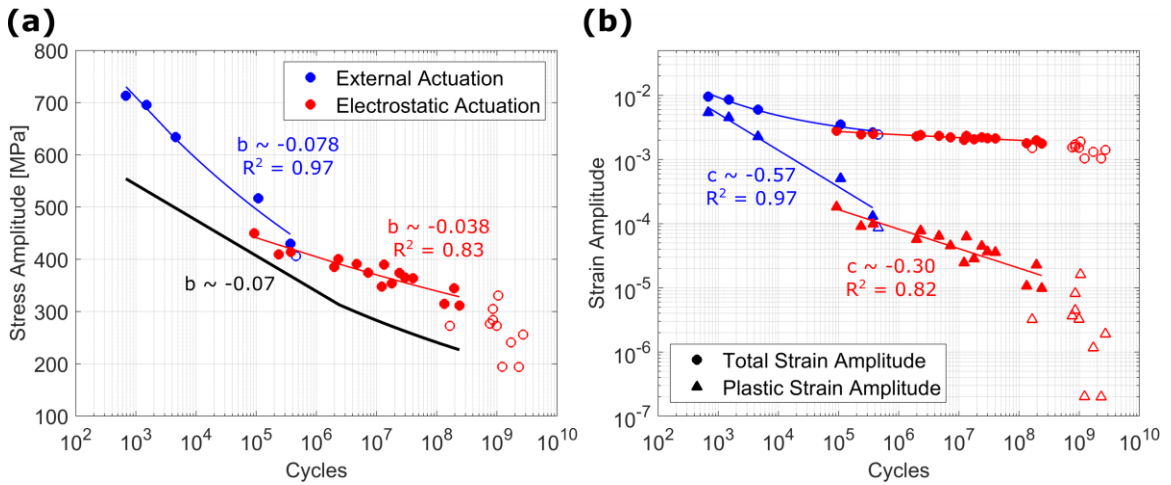
Figure 4.3 – (a) Stress and (b) Strain life curves for the LCF and HCF/VHCF

Both the LCF and HCF/VHCF regimes were fitted with the Basquin equation (Equation 4.1) and the Coffin-Manson equation (Equation 4.2) below:

$$\sigma_a = \sigma_f'(2N_f)^b \qquad \text{Equation 4.1}$$

$$\varepsilon_{pa} = \varepsilon_f'(2N_f)^c \qquad \text{Equation 4.2}$$

where σ_f' is the fatigue strength coefficient, b is the Basquin exponent, ε_f' is the fatigue ductility coefficient and c is the Coffin Manson coefficient; and show good correlations with the power fits. The Basquin exponent changes from -0.038 in the HCF/VHCF to -0.078 in the LCF regime, while the Coffin-Manson coefficient changes from -0.30 in the HCF/VHCF to -0.57 in the LCF regime The LCF regime presents a Basquin coefficient closer to behavior of Ni under the absence of stress/strain gradients, which has b~ -0.07 (also shown in Figure 4.3a) [61] and a Coffin Manson coefficient closer to typical values for bulk metals, which show c values ranging from -0.5 to -0.8 [12]. Overall, the fatigue

curves change from a shallower behavior in the HCF/VHCF to a more conventional behavior in the LCF regime. The drastic change in fatigue properties and behavior suggest that there is a change in the physical mechanisms for crack nucleation and propagation caused by the increase in applied strain amplitude. Therefore, the dominating fatigue mechanism may no longer be the void controlled mechanisms reported for the HCF/VHCF regime [32].

Additionally, there is a small overlap in the curves (10^5 to 10^6 cycles) where both techniques were applied and the frequency effects can be studied, as indicated in the next section.

4.3 Frequency Effects

The frequency effects on fatigue lives were investigated by employing the two techniques at similar stress and strain amplitudes. Figure 4.4a shows the plot of the normalized load amplitude $\left(\frac{N_a}{N_{initial}}\right)$ or resonance frequency $\left(\frac{f}{f_{initial}}\right)$ as a function of cycles, comparing two experiments with the different techniques. One sample was tested at $\sigma_a = 415$ MPa and $\varepsilon_a = 0.25\%$ with $N_f = 3.8 \times 10^5$ using the electrostatic technique (frequency of ~ 8 kHz) and had a total runtime about 1 minute. The other sample was tested at $\sigma_a = 430$ MPa and $\varepsilon_a = 0.26\%$ with $N_f = 3.4 \times 10^5$ using the external actuation technique (frequency of 0.5 Hz) and had a total runtime 9 days. Sidewall images of both microbeams after the fatigue tests are shown in Figure 4.4b and c. Both microbeams' sidewalls exhibit cracks and similar extrusion/intrusion densities. Both tests ran at frequencies that differ by four orders of magnitude but at similar stress/strain amplitude failed at approximately the same number of cycles, indicating that frequency does not play a significant role in the fatigue life of these Ni microbeams.
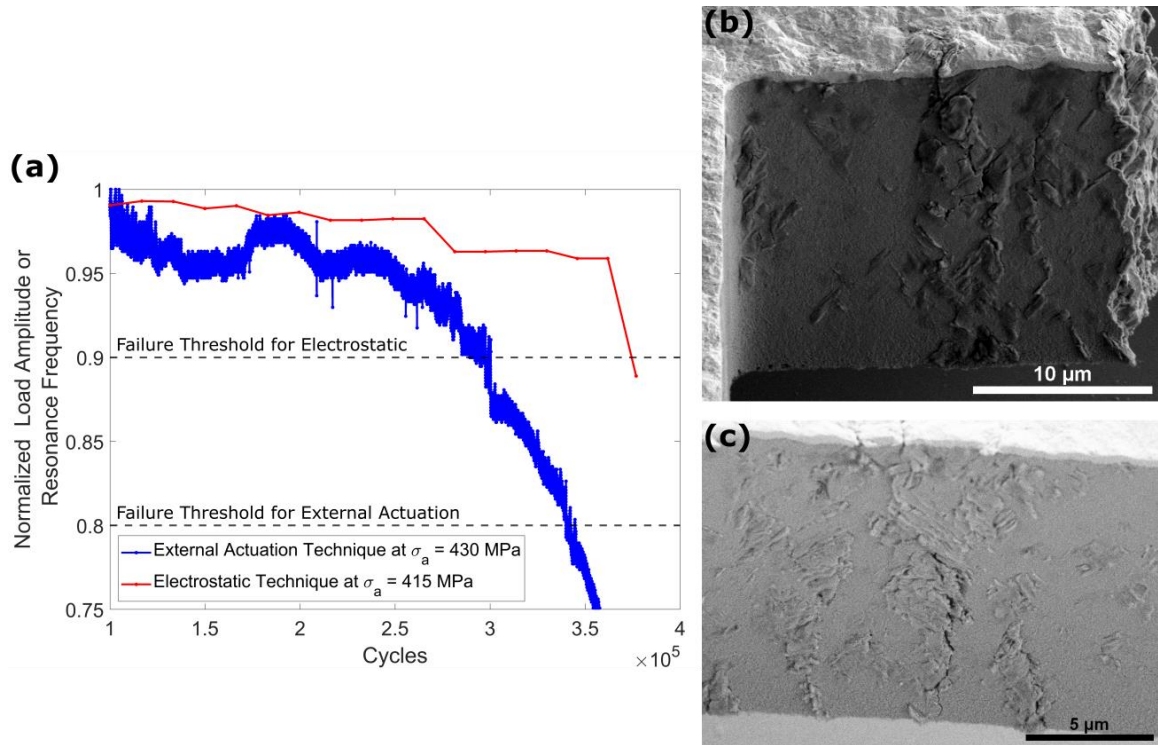
Figure 4.4 – (a) Frequency and load amplitude evolution curves for sample tested with the two techniques; (b) Sidewall image of the sample tested at σ_a = 430 MPa and ε_a = 0.26% with the external actuation technique; (c) Sidewall image of the sample tested at σ_a = 415 MPa and ε_a = 0.25% with the electrostatic technique

4.4 Fatigue Crack Propagation Rates

The effect of the applied strain amplitude was further investigated in regards to the crack propagation rates. The local crack propagation rates were measured for 2D cracks that spanned the entire thickness of the microbeam. Therefore, by observing crack evolution at the top surface of the microbeam through SEM images and by counting the number cycles in between two stages of a fatigue test, the average crack growth rates can be found [32]. Figure 4.5 shows the images of the microbeam tested at σ_a = 715 MPa, ε_a = 0.96% and with N_f = 680 cycles (same microbeam shown in Figure 4.1). The average crack growth rate in between the beginning and the end of the fatigue test was found to be $\frac{da}{dN} =$ 12 $nm/cycle$ ($da = 10 \ \mu m$ and $dN = 850$ cycles). In addition, Figure 4.5b shows a

64

transverse FIB cross-section exactly through the crack highlighted in Figure 4.5a. The high-resolution SEM image at the cross-section, shown in Figure 4.5c, reveal striations along the path of the crack towards the neutral axis of the microbeam. These fatigue striations are at an average distance $d = 19\ nm$ apart which is equivalent to an average crack growth rate of $\frac{da}{dN} = 19\ nm/cycle$.
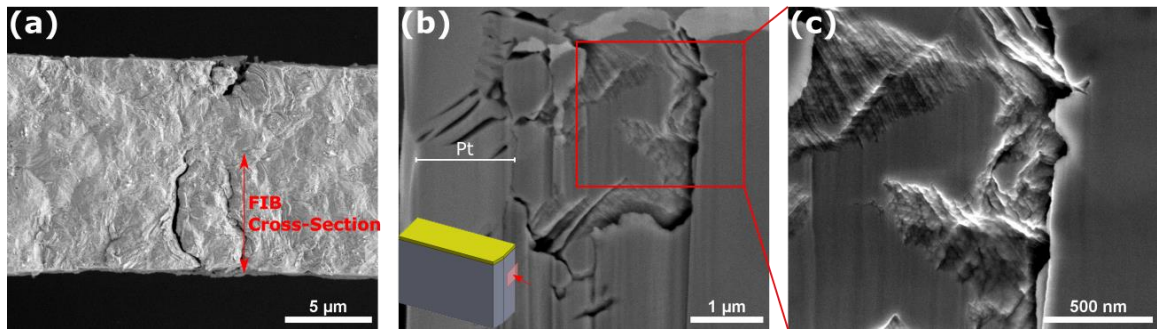
Figure 4.5 – (a) Top view of microbeam showing the location of the FIB cut; (b) Transverse FIB cross-section at the crack; (c) Fatigue striations at the fracture surface

Hence, two independent crack growth rate measurements provide crack growth rates in the 12-20 nm/cycle range in the LCF regime. These values are four orders of magnitude larger than in the HCF/VHCF regime, which exhibits crack growth rates of the order of 10^{-12} m/cycle in air [32]. Additionally, the crack growth rates in the LCF regime are more comparable among rates expected for the growth of microstructurally small cracks (stage I cracks). Stage I cracks usually have larger crack growth rates than long cracks (stage II cracks) in macroscopic metals, which exhibit rates from 1 nm to 1 µm/cycle [12]. These results suggest once more that the dominating mechanism for crack nucleation and propagation are not equivalent when comparing the two studied regimes.

4.5 Fractography

4.5.1 FIB Cuts and Fracture Surfaces

A series of FIB cross-sections were performed on microbeams tested over a wide range of fatigue lives in order to evaluate the subsurface fatigue damage and to investigate the nanoscale fatigue mechanisms for nucleation and propagation of cracks. Figure 4.6a shows a vertical FIB cross-section of the same microbeam shown in Figure 4.1b and Figure 4.5 (tested at $\sigma_a = 715$ MPa, $\varepsilon_a = 0.96\%$ and with $N_f = 680$ cycles), while Figure 4.6b shows a vertical FIB cross-section of a sample tested at $\sigma_a = 365$ MPa and $\varepsilon_a = 0.21\%$ with $N_f = 3 \times 10^7$ cycles using the electrostatic technique. Both samples present cracks spanning the thickness of the microbeam that were propagating towards the neutral axis. Figure 4.6a shows two cracks (one extending from the top and another from the bottom) with a fairly straight crack path without many deviations, except at the region where the two cracks meet. In contrast, Figure 4.6b shows a very tortuous crack path and the clear presence of voids, which are linked through thin cracks [32], highlighting again the difference in fatigue crack path behavior between the LCF and HCF/VHCF regimes.
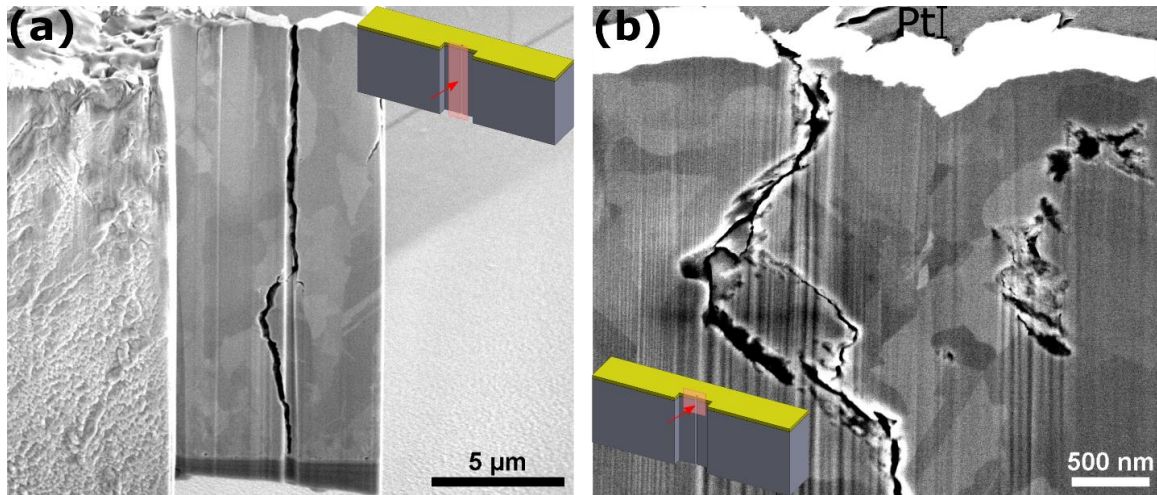
Figure 4.6 – (a) Vertical FIB cross-section of microbeam tested at σ_a = 715 MPa, ε_a = 0.96% with the external actuation technique, (b) Vertical FIB cross-section of microbeam tested at σ_a = 365 MPa and ε_a = 0.21% with the electrostatic technique

Figures 4.7a and b show SEM images of the fracture surfaces of two microbeams. Both microbeams exhibited through thickness cracks that spanned almost the whole width of the microbeams (both only had a small remaining ligament around the neutral axis). The fracture surfaces belong to the part of the microbeams that were still attached to the substrate after the careful sectioning of the ligament at the crack surface and removal of the remaining portion of the microbeam. The sample in Figure 4.7a was tested at σ_a ~710 MPa and ε_a ~ 0.97% for N = 1000 cycles using the external actuation technique, while the sample in Figure 4.7b was tested at σ_a = 355 MPa and ε_a = 0.21% with N_f = 1.8×10^7 using the electrostatic technique. The fracture surface in Figure 4.7a exhibits a very rugged surface with a zig-zag pattern followed by the crack that propagated towards the middle section of the microbeam, showing what appears to be intergranular crack growth. Figure 4.7b shows a less protruded fracture surface with what seems to be some columnar grains flattened along the crack path. This fracture surface also shows a clear and abundant presence of voids along the crack path, highlighted in the image. These voids are not

present in Figure 4.7a, confirming than in the LCF regime (high strain amplitudes) the mechanism for crack propagation is no longer controlled by the formation of voids and is instead, controlled by the crack tip stress intensification.
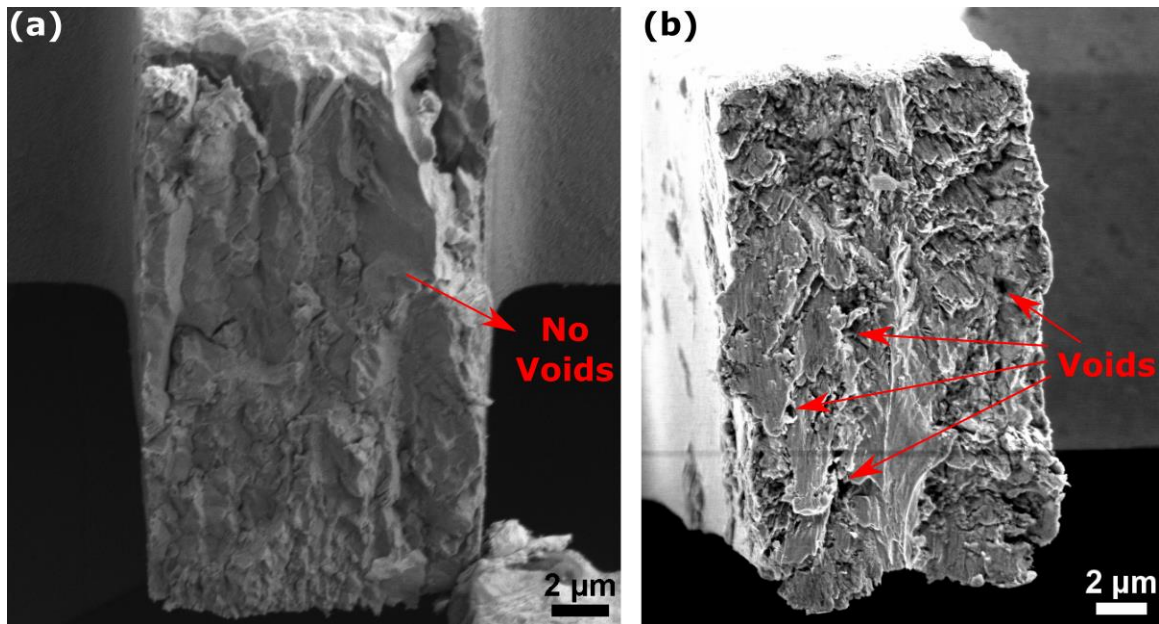
Figure 4.7 – Fracture surface of samples tested at (a) σ_a ~710 MPa and ε_a ~ 0.97% and (b) σ_a = 355 MPa and ε_a = 0.21% with arrows highlighting the presence of voids

The external actuation technique was also employed to study fatigue samples at lower stress/strain amplitudes although, with tests ran at 0.5 Hz, the runtime of each test significantly increased. One microbeam was tested at σ_a = 430 MPa and ε_a = 0.26% and failed with N_f = 3.4×10^5 (same sample as Figure 4.4b). The sample exhibited cracks on both sidewalls that almost spanned the entire width with only a ligament remaining in the neutral axis. A vertical FIB cross-section was performed at a region close to the main crack and is shown in Figure 4.8 along with high resolution images at areas of interest. The two highlighted areas show portions of a crack that propagated towards the neutral axis. Voids are clearly observed in these two areas and are very similar to the voids observed in tests using the electrostatic technique. Therefore, this evidence demonstrates that void-

controlled crack growth is the main mechanism for crack propagation in this sample. In other words, void-controlled fatigue was observed in samples that were tested under the external actuation technique but at low enough stress/strain amplitudes.
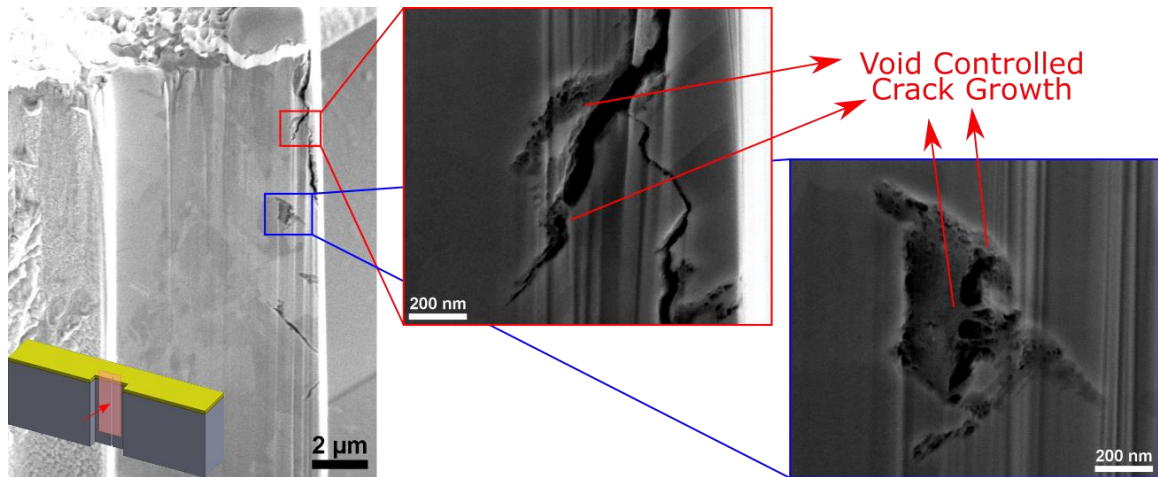
Figure 4.8 – Vertical FIB cross-section showing void dominated crack propagation in microbeam tested at $\sigma_a = 430$ MPa and $\varepsilon_a = 0.26\%$

4.5.2   FIB Slices Crack Growth Path

Similarly, as it was done in Section 3.5.2 with HCF microbeams, the crack path characteristics were analyzed for samples tested under the external actuation technique at high strain amplitudes. The 3D FIB-EBSD procedure (see Section 2.6) was used once more to obtain crack and grain information through the entire thickness of the microbeam.

Figure 4.9 shows the top view and sidewall of a microbeam tested with the external actuation technique at $\sigma_a = 695$ MPa ($\varepsilon_a = 0.85\%$) and cycled for 1.5×10^3 cycles. The locations of selected slices from the 3D FIB-EBSD procedure are also shown in Figure 4.9. Figure 4.10 shows the EBSD information from the selected slices highlighting the nature of the cracks. This specific microbeam was sliced 20 times (most microbeam were sliced about 13 times), allowing for a more detailed analysis on the nature and characteristics of

the crack path. All cracks found in the slices were of the intergranular nature without exceptions.
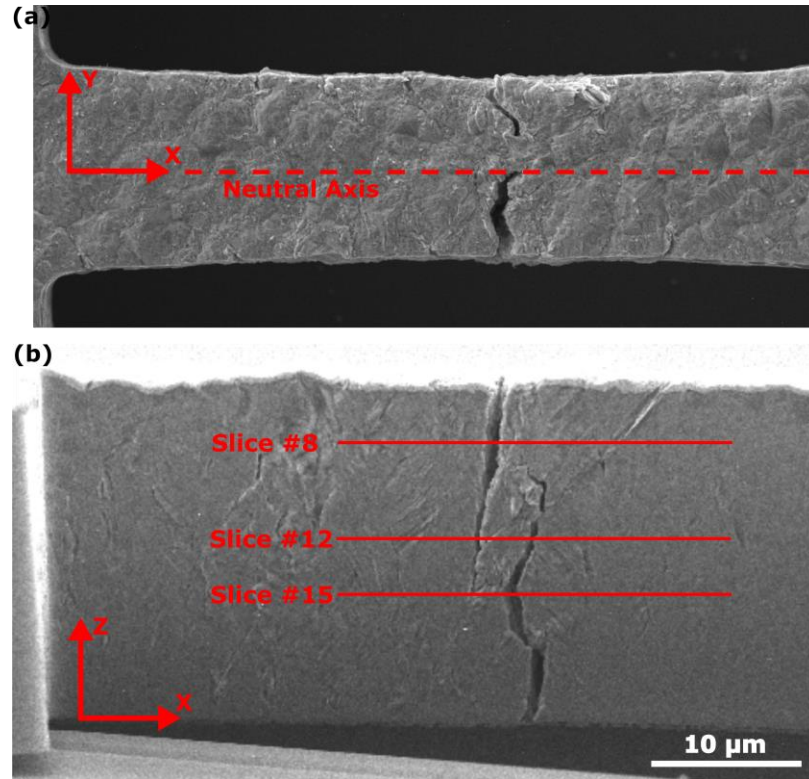
Figure 4.9 – (a) Top view and (b) sidewall of microbeam tested at σ_a = 695 MPa (ε_a = 0.85%) and cycled for 1.5×10^3 cycles

Figure 4.10 – (a)-(c) SEM, band contrast and IPF Z images of selected slices of microbeam of microbeam tested with the external actuation technique at σ_a = 695 MPa (ε_a = 0.85%) and cycled for 1.5×10^3 cycles

A second microbeam tested under the external actuation technique at $\sigma_a = 515$ MPa ($\varepsilon_a = 0.35\%$) and cycled for 1.1×10^5 cycles was also evaluated under the same procedure, with the information shown in Figure 4.11 and Figure 4.12. In this particular microbeam, the main crack spanned the entire width, completely fracturing the microbeam (fractured side of the microbeam can be observed on the right side of Figure 4.11a and b). This provided an opportunity to identify and analyze secondary cracks that were not associated with the main crack. In other words, cracks that nucleated and were not a result of the propagation of the main crack. The main crack appears to be intergranular based on images of the fracture surface, shown in Figure 4.11c (the two highlighted areas are a result of the propagation of fatigue cracks during the test, while the other areas are likely to be the remaining ligament that fast fractured at the end of the test). Analyzing all FIB-EBSD slices, many small cracks (less than 1 µm) were found and the great majority were intergranular cracks (as shown in Figure 4.12), although a few were transgranular.
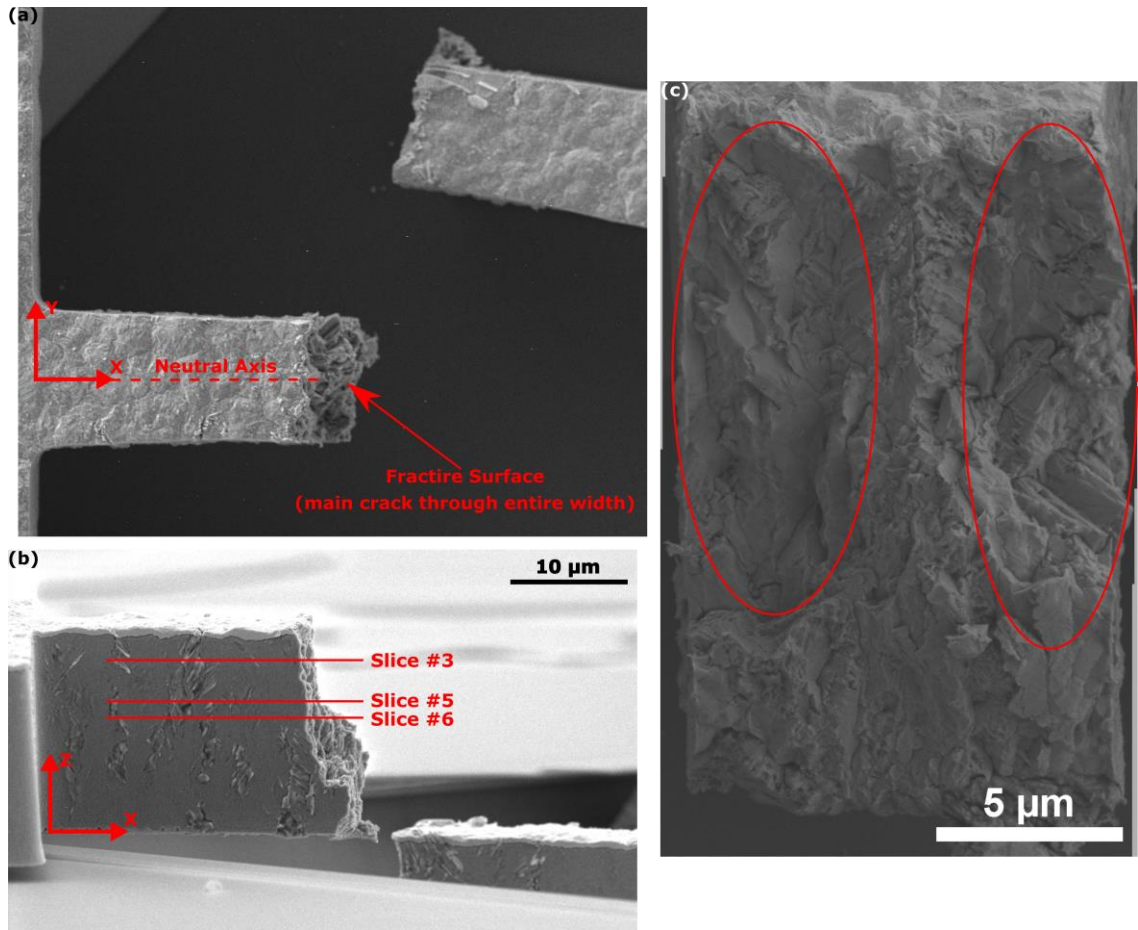
Figure 4.11 – (a) Top view and (b) sidewall of microbeam tested at $\sigma_a = 515$ MPa ($\varepsilon_a = 0.35\%$) and cycled for 1.1×10^5 cycles; (c) Fracture surface caused by the propagation of the main crack through entire width of microbeam
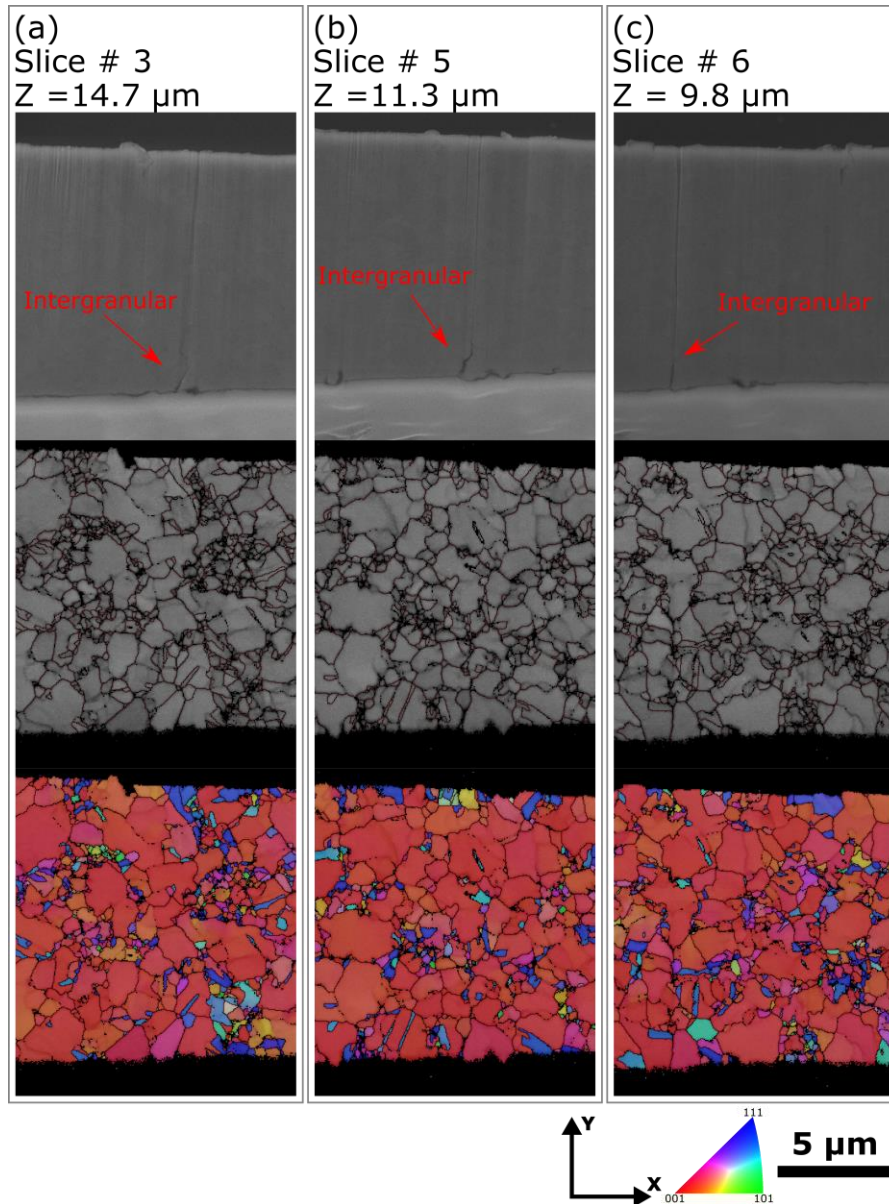
Figure 4.12 – (a)-(c) SEM, band contrast and IPF Z images of selected slices of microbeam of microbeam tested with the external actuation technique at $\sigma_a = 515$ MPa ($\varepsilon_a = 0.35\%$) and cycled for 1.1×10^5 cycles

These results reveal that at higher stress/strain amplitudes the crack path behavior is mostly intergranular and complements the results from the HCF crack path analysis. As the applied strain amplitude increases, the number of fatigue cracks with an intergranular nature tends to increase.

4.6   Discussion

The results of this work highlight pronounced differences in fatigue behaviors and mechanisms for the two studied fatigue regimes. The four orders of magnitude difference in average crack propagation rates and the stress/strain-life curve results with unusual Basquin and Coffin-Manson exponents in the HCF/VHCF due to the extreme stress gradients and more conventional exponents in the LCF regime reveal a transition in the governing fatigue mechanisms from void-controlled mechanisms in the HCF/VHCF to the conventional mechanisms in LCF.

Additionally, in microbeams tested at higher strain amplitudes, the extrusions observed on the sidewalls are much shallower when compared to the ones tested under the HCF/VHCF regime (compare Figure 4.13a with Figure 4.13b, respectively). While the microbeam in Figure 4.13b ($\sigma_a = 375$ MPa, $\varepsilon_a = 0.22\%$) shows extrusion heights up to 0.9 μm (measured from top view images), the microbeam in Figure 4.13a ($\sigma_a = 715$ MPa, $\varepsilon_a = 0.96\%$) only show extrusions with a maximum height of 0.4 μm. The extra cycling in the lower strain amplitude ranges with N_f ranging from 10^5 to 10^9 cycles, combined with the void-controlled governing mechanism, contribute to the increase in the average height of extrusions.
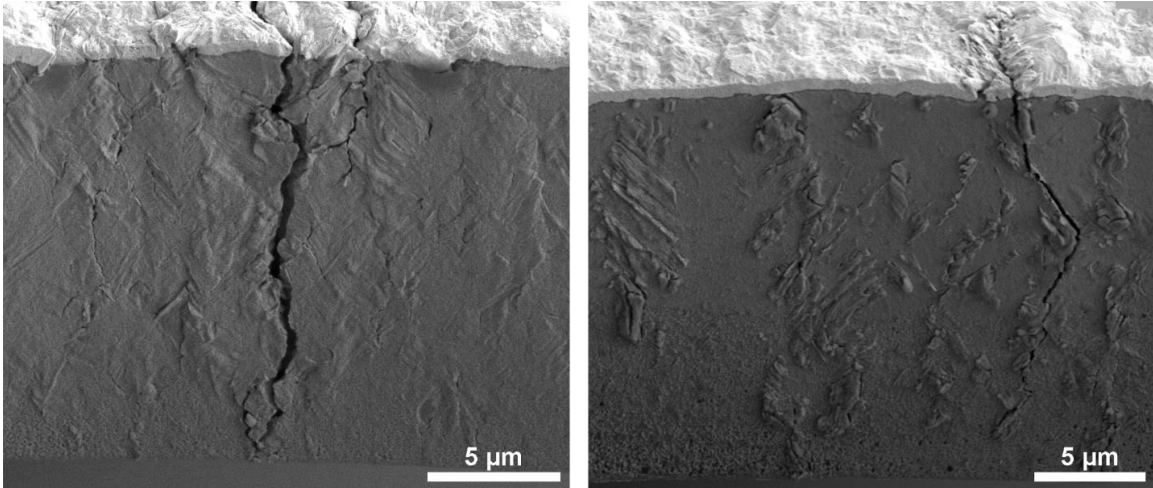
Figure 4.13 – Extrusion in microbeams' sidewalls tested at (a) $\sigma_a = 715$ MPa, $\varepsilon_a = 0.96\%$ and (b) $\sigma_a = 375$ MPa, $\varepsilon_a = 0.22\%$

The microbeams tested in the LCF regime exhibit mechanisms that resemble the conventional fatigue mechanisms associated with large cyclic plastic deformation at the crack tip. These fatigue mechanisms are characterized by the formation of extrusions caused by Persistent Slip Bands (PSB). Once a PSB forms due to cyclic slip, the strain is highly localized in sites close to PSBs, leading to extrusions and these sites become fatigue crack initiation sites. Concurrently, cyclic irreversibility at PSBs further contribute to the growth of extrusions and are associated with the generation of vacancies [53, 62]. In turn, when a crack has formed, the common crack tip stress intensification related with the irreversible dislocation emission cause a crack to propagate.

The dominating fatigue mechanism in the HCF/VHCF samples with lower applied strain amplitudes is the formation of voids ahead of the crack tip. This mechanism is characterized by ultraslow propagation rates and is likely caused by the prevention of stress concentration effects at the crack tip due to the effect of extreme stress gradients [32]. We therefore show in this work that, once the applied strain amplitudes are large enough, the effects of extreme stress gradients are not as influential and the dominant mechanisms

change to the conventional fatigue mechanisms characterized by larger crack propagation rates. Additionally, the intergranular cracking found in these microbeam is further evidence for a change in mechanisms. The evident increase in intergranular cracking is associated with the conventional fatigue mechanisms, contrasting the higher number of transgranular cracks found in microbeams tested at lower strain amplitudes. This result suggests that there is a threshold in applied strain amplitudes for the change in dominant fatigue mechanisms. The threshold becomes apparent in Figure 4.3, where there is an inflexion point in fatigue behavior at around $N_f = 10^5$ cycles in the stress/strain-life curves.

At the inflexion point, the two microbeams tested at significantly different frequencies and shown in Figure 4.4 present void-controlled fatigue as the dominating fatigue mechanism. The lack of frequency effects suggests that the formation of voids is independent of frequency, and therefore the diffusion of oxygen or water species into the material, thought to be necessary to stabilize voids resulting from the condensation of vacancies below extrusions or ahead of the crack tip [32], is not the limiting factor governing the overall fatigue process.

Therefore, at N_f higher than 10^5 cycles and at plastic strain amplitudes lower than 10^{-4}, the governing mechanism transitions from the conventional mechanisms in LCF to the void-controlled mechanisms in HCF/VHCF. The void dominated mechanism has been previously observed in the ultrasonic fatigue testing of bulk ultrafine grained Cu [51, 52] (Figure 3.20), although only in the VHCF regime with cycling higher than 10^8 cycles and plastic strain amplitudes lower than 10^{-6}. Hence, the size effects present in the current microbeam study highly influence the transition between the two governing mechanisms, increasing the plastic strain amplitude at which the transition occurs.

4.7   Conclusions

This chapter demonstrated an external actuation technique to investigate fatigue behavior of Ni microbeams under bending. Along with the previously reported electrostatic technique, Ni microbeams could be tested over fatigue lives ranging from 100 to 10^9 cycles. Results highlight stark differences in fatigue behavior and mechanisms when comparing LCF and HCF/VCHF. In the HCF/VHCF regime the dominant fatigue mechanism is void-assisted crack nucleation and propagation of transgranular nature characterized by ultraslow propagation rates and the fatigue curves are characterized by $b = $ -0.038 and $c = $ -0.30, while in the LCF regime, the dominant fatigue mechanisms are the well-documented fatigue mechanisms characterized by larger crack growth rates, behavior with $b = $ -0.078 and $c = $ -0.57 and intergranular characteristics. Results suggest the presence of a threshold in applied strain amplitude around 10^{-4} above which the effects of extreme stress gradients no longer influence the dominant fatigue mechanism. In addition, results highlight the lack of frequency effects in the fatigue behavior of Ni microbeams.

CHAPTER 5.   FATIGUE INDUCED GRAIN GROWTH

The previous investigations discussed in Chapters 3 and 4 presented the fatigue behavior dominated by the nucleation and propagation of cracks in the columnar micro-sized grained part of the microbeam (i.e., the top 17.5 µm of the 20-µm-thick microbeam). This chapter is mainly focused on the microstructural evolution of the bottom 2.5 µm layer made of ultrafine grains which can be seen as a thin layer undergoing fully-reversed cyclic bending at a strain amplitude, ε_a, and for a number of cycles dictated by the rest of the microbeam. The 3D EBSD-FIB procedure mentioned in previous chapters allowed for the observation of significant grain growth in the bottom layer after cycling. Hence, this chapter presents a fatigue grain growth investigation under fully reversed loadings for up to 10^9 cycles and strain amplitudes ε_a ranging from 0.15 to 0.85 % at two different testing frequencies (0.5 Hz vs 8 kHz), on the ultrafine grained regions of Ni microbeams. Additionally, finite element models performed by collaborators of the actual microstructures of selected microbeams are employed to further perform an attribution study for the roles of the underlying driving force and mechanisms controlling grain boundary mobility under cyclic loading.

5.1   Grain Growth Results

The numbers of cycles that will be presented in this chapter do not represent the fatigue life of the ultrafine grained layer, but instead the number of cycles applied at a given ε_a. Previous characterizations of the microresonators demonstrated (using the lack of reversible resonance frequency evolution) that no significant increase in temperature

occurs during the fatigue tests [30, 32], therefore the grain growth results shown next are fatigue driven grain growth at room temperature.

Figure 5.1 shows the band contrast images, as well as the grain orientation maps in the X direction of horizontal slices obtained at the bottom of the microbeam (~1 µm from bottom) for seven fatigued specimens. Figure 5.1a corresponds to a specimen tested at $\varepsilon_a =$ 0.31% for 1.2×10^7 cycles, at 8 kHz. Significant, abnormal grain growth has occurred along the edges of the microbeam, i.e., at the location of the largest applied strain. No grain growth occurred over a distance of ~1.5 µm from the neutral axis, clearly indicating that deformation-induced grain growth took place. Most of the large grains have an elongated shape along the X direction, with a maximum size of ~3 µm in the Y direction, indicating that the local strain 3 µm from the edges (approximately 0.15% for a microbeam width of 12 µm) is not large enough to induce grain growth. However, some grains are longer than 10 µm in the X direction, suggesting significant grain boundary migration under the maximum applied cyclic strain. The grain orientation map shows that most of the large grains have a near (001) orientation in the X direction (as well as a (001) orientation in the Z direction as expected given the strong initial fiber texture).
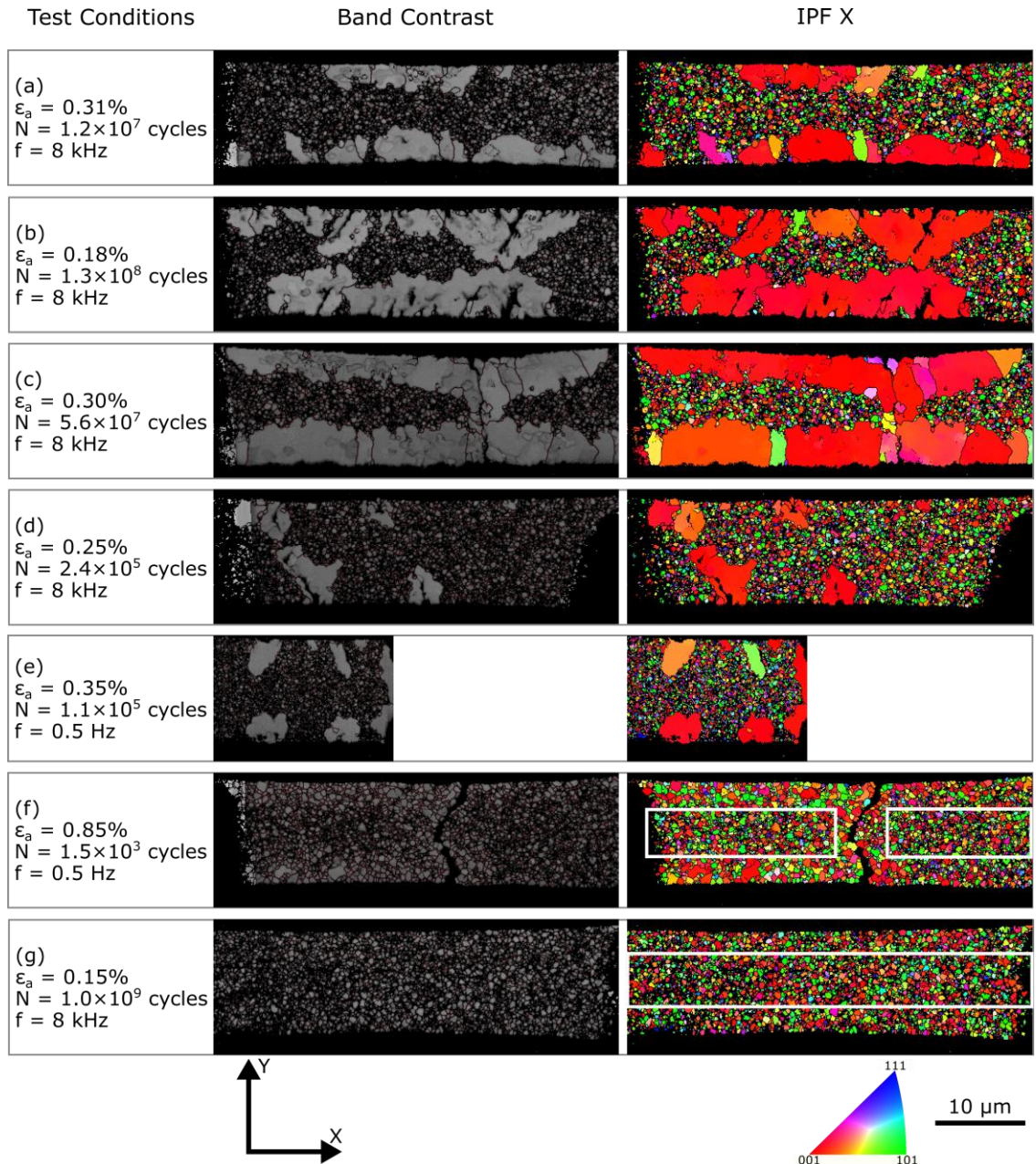
Figure 5.1 – (a)-(g): Band contrast images and grain orientation maps in the X direction of horizontal slices obtained at the bottom of the microbeam (~1 µm from bottom) for seven fatigued specimens.

Figure 5.1b presents a specimen tested at $\varepsilon_a = 0.18\%$ for 1.3×10^8 cycles, at 8 kHz. Similarly, significant abnormal grain growth occurred as well, with elongated shapes along the X direction and a (001) preferential orientation in the X direction. The main difference

with Figure 5.1a is that most large grains grew in the Y direction much closer the neutral axis, despite having a lower ε_a (0.18 vs 0.31%). This is likely the result of having fatigue cracks in the large grains that developed presumably because of the larger number of applied cycles (1.3×10^8 vs 1.2×10^7). It is not possible to know the origin of these fatigue cracks (i.e. whether they nucleated within the growing grains, or propagated from existing cracks that nucleated first in the top portion of the microbeam, where large columnar grains are present initially). Nevertheless, the effect of the fatigue crack growing towards the neutral axis is to increase the strain/stress fields ahead of the crack tip, which may provide additional driving force for grain growth in the Y direction. Hence, the presence of fatigue cracks can explain the irregular shape of the larger grains in the Y direction (compared to Figure 5.1a). This result is also clearly illustrated in Figure 5.1c, for a specimen tested at $e_a = 0.3\%$ for 5.6×10^7 cycles, at 8 kHz. Similar to the specimen shown in Figure 5.1a, this specimen has many large grains with elongated shapes, 3-4 µm in size in the Y direction, and as long as 10 µm in the X direction. However, this specimen has a fatigue crack that grew from each side of the microbeam and reached the neutral axis. Significant grain coarsening occurred in that region, with grains spanning the entire half-width of the microbeam. The large grains also exhibit a (001) preferential orientation in the X direction.

The three specimens studied so far experienced more than 10^7 cycles. Figure 5.1d is for a specimen that was tested at $\varepsilon_a = 0.25\%$ for 2.4×10^5 cycles, at 8 kHz, i.e., at least 50 times less cycling for similar ε_a (0.2-0.3%). Abnormal grain growth is also observed for 5 or 6 grains, which have a (001) preferential orientation in the X direction. Fatigue cracks are present in most of these large grains, explaining why some grains grew to the neutral axis. However, none of these large grains have an elongated shape in the X direction, likely

because of the smaller number of cycles experienced by this specimen. Hence, we can conclude that a significant amount of grain coarsening for the specimens showed in Fig. Figure 5.1a-c likely occurred between 10^5 and 10^7-10^8 cycles, suggesting a continuous growth process for selected grains. In other words, the number of cycles is an important factor determining the amount of fatigue induced grain growth, which is in agreement with the notion that accumulated plastic strain is expected to play a significant role [63].

The effect of testing frequency can be assessed by comparing Figure 5.1e (specimen tested at $\varepsilon_a = 0.35\%$ for 1.1×10^5 cycles, at 0.5 Hz) to Figure 5.1d ($\varepsilon_a = 0.25\%$ for 2.4×10^5 cycles, at 8 kHz). The test duration is 7200 times longer for the specimen shown in Figure 5.1e, i.e. 60 hours vs 30 s for the specimen shown in Figure 5.1d (the portion of the test duration spent at maximum applied strains are similar for both tests). However, the amount of grain coarsening is similar for both specimens, with a few large grains mainly having a (001) preferential orientation in the X direction. Figure 5.1e shows that the grains with no fatigue cracks reached at most 3-4 µm in size in the Y direction. This specimen was fractured in two parts during the fatigue test, hence only one remaining half of the microbeam is shown. Two grains surrounding the crack path grew to the neutral axis.

Figure 5.1f is for a specimen that was tested at much larger $\varepsilon_a = 0.85\%$ (compared to 0.18-0.35% for the other specimens), using the external actuation technique (testing frequency of 0.5 Hz). The specimen failed after only 1.5×10^3 cycles at this large ε_a value, with a crack path that appears to be intergranular. The amount of grain coarsening is clearly less severe, likely due to the lower number of cycles (despite a much larger ε_a). Comparison of the grain size distributions (see Figure 5.2) at the edges of the microbeam vs around the neutral axis (see areas in Figure 5.1f) show that grain growth did occur, with the largest

grain of about 2 µm in diameter along the edges. Grain growth was also present along the crack path, a behavior reminiscent of grain growth in nanocrystalline Pt films [64].
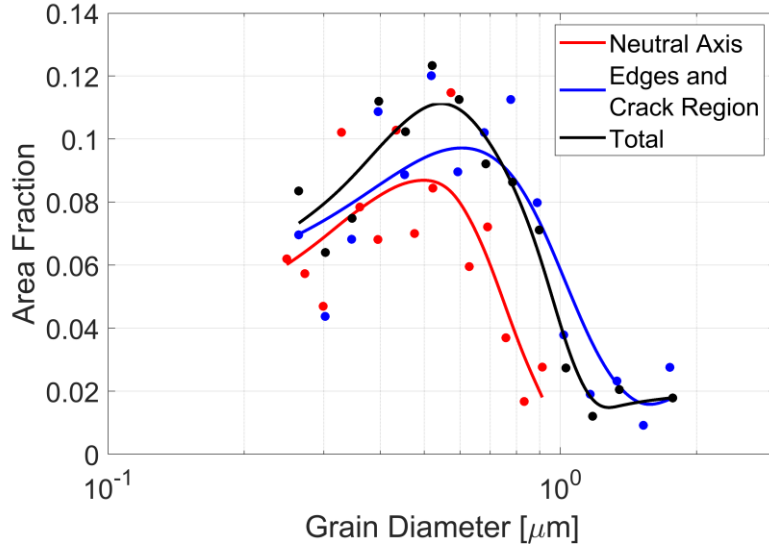
Figure 5.2 – Comparison of grain size distributions of the microbeam shown in Figure 5.1f, at the edges of the microbeam and surrounding the neutral axis

The last specimen shown in Figure 5.1g was tested at ε_a = 0.15% for 1.0×10^9 cycles, at 8 kHz. No grain growth was observed, as evidenced by comparing the grain size distribution at the edges of the microbeam vs around the neutral axis (see Figure 5.3). Hence, there appears to be a threshold in ε_a around 0.15-0.18% (grain growth was observed at 0.18%; see Figure 5.1b) below which no grain growth occurs, despite the application of 10^9 cycles. This threshold value is consistent with the local strain amplitude of 0.15% estimated in Figure 5.1a corresponding to the location from the edges of the microbeam where grain growth did not occur either.
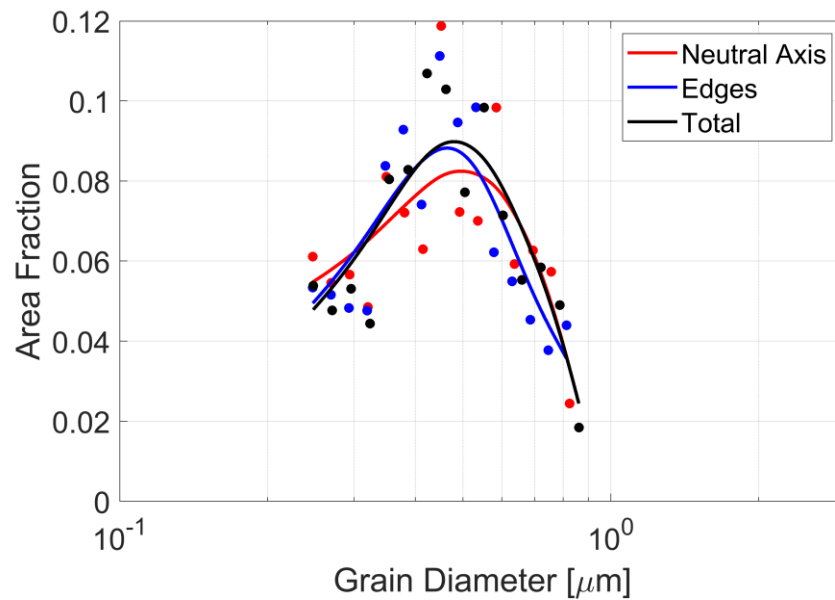
Figure 5.3 – Comparison of grain size distributions of the microbeam shown in Figure 5.1g, at the edges of the microbeam and surrounding the neutral axis

Figure 5.4 summarizes some of the observations from Figure 5.1 regarding the amount of grain growth. Figure 5.4a shows the maximum equivalent grain diameter as a function of applied cycles. The maximum grain diameter in the untested microstructure is about 1 µm. The plot indicates an increase in maximum diameter with increasing cycling from 10^3 to 10^8, confirming that the number of cycles is an important factor in the growth process. However, ε_a must be above a certain threshold (0.15-0.18% in our case), as cycling for 10^9 cycles at $\varepsilon_a = 0.15\%$ did not result in any grain growth. Given that the growth of these large grains appears to be a continuous process over cycling, an average grain growth rate (the difference between the maximum grain diameter of the tested and the untested microbeam divided by the number of cycles) is calculated for each specimen and plotted as a function of ε_a in Figure 5.4b. This figure shows that the average rate increases with ε_a, which is therefore an important metric governing the driving force for grain growth. A recent fatigue study on ultrafine grained Au films have also shown room temperature grain

coarsening [65] and show average grain coarsening rates that follow similar trends as the rates found in the current study, as shown in Figure 5.4b.
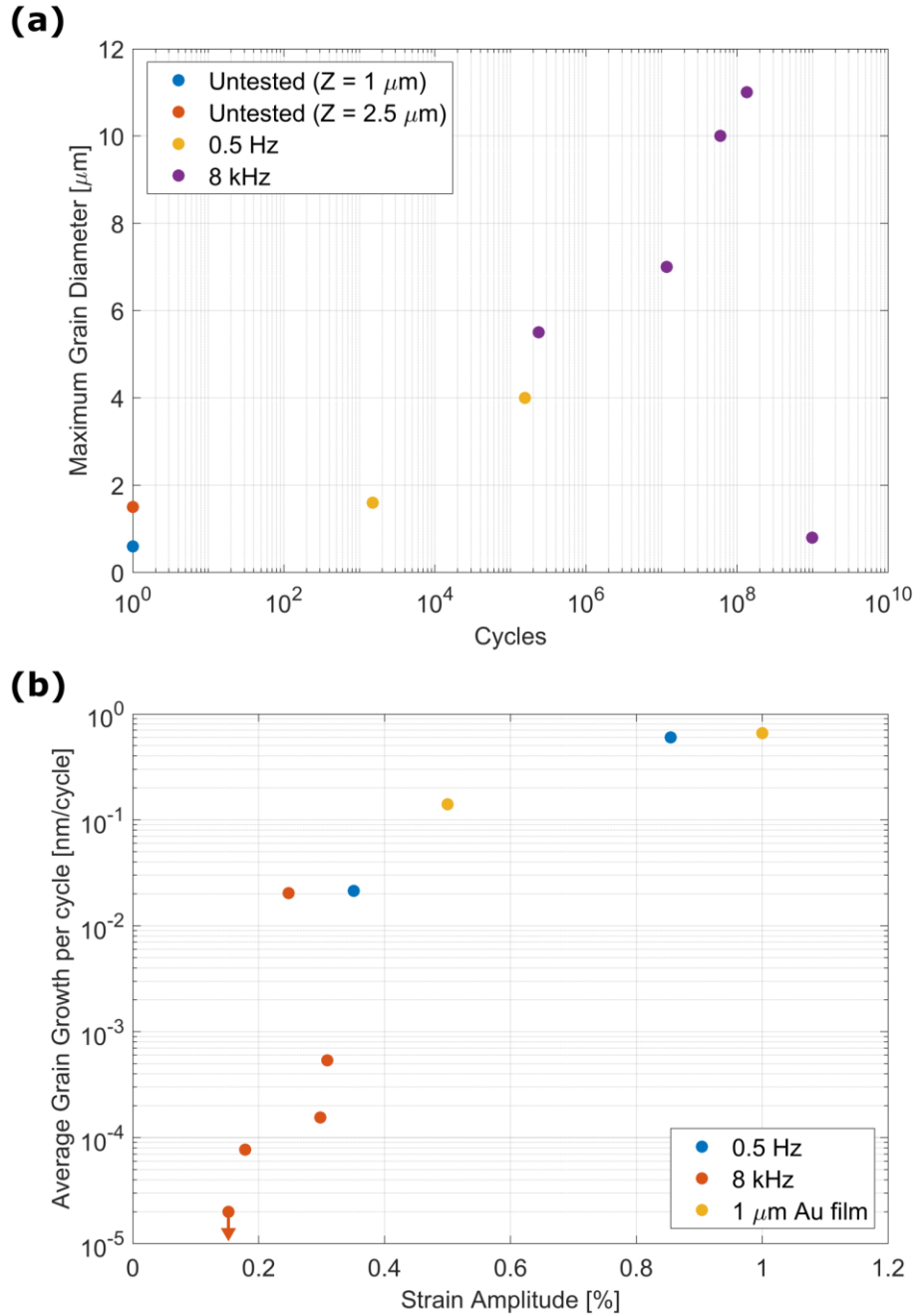
Figure 5.4 – (a) Maximum equivalent grain diameter as a function of applied cycles; (b) Average grain growth rate as a function of ε_a; data for the 1 µm Au film was taken from reference [65]

5.2 Microbeam Modeling and Results

The computational modeling efforts were performed by Ebiakpo Kakandar and Gustavo Castelluccio, our collaborators at Cranfield University. Along with the experimental results, modeling was essential for the study of driving forces and mechanisms for fatigue induced grain growth.

Crystal plasticity simulations were conducted on an equivalent microbeam with similar dimensions and an equiaxed randomly oriented ultrafine grained microstructure. Figure 5.5 shows the mean strain energy for each grain after loading. The orientation parameter 3Γ considers the miller indices of the orientations of each grain (according to Equation 5.1) with a value of 0 for (001) and a value of 1 for (111) orientations. The figure demonstrates that grains which have a closer orientation to the (001) orientation have, in average, lower strain energy densities. Considering that the grains that presented significant grain growth in this study are oriented more closely to the (001) orientation, these results exemplify that, in average, the reduction in strain energy is the driving force for grain coarsening. However, the data shown here present a great amount of scatter across all orientations which affects the overall interpretation of the results. Therefore, more detailed simulations are needed in order to investigate how the reduction in strain energy affects grain coarsening.

$$3\Gamma = 3 \times \frac{h^2 k^2 + l^2 k^2 + h^2 l^2}{(h^2 + k^2 + l^2)^2} \qquad \text{Equation 5.1}$$
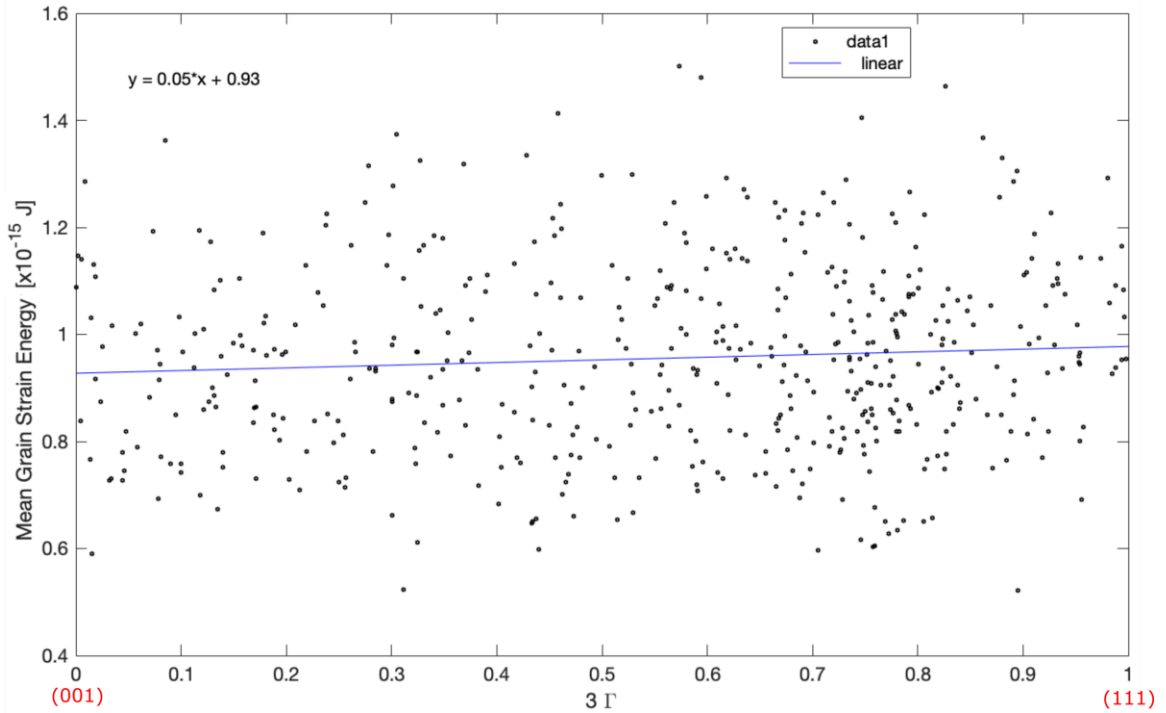
Figure 5.5 – Strain energy per grain versus orientation parameter 3Γ

With the EBSD data gathered from all slices of the microbeam (3D FIB-EBSD procedure), our collaborators were able to create a synthetic computational microbeam with the same microstructure using Dream 3D [66]. In this particular set of simulations, an individual slice of the bottom ultrafine grained region from two microbeams were studied. The models (example shown in Figure 5.6) were created in Abaqus with C3D8R elements with a single element through the thickness and dimensions of 0.35 µm x 0.35 µm x 1.5 µm, corresponding to the EBSD scans resolution and the height of the slice. The applied loadings were monotonic tensile deformations of 0.3% and, although different from the experimental loadings, they will allow for comparisons between an untested microbeam and a tested one with grain growth. Each element in the models were assigned Euler angles according to the EBSD scans data.
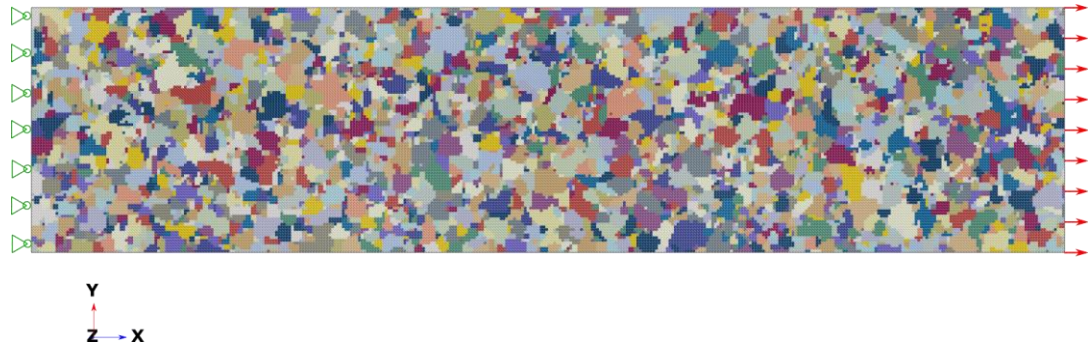
Figure 5.6 – Example of a finite element model reconstructed with Dream 3D from an EBSD scan of an untested microbeam

The two microbeams investigated were the untested microbeam and the one tested at $\varepsilon_a = 0.3$ % for 5.6×10^7 cycles (Figure 5.1c) with significant grain growth. Figure 5.7 shows the strain energy density calculated with simulations under the 0.3% tensile straining. Comparing Figure 5.7a (untested) with Figure 5.7b (tested at $\varepsilon_a = 0.3$ %), the larger grains that have grown at the edges of the microbeam in Figure 5.7b clearly exhibit lower strain energy densities. The mean strain energy density per element is $0.85 \times 10^6 \frac{J}{m^3}$ in the untested microstructure, while it decreases to $0.78 \times 10^6 \frac{J}{m^3}$ in the fatigued microstructure. Even though the simulations are not fully equivalent to the experiments due to the different loadings, they show that the driving force for grain growth is associated with an overall decrease in strain energy.
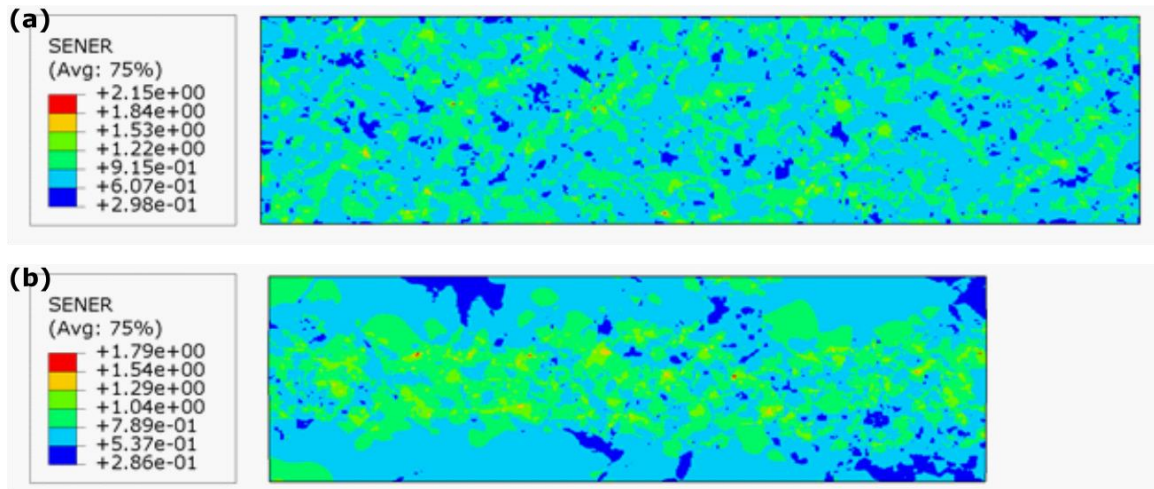
Figure 5.7 – Strain energy in 10^{-15} J computed under monotonic loading using EBSD reconstruction for (a) a sample without evident grain growth (b) a sample with significant grain growth.

Figure 5.8 presents the average strain energy density per grain as a function of the 2D equivalent grain diameter. Each dot represents the average IPF along the microbeam's length (IPF X) of each grain, while the dotted lines show the computed values of the strain energy density using single crystals simulations with three different orientations ((001), (011) and (111)) along the X direction, and a (001) orientation along the Z direction. The figure shows that as the grain size increases, the grains have lower mean strain energy densities, confirming that the driving force for grain coarsening is associated with the decrease in strain energy. The strain energy of the larger grains in the fatigue microstructure (Figure 5.8b) approaches the value found for the (001) single crystal which corresponds to the orientation with softest grains and lower strain energy [67]. However, the strain energy values seem to be slightly above the dotted line for (001) single crystal. Hence, the strain energy values do not reach the minimum value, and are consistent with the observation that the grains that exhibit grain growth are not perfectly orientated along the (001) orientation in the X direction (see Figure 5.1c, for example). Since grain growth requires a driving

force and kinetics for grain boundary mobility, the slightly higher strain energy level than the (001) orientation suggests that grains that grew have boundaries that are more mobile than boundaries in grain with the lowest strain energy levels. These results highlight that the abnormal grain growth with preferential direction along (001) is associated with the strain energy levels. However, the findings observed here were the result of only two simulations and, therefore, more simulations are needed in other slices of the microbeam to validate these findings and provide statistically significant conclusions.

Figure 5.9 and 5.10 show grain averages for the von Mises stress and maximum principal strain as a function of the equivalent grain diameter when the loading is applied. The stress values do not converge to a single value, showing that grain growth is not driven by stress. On the other hand, the strain values converge to a single value since the simulations are strain-controlled and larger grains only exhibit strains around that value (Figure 5.10b). Additionally, the strain distribution per grain is symmetric around that value.
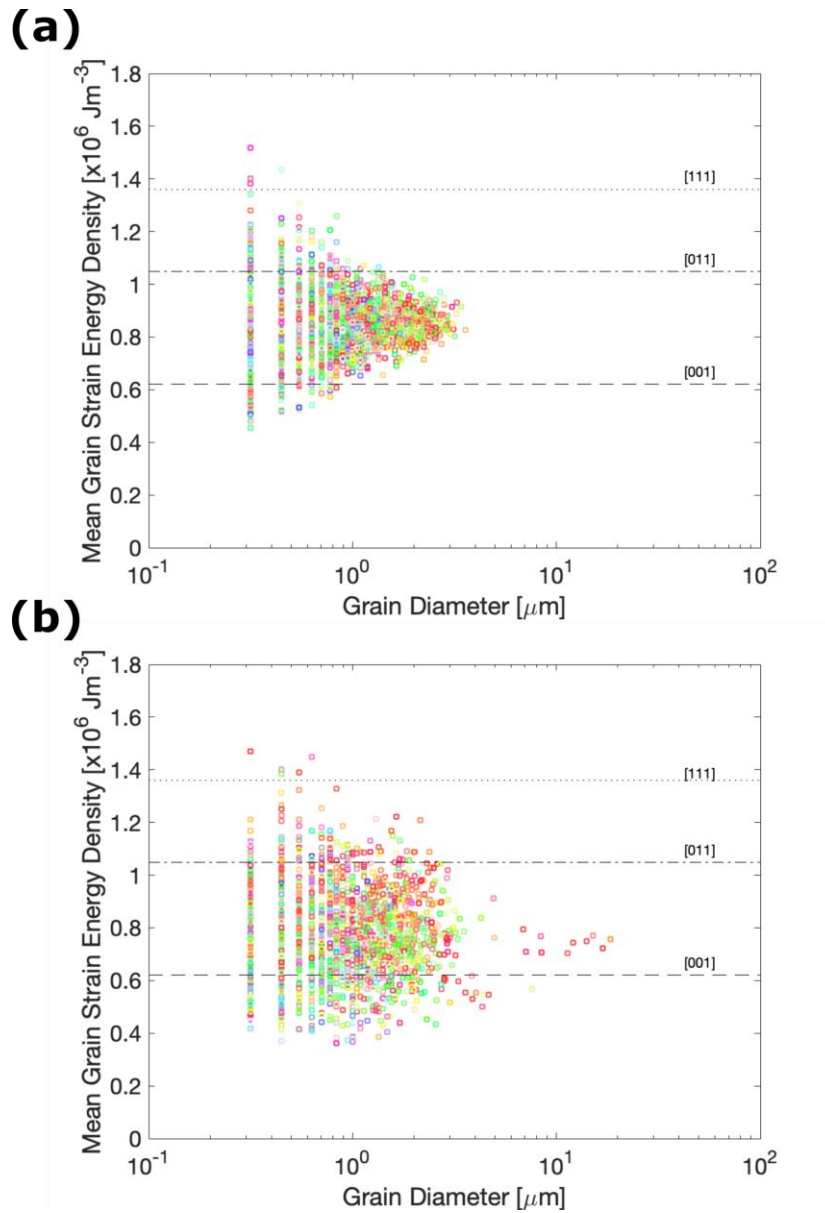
Figure 5.8 – Mean strain energy density per grain as a function of the grain size for (a) untested microbeam and (b) fatigued microbeam. Colors for each grain corresponds inverse pole figure orientation in the X direction

(a)

(b)
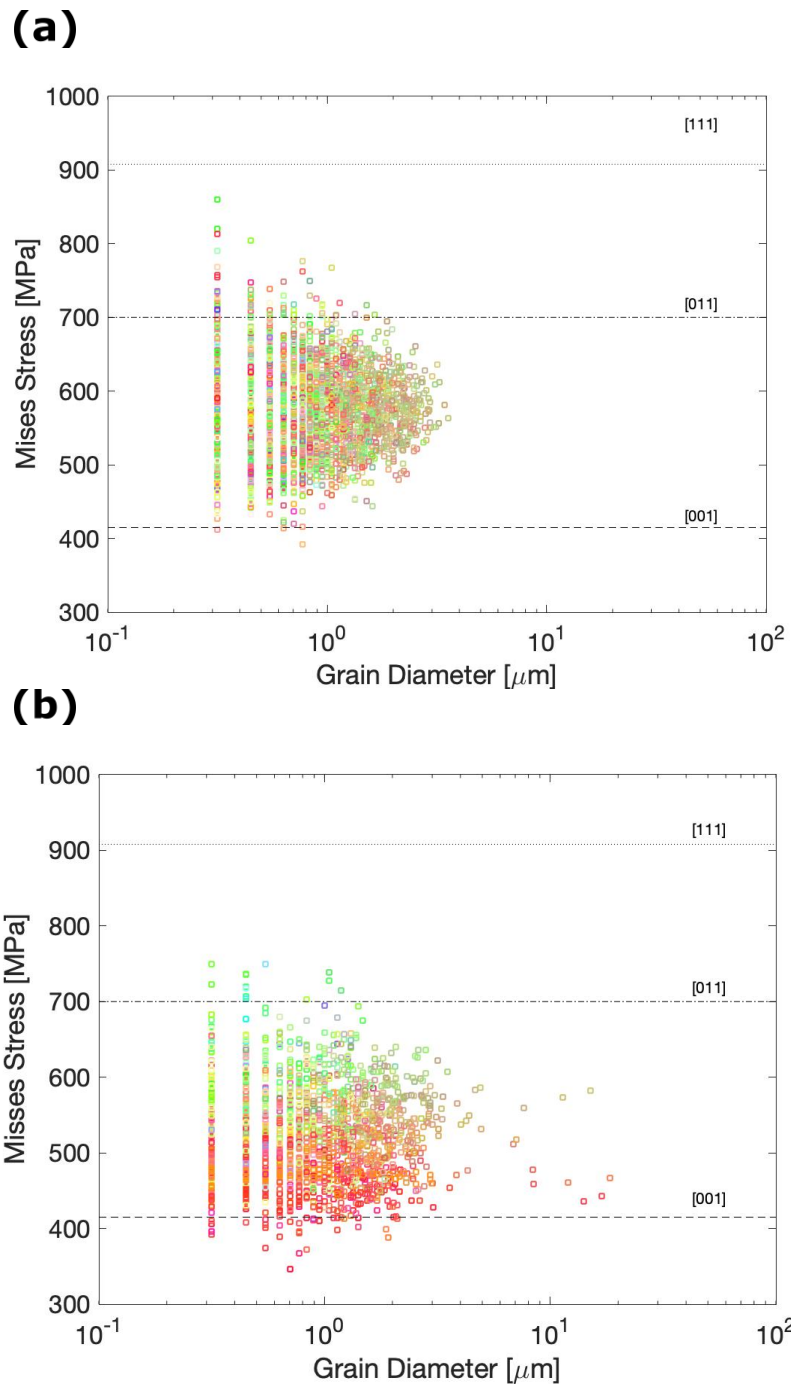
Figure 5.9 – Mean von Mises stress per grain as a function of the grain size for (a) untested microbeam and (b) fatigued microbeam

(a)

(b)
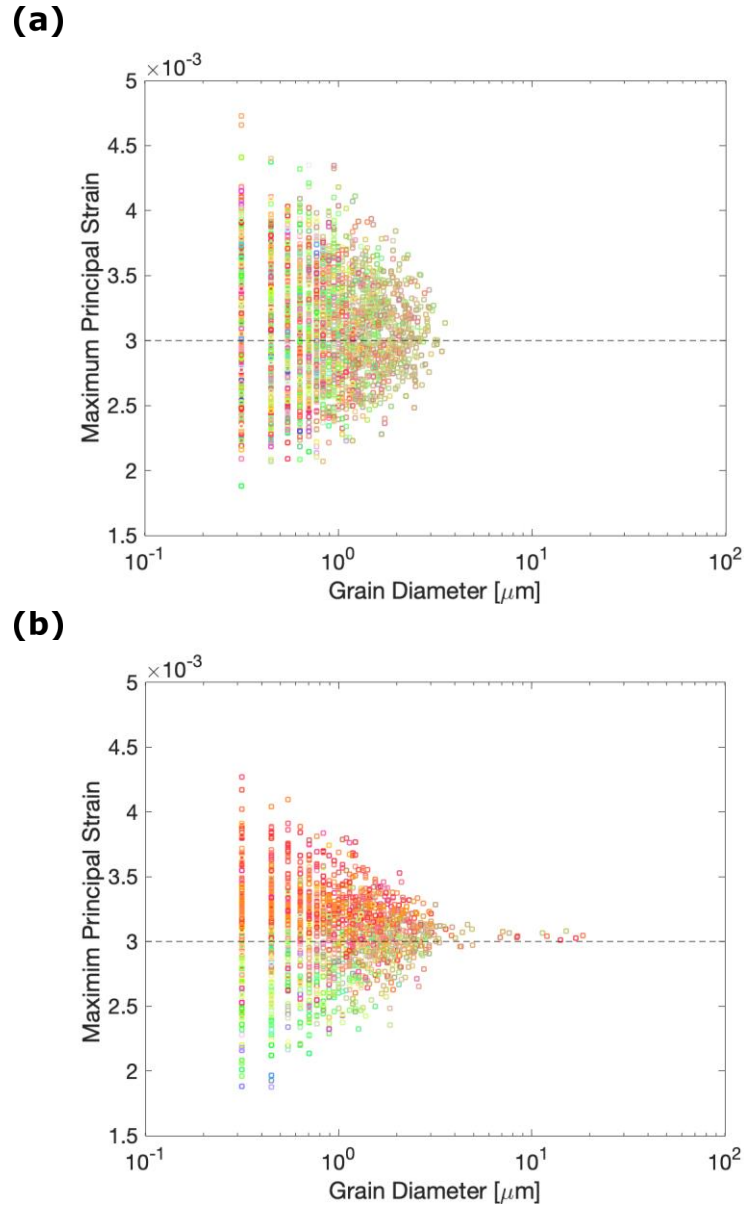
Figure 5.10 – Minimum principal strain per grain as a function of the grain size for (a) untested microbeam and (b) fatigued microbeam

5.3   EBSD Slices Across Width of Microbeam

The 3D FIB-EBSD procedure was also used to investigate grain size variation across the width of the microbeam. All slices and EBSD scans presented until this point were gathered from horizontal slices parallel to the top surface at distances Z from the bottom of the microbeam. In one particular microbeam tested at $\varepsilon_a = 0.28$ % for 1.8×10^8

cycles, the 3D FIB-EBSD procedure was performed with vertical slices parallel to the sidewall at different distances Y from the neutral axis of the microbeam. Figure 5.11 shows the fatigue damage on the sidewall just after the test was finished. The crack spans the whole thickness of the microbeam and has propagated along the top surface. In preparation for the EBSD procedure, the microbeam was attached to a micromanipulator and then was completely removed from its original position using FIB. The microbeam was rotated along its axis with the micromanipulator and placed on a flat surface of the microresonator's substrate with the sidewall face pointing upwards (Figure 5.11b). This orientation would allow for EBSD scans to be performed in order to observe the grain data along the sidewall, which was not possible in the original orientation of the microbeam. Figure 5.11c shows the locations of selected slices from the procedure. The distance Y is the height measured from the neutral axis (e.g. Y = 0 µm at the neutral axis and Y = ± 6 µm at the sidewalls).

Figure 5.12 shows the SEM images, the Band Contrast and the Inverse Pole Figure (IPF) in the in-plane direction along the beam's length (IPF X) of the selected slices shown in Figure 5.11c. Figure 5.12a of a slice close to the sidewall shows the clear grain growth in the bottom of the microbeam, with "pancaked" grains in the bottom 2 µm and columnar grains on the rest of the microbeam. The columnar grains in regions close to the crack that covers the whole thickness also appear to show grain growth, which was not observable using the previous orientations in the procedure. Figure 5.12b shows a slice very close to the neutral axis and is more representative of the original microstructure of an untested microbeam, with columnar grains and an ultra-fine-grained structure in the bottom 2 µm. Around the bottom middle of the figure, a couple of grains which have a grain size much larger than the neighboring grains are observed, and are a result of a small crack that

95

propagated past the neutral axis, as also observed in Figure 5.1c. Figure 5.12c shows a slice past the neutral axis and closer to the other sidewall. Grain growth can again be observed in the bottom regions of the microbeam. Observing all slices, the great majority of grains that show grain growth demonstrate an orientation close the (001) orientation in the X directions, highlighting again the abnormal grain growth with that preferential orientation.
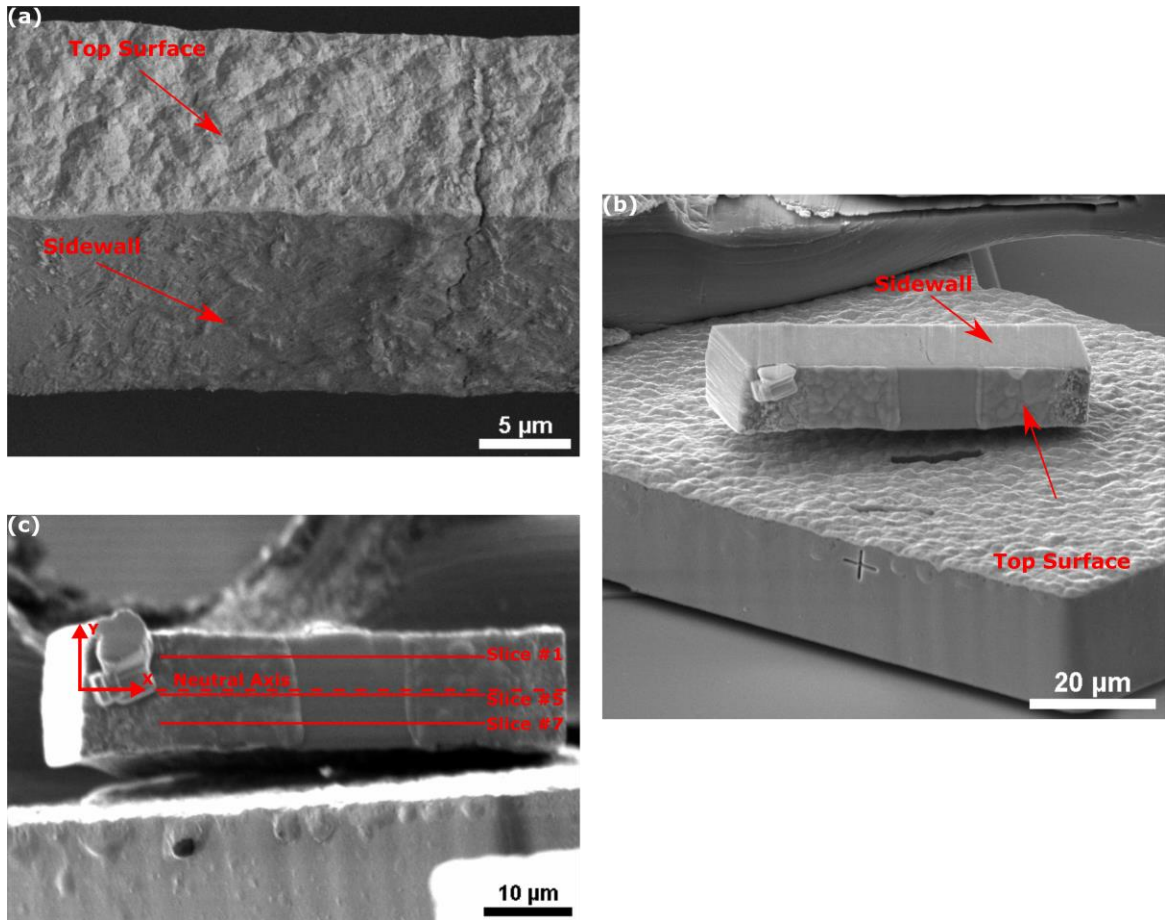
Figure 5.11 – (a) SEM *postmortem* images of microbeam tested at $\varepsilon_a = 0.28$ % for 1.8×10^8 cycles; (b) Microbeam after manipulation in preparation for EBSD; (c) Top surface of microbeam with location of selected slices
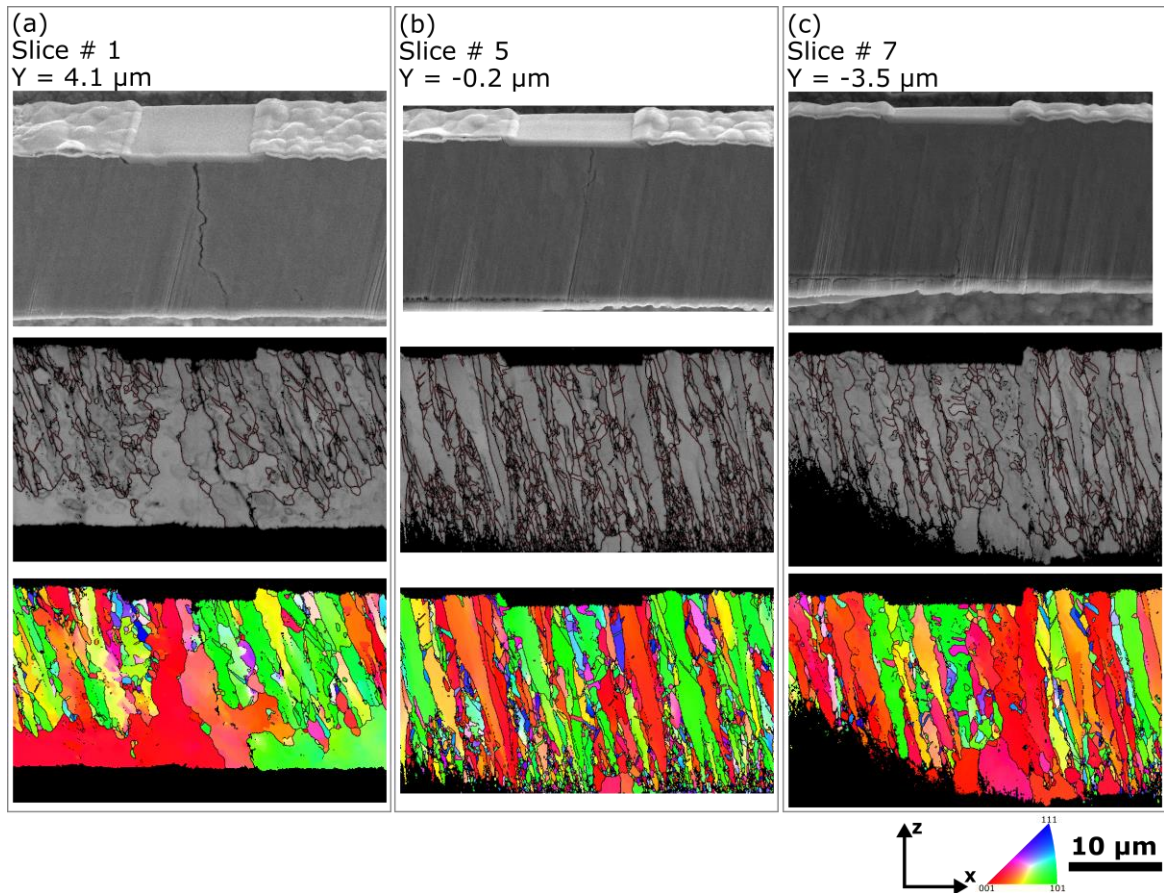
Figure 5.12 – (a)-(c) SEM, band contrast and IPF X images of selected slices of microbeam showing grain size variation along the width

5.4 Discussion

The coarsening of existing grains (grain growth) in metals can occur at large homologous temperatures and/or with deformation [68, 69]. The grain boundary migration rate depends on a thermodynamic driving force that reduces the total energy of the system and grain boundary mobility mechanisms that control the kinetics of the mobility [69]. Grain boundary curvature and the difference in strain energy between adjacent grains affect the likelihood of grain growth. Furthermore, strain-induced grain boundary migration may result from monotonic applied deformation or residual stresses. Large enough shear stresses are believed to control the nucleation and glide of grain boundary defects (shear

stress grain boundary migration), which can explain the observed grain growth at room temperature in nanocrystalline metals [70-73]. Accounting for grain boundary character (affecting mobility), elastic and plastic anisotropy, as well as grain-size-dependent plastic yielding can lead to a wide range of observed grain growth behaviors, including continuous and abnormal grain growth as well as texture formation [74, 75]. Numerical and atomistic models have also been very instrumental in understanding grain growth, especially under monotonic deformation [70, 75-77].

In comparison, much less is known about grain growth under cyclic loading. Only recently, researchers have starting reconsidering the common assumption that metals with micron sized grains would not undergo fatigue grain growth at low homologous temperatures. For instance, bulk ultrafine grained metals processed by severe plastic deformation undergo cyclic softening at room temperature, which is in part related to grain coarsening [63, 78, 79]. Similarly, ultrafine grained metallic thin films, deposited on polymer substrates, also undergo grain growth under cyclic loading [65, 80]. The accumulated plastic strain, instead of the plastic strain amplitude, is expected to play a significant role [63], but many details regarding the cyclic growth of these sub-micron grains are still missing [81]. More impressively, a recent study highlighted room temperature grain coarsening ahead of a fatigue crack [82] in an Al alloy with grain size between 12μm and 80μm. Hence, there is a notable lack of understanding of the driving forces and kinetic mechanisms responsible for the growth of grains in metallic materials under cyclic loading.

The experimental testing and microbeam characterization in this study have demonstrated that cyclic deformation can induce significant grain growth in electroplated

Ni with grains increasing by up to one order of magnitude in size. This study demonstrates that a larger deformation amplitude accelerates the grain growth as long as a minimum threshold deformation is applied. The computational analysis of an initial and fatigued microstructure has demonstrated that largest grains in the fatigued specimen have strain energy densities slightly above that of the (001) single crystal orientation, which corresponds to the minimum among all crystal orientations. The analysis supports that the strain energy density is a metric of the grain growth driving force rather than von Mises stress or maximum principal strains, especially given the fully reversed nature of the loading. Indeed, the strain energy density describes the thermodynamic likelihood for a grain to grow, although it does not provide any reference regarding the kinetics of the process.

The mechanisms controlling the kinetics of grain growth are certainly related to the cyclic character of the load since a monotonic loading at 0.18-0.85% strain levels is not expected to provide the same extent of grain growth. Hence, the continued (i.e. with cycling) irreversible emission of lattice dislocations is required to enable grain boundary mobility (for example via formation of grain boundary steps [65]) in addition to a favorable thermodynamic driving force. Figure 5.13 presents the maximum apparent Schmid factor computed for both microstructures as a function of grain diameter. These results demonstrate that the Schmid factor of the grains that grew are above 0.4, which is the value for the (001) crystal orientation. Hence, this proposes that plastic deformation, facilitated by higher Schmid factors, plays a key role in enabling fatigue induced grain growth. The actual orientation of the growing grains under cyclic loading result from the competition between maximizing the driving force and the grain growth mechanism. Because the

minimum strain energy density does not correspond to the maximum Schmid factor, the grains that grew have strain energy densities above the lowest possible value. This effect should be most noticeable at lower deformation amplitudes in which the emission of dislocations is more difficult and the maximization of the Schmid factor becomes a more dominant factor. It is also likely that the absence of grain growth at 0.15% is the consequence of having no plastic deformation occurring at this low strain level, thereby drastically reducing the grain boundary mobility, despite having a driving force for grain growth.

(a)

(b)
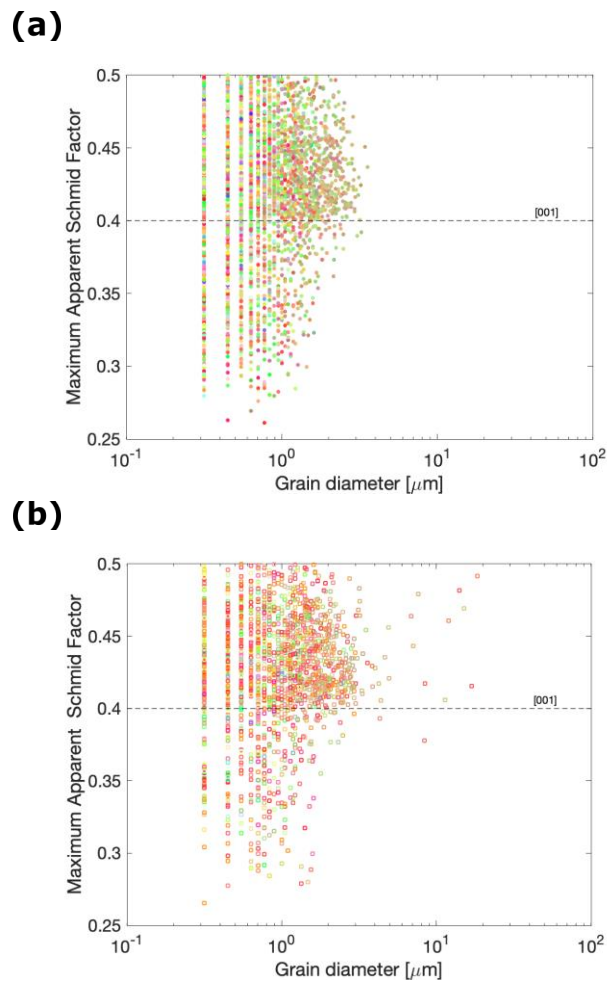
Figure 5.13 – Maximum apparent Schmid factor as a function of the grain size (a) a sample without evident grain growth (b) a sample with large grown grains. Dotted line corresponds to the (001) crystal with minimum strain energy

100

5.5   Conclusions

The combination of *postmortem* EBSD scans of fatigued microbeams and finite element modeling of reconstructed microstructures led to the following conclusions regarding fatigue-induced grain growth in ultrafine grained Ni with a strong initial (001) fiber texture:

1. Abnormal grain growth occurs for grains with a near (001) orientation in the beam length direction, as long as the applied ε_a exceeds 0.18%. No grain coarsening occurred for a microbeam tested at $\varepsilon_a = 0.15\%$ for 10^9 cycles.

2. The maximum equivalent grain diameter, which can exceed 10 µm (compared to a maximum of 1 µm for the initial microstructure) after 10^8 cycles at $\varepsilon_a \sim 0.2\text{-}0.3\%$, is dependent on the number of cycles, with clear evidence that grain growth continues to occur even after 10^7 cycles and no sign of any testing frequency dependence.

3. The average grain growth rate, calculated assuming a linear growth with cycles, increases with increasing ε_a, from $\sim 10^{-4}$ nm/cycle at $\varepsilon_a = 0.18\%$ to ~ 0.6 nm/cycle at 0.85%. These values agree with the data for other FCC metals on the literature.

4. The grains that grew, with preferential (001) orientation along the X direction, have lower strain energy densities than the average value for the initial microstructure, clearly confirming that a reduction in elastic strain energy is the main driving force for grain growth.

5. Interestingly, the strain energy density computed with simulations for grains that grew the most is slightly higher than the one for (001) single crystals, which is the lowest possible. This suggests that the kinetics of grain boundary migration may

also plays a role in the fatigue-induced grain growth process, and that the grains with the lowest strain energy density do not necessarily have the optimal boundary mobility under the fatigue loading conditions, although more detailed simulations are needed to validate these results.

6. The maximum apparent Schmid factor of the largest grains is higher than that of (001) single crystals and close to 0.5, which suggests that orientations that are preferentially oriented to promote plastic shear can enhance grain growth. It is consistent with the notion that lattice dislocations generated under cyclic deformation interact with grain boundaries to form steps, whose motion leads to grain boundary migration. The absence of any grain growth observed at $\varepsilon_a = 0.15\%$ is likely due to the absence of boundary steps generation at this low strain levels.

CHAPTER 6.   CONCLUSIONS AND FUTURE WORK

6.1   Conclusions

This dissertation studied the fatigue behavior of Ni microbeams under a range of conditions. The extreme stress gradients caused by bending loadings and the presence of microstructurally small cracks greatly influences the behavior of these Ni microbeams, deviating their behavior from the mostly well understood bulk Ni behavior. Characterizing and understanding the fatigue damage and mechanisms of metals under these size effects are of paramount importance since they are present in wide variety of MEMS and micrometer-scale structures. MEMS and micrometer-scale structure have seen increased uses in the past years with applications ranging from accelerometers to biotechnology sensors.

This work investigated the fatigue behavior and crack nucleation and propagation mechanisms in the HCF/VHCF regime, while also accessing environmental effects (comparison between air and vacuum environments), with a novel *in situ* SEM electrostatic technique. A new external actuation technique was developed in order to investigate fatigue behavior and mechanisms under the LCF regime, while also investigating frequency effects. Finally, fatigue-induced grain coarsening was observed in the ultrafine grained region of the microbeam and the combination of EBSD data with computational simulations allowed for the development of arguments for the driving force of grain growth.

Results from the *in situ* SEM technique for HCF/VHCF testing highlighted strong environmental effects on fatigue behavior. The air accelerates fatigue crack nucleation by

decreasing fatigue initiation life by at least one order of magnitude and the S-N curve shows fatigue lives that are three orders of magnitude longer in vacuum at the same stress/strain amplitudes. Ultraslow crack propagations rates of the order of 10^{-14} m/cycle in a vacuum and 10^{-12} m/cycle in air were found and are associated with a discontinuous process for crack growth. In fact, fractography results revealed that the fatigue crack nucleation and propagation are controlled by the formation of voids underneath extrusions or ahead of the crack tip. The air environment facilitates the formation of voids and, consequently, accelerates crack nucleation and propagation. The void dominated fatigue process is thought to be a consequence of the effects of extreme stress gradients in the microbeams, that greatly reduce the driving force for crack propagation. However, the limited amount of cyclic slip ahead of the crack tip still allows for vacancy nucleation, with subsequent formation of voids allowing the nucleation and propagation of fatigue cracks.

The study of the microbeam under the LCF regime highlight strong differences in fatigue behavior and mechanisms when comparing to the HCF/VCHF regime. In the LCF regime, fractography results show that the dominant fatigue mechanisms are the well-documented fatigue mechanisms characterized by larger crack growth rates (average of 10^{-8} m/cycle) and S-N behavior with $b = -0.078$ and $c = -0.57$ (in contrast with the S-N behavior in HCF/VHCF with $b = -0.038$ and $c = -0.30$). Results also highlight the lack of frequency effects in the fatigue behavior of Ni microbeams by comparing microbeams ran at similar strain/stress amplitude but ran at 8 kHz and 0.5 Hz. Additionally, the transition in governing mechanisms from void controlled to conventional mechanisms appears to be highly influenced by the size effects present in the microbeams.

Hence, these results showed that extreme stress gradients significantly reduce the driving force for crack growth, causing an unusual fatigue behavior and a void controlled fatigue mechanism in the HCF/VHCF regime. As the driving force is increased under higher applied strain amplitudes in the LCF regime, the fatigue behavior and mechanisms follow more closely the well documented conventional behavior and mechanisms, indicating a threshold in applied strain amplitude around 10^{-4} above which the effects of extreme stress gradients no longer influence the dominant fatigue mechanism.

Results from the fatigue-induce grain growth study showed abnormal grain growth in the originally ultrafine grained region of the microbeam for grains that are preferentially oriented along a near (001) direction along the microbeam's length. The average grain growth rates ranging from 10^{-4} to 1 nm/cycle are shown to increase as applied strain amplitude increases, as long as it is above a threshold of 0.18%. Computational simulations synthetic models of the same microstructure revealed that the reduction in elastic strain energy is the main driving force for grain coarsening. However, the strain energy density of the coarser grains does not reach the minimum values indicating the kinetics of grain boundary migration also plays a significant role in grain growth. Additionally, the apparent Schmid factor of the coarser grains tends to be larger suggesting that plastic deformation enables grain growth.

All of these results are expected to provide a better understanding of the fatigue behavior in micro and nano scale devices and therefore allow for a more robust design of these devices.

6.2   Recommendations for Future Work

The findings in this work revealed many insights into the particular fatigue behavior of small-scale metals under extreme stress gradients. However, the understanding and details of these findings can be further expanded by performing additional in-depth investigations. The following are recommendations for future research avenues:

- As investigated in the HCF/VHCF regime, the environmental effects can also be studied in detail in the LCF regime. The current micromechanical external actuation technique can be adapted to perform *in situ* SEM LCF fatigue tests. These tests would also provide further insights into how cracks and extrusions nucleate as cycling progresses under this regime. The environmental effects should not be as drastic as in the HCF/VHCF regime, based on the lower initiation fatigue lives, but would certainly provide more insights into the fatigue behavior and mechanisms of the microbeams

- In order to further characterize the two fatigue mechanisms presented in this study, transmission electron microscopy (TEM) lamellas of fatigue microbeams can be prepared, specially of regions around fatigue cracks. This would provide detailed observations of dislocation densities ahead of crack tips and/or regions around voids (in microbeam tested under HCF/VHCF). Comparisons could also be traced between samples tested in air and in vacuum. These observations would bring more understanding into how plasticity plays a role in the nucleation and propagation of cracks in these microbeams.

- The fatigue induced grain coarsening can be further studied under *in situ* SEM/EBSD fatigue tests. The top portion of the microbeam can be sectioned with

FIB, leaving only the region with ultrafine grained microstructure. A possible *in situ* SEM LCF technique could be adapted to account for the right EBSD orientations and observations could be made as the grains grow with increasing cycling, providing more insights into the mechanisms and kinetics for grain boundary migration.

- The integration of experiments with crystal plasticity modeling performed by collaborators at Cranfield University has proven to be very effective. This integration has been an ongoing work [83, 84], but with the great amount of data collected from experiments and characterization of the microbeam many comparisons can be traced between experiments and simulations. More specifically, the creation of synthetic microbeams with the same microstructure as the experimental sample will allow for one to one correlations between modeling and experiments.

REFERENCES

1. Zhang, G.P. and Z.G. Wang. *Fatigue of Small-Scale Metal Materials: From Micro-to Nano-Scale*. 2008. Springer Netherlands.

2. Licari, J.J. and D.W. Swanson, *Adhesive Bonding Processes*, in *Adhesives Technology for Electronic Applications (Second Edition)*, J.J. Licari and D.W. Swanson, Editors. 2011, William Andrew Publishing: Oxford. p. 143-216.

3. Spearing, S.M., *Materials issues in microelectromechanical systems (MEMS).* Acta Materialia, 2000. **48**(1): p. 179-196.

4. Krogstad, J.A., C. Keimel, and K.J. Hemker, *Emerging materials for microelectromechanical systems at elevated temperatures.* Journal of Materials Research, 2014. **29**(15): p. 1597-1608.

5. Connolley, T., P.E. McHugh, and M. Bruzzi, *A review of deformation and fatigue of metals at small size scales.* Fatigue & Fracture of Engineering Materials & Structures, 2005. **28**(12): p. 1119-1152.

6. Warnasch, A. and A. Killen. *Low cost, high G, Micro Electro-Mechanical Systems (MEMS), Inertial Measurements Unit (IMU) program*. 2002. Palm Springs, CA: Institute of Electrical and Electronics Engineers Inc.

7. Lotfi, A., et al. *Platinum Balanced Cantilever-based Thermal Conductivity Detector for Gas Chromatography Application*. in *2019 IEEE SENSORS*. 2019.

8. Sparks, D.R., M.I. Chia, and G.Q. Jiang, *Cyclic fatigue and creep of electroformed micromachines.* Sensors and Actuators, A: Physical, 2001. **95**(1): p. 61.

9. Boyce, B.L., J.R. Michael, and P.G. Kotula, *Fatigue of metallic microdevices and the role of fatigue-induced surface oxides.* Acta Materialia, 2004. **52**(6): p. 1609-1619.

10. Sim, G.-D., et al., *Nanotwinned metal MEMS films with unprecedented strength and stability.* Science Advances, 2017. **3**(6).

11. Cui, W., X. Huang, and F. Wang, *Current Understanding of Fatigue Mechanisms of Metals*, in *Towards a Unified Fatigue Life Prediction Method for Marine Structures*, W. Cui, X. Huang, and F. Wang, Editors. 2014, Springer: Berlin, Heidelberg. p. 31-68.

12. Suresh, S., *Fatigue of materials*. 2001: Cambridge University Press.

13. Dowling, N.E., *Mechanical behavior of materials : engineering methods for deformation, fracture, and fatigue*. 4th ed. ed. 2013, Boston: Pearson.

14.   Polak, J., *Mechanisms and kinetics of the early fatigue damage in crystalline materials.* Materials Science And Engineering A-Structural Materials Properties Microstructure And Processing, 2007. **468**: p. 33-39.

15.   Ritchie, R.O., *Mechanisms of fatigue-crack propagation in ductile and brittle solids.* International Journal of Fracture, 1999. **100**: p. 55-83.

16.   Hammouda, M.M., R.A. Smith, and K.J. Miller, *Elastic-Plastic Fracture-Mechanics for Initiation and Propagation of Notch Fatigue Cracks.* Fatigue of Engineering Materials and Structures, 1979. **2**(2): p. 139-154.

17.   Troshchenko, V.T. and L.A. Khamaza, *Fatigue limits of steels and stress gradient.* Strength of Materials, 2011. **43**(4): p. 417-425.

18.   Yang, Y., et al., *Nanoscale and submicron fatigue crack growth in nickel microbeams.* Acta Materialia, 2007. **55**(13): p. 4305-4315.

19.   Allameh, S.M., et al., *An investigation of fatigue in LIGA Ni MEMS thin films.* Materials Science and Engineering A, 2004. **371**(1-2): p. 256.

20.   Cho, H.S., et al., *Measured mechanical properties of LIGA Ni structures.* Sensors and Actuators, A: Physical, 2003. **103**(1-2): p. 59.

21.   Hanlon, T., Y.N. Kwon, and S. Suresh, *Grain size effects on the fatigue response of nanocrystalline metals.* Scripta Materialia, 2003. **49**(7): p. 675-680.

22.   Hanlon, T., E.D. Tabachnikova, and S. Suresh, *Fatigue behavior of nanocrystalline metals and alloys.* International Journal of Fatigue, 2005. **27**(10-12): p. 1147-1158.

23.   Sadeghi-Tohidi, F. and O.N. Pierron, *Extreme stress gradient effects on microstructural fatigue crack propagation rates in Ni microbeams.* Applied Physics Letters, 2015. **106**(20): p. 201904.

24.   Muhlstein, C.L., R.T. Howe, and R.O. Ritchie, *Fatigue of polycrystalline silicon for microelectromechanical system applications: crack growth and stability under resonant loading conditions.* Mechanics of Materials, 2004. **36**(1-2): p. 13-33.

25.   Miller, K.J., *The 2 thresholds of fatigue behavior.* Fatigue & Fracture of Engineering Materials & Structures, 1993. **16**(9): p. 931-939.

26.   Petit, J. and C. Sarrazin-Baudoux, *Some critical aspects of low rate fatigue crack propagation in metallic materials.* International Journal of Fatigue, 2010. **32**(6): p. 962-970.

27.   Rodopoulos, C.A. and E.R. de los Rios, *Theoretical analysis on the behaviour of short fatigue cracks.* International Journal of Fatigue, 2002. **24**(7): p. 719-724.

28.   Baumert, E.K. and O.N. Pierron, *Fatigue Degradation Properties of LIGA Ni Films Using Kilohertz Microresonators.* Journal of Microelectromechanical Systems, 2013. **22**(1): p. 16-25.

29.   Baumert, E.K., et al., *Fatigue-induced thick oxide formation and its role on fatigue crack initiation in Ni thin films at low temperatures.* Acta Materialia, 2014. **67**(0): p. 156-167.

30.   Sadeghi-Tohidi, F. and O.N. Pierron, *Extreme stress gradient effects on the fatigue behavior of Ni notched microbeams.* Acta Materialia, 2016. **106**: p. 388-400.

31.   Sadeghi-Tohidi, F. and O.N. Pierron, *Towards prediction of the fatigue life of Ni microbeams under extreme stress gradients.* Extreme Mechanics Letters, 2016. **9**: p. 97-107.

32.   Barrios, A., et al., *Quantitative in Situ SEM High Cycle Fatigue: The Critical Role of Oxygen on Nanoscale-Void-Controlled Nucleation and Propagation of Small Cracks in Ni Microbeams.* Nano Letters, 2018. **18**(4): p. 2595-2602.

33.   Cowen, A., et al., *MetalMUMPs Design Handbook.* 2002.

34.   Banovic, S.W., K. Barmak, and A.R. Marder, *Microstructural characterization and hardness of electrodeposited nickel coatings from a sulphamate bath.* Journal of Materials Science, 1998. **33**(3): p. 639-645.

35.   Godon, A., et al., *Characterization of electrodeposited nickel coatings from sulphamate electrolyte without additive.* Materials Characterization, 2011. **62**(2): p. 164-173.

36.   Pathak, S., et al., *Influence of lower current densities on the residual stress and structure of thick nickel electrodeposits.* Surface & Coatings Technology, 2011. **205**(12): p. 3651-3657.

37.   Savall, C., et al., *Influence of deposition parameters on microstructure and contamination of electrodeposited nickel coatings from additive-free sulphamate bath.* Surface & Coatings Technology, 2012. **206**(21): p. 4394-4402.

38.   Baumert, E.K. and O.N. Pierron, *Very high cycle fatigue crack initiation in electroplated Ni films under extreme stress gradients.* Scripta Materialia, 2012. **67**(1): p. 45-48.

39.   Gupta, S., et al., *Improved very high cycle bending fatigue behavior of Ni microbeams with Au coatings.* Acta Materialia, 2018. **161**: p. 444-455.

40.   Kettunen, P.O., et al., *Voids Produced by Fatigue in Copper Single-Crystals of (111)-Orientation.* Acta Metallurgica, 1981. **29**(6): p. 969-972.

41.   Grobstein, T.L., et al., *Fatigue Damage Accumulation in Nickel Prior to Crack Initiation.* Materials Science and Engineering a-Structural Materials Properties Microstructure and Processing, 1991. **138**(2): p. 191-203.

42.   Burger, S., et al., *A novel high-throughput fatigue testing method for metallic thin films.* Science and Technology of Advanced Materials, 2011. **12**(5): p. 7.

43.   Schwaiger, R. and O. Kraft, *High cycle fatigue of thin silver films investigated by dynamic microbeam deflection.* Scripta Materialia, 1999. **41**(8): p. 823-829.

44.   Schwaiger, R., G. Dehm, and O. Kraft, *Cyclic deformation of polycrystalline Cu film.* Philosophical Magazine, 2003. **83**(6): p. 693-710.

45.   Differt, K., U. Essmann, and H. Mughrabi, *A model of extrusions and intrusions in fatigued metals. 2. Surface roughening by random irreversible slip.* Philosophical Magazine a-Physics of Condensed Matter Structure Defects and Mechanical Properties, 1986. **54**(2): p. 237-258.

46.   Essmann, U., U. Gosele, and H. Mughrabi, *A model of extrusions and intrusions in fatigued metals. 1. Point-defect production and the growth of extrusions.* Philosophical Magazine a-Physics of Condensed Matter Structure Defects and Mechanical Properties, 1981. **44**(2): p. 405-426.

47.   Polak, J., *On the role of point-defects in fatigue crack initiation.* Materials Science and Engineering, 1987. **92**: p. 71-80.

48.   Hsiung, L.M. and N.S. Stoloff, *A Point-Defect Model for Fatigue Crack Initiation in Ni3al+B Single-Crystals.* Acta Metallurgica Et Materialia, 1990. **38**(6): p. 1191-1200.

49.   Mughrabi, H., *Cyclic Slip Irreversibilities and the Evolution of Fatigue Damage.* Metallurgical and Materials Transactions a-Physical Metallurgy and Materials Science, 2009. **40A**(6): p. 1257-1279.

50.   Man, J., et al., *Extrusions and intrusions in fatigued metals. Part 2. AFM and EBSD study of the early growth of extrusions and intrusions in 316L steel fatigued at room temperature.* Philosophical Magazine, 2009. **89**(16): p. 1337-1372.

51.   Lukas, P., et al., *Fatigue damage of ultrafine-grain copper in very-high cycle fatigue region.* Materials Science And Engineering A-Structural Materials Properties Microstructure And Processing, 2011. **528**(22-23): p. 7036-7040.

52.   Kunz, L., P. Lukas, and L. Navratilova, *Strain localization and fatigue crack initiation in ultrafine-grained copper in high- and giga-cycle region.* International Journal of Fatigue, 2014. **58**: p. 202-208.

53. Polak, J. and P. Liskutin, *Nucleation and short crack-growth in fatigued polycrystalline copper.* Fatigue & Fracture of Engineering Materials & Structures, 1990. **13**(2): p. 119-133.

54. Wood, W.A., *Formation of fatigue cracks.* Philosophical Magazine, 1958. **3**(31): p. 692-699.

55. Sriram, T.S., M.E. Fine, and Y.W. Chung, *The Application of Surface Science to Fatigue - The Role of Surface-Chemistry and Surface Modification in Fatigue Crack Initiation in Silver Single-Crystals.* Acta Metallurgica Et Materialia, 1992. **40**(10): p. 2769-2780.

56. Zinkle, S.J., et al., *Stability of Vacancy Clusters in Metals .2. Effect of Oxygen and Helium on Void Formation in Metals.* Philosophical Magazine a-Physics of Condensed Matter Structure Defects and Mechanical Properties, 1987. **55**(1): p. 127-140.

57. Zinkle, S.J. and E.H. Lee, *Effect of Oxygen on Vacancy Cluster Morphology in Metals.* Metallurgical Transactions a-Physical Metallurgy and Materials Science, 1990. **21**(5): p. 1037-1051.

58. Seitzman, L.E., et al., *The Effect of Oxygen on Void Stability in Nickel And Austenitic Steel.* Journal of Nuclear Materials, 1986. **141**: p. 738-742.

59. Seitzman, L.E., R.A. Dodd, and G.L. Kulcinski, *The Effect of Oxygen on Void Stability in Ion-Irradiated Steel.* Metallurgical Transactions a-Physical Metallurgy and Materials Science, 1990. **21**(7): p. 1839-1846.

60. Cawthorne, C. and E.J. Fulton, *Voids in Irradiated Stainless Steel.* Nature, 1967. **216**(5115): p. 576-+.

61. Aktaa, J., et al., *High cycle fatigue and fracture behavior of LIGA Nickel.* Scripta Materialia, 2005. **52**(12): p. 1217-1221.

62. Mughrabi, H., *Damage Mechanisms and Fatigue Lives: From the Low to the Very High Cycle Regime.* Procedia Engineering, 2013. **55**: p. 636-644.

63. Mughrabi, H. and H.W. Hoppel, *Cyclic deformation and fatigue properties of very fine-grained metals and alloys.* International Journal of Fatigue, 2010. **32**(9): p. 1413-1427.

64. Meirom, R.A., et al., *Fatigue-induced grain coarsening in nanocrystalline platinum films.* Acta Materialia, 2011. **59**(3): p. 1141-1149.

65. Glushko, O. and G. Dehm, *Initiation and stagnation of room temperature grain coarsening in cyclically strained gold films.* Acta Materialia, 2019. **169**: p. 99-108.

66. Groeber, M.A. and M.A. Jackson, *DREAM. 3D: A Digital Representation Environment for the Analysis of Microstructure in 3D.* Integrating Materials and Manufacturing Innovation, 2014. **3**(1): p. 17.

67. Zhang, Y., et al., *Lattice strains and diffraction elastic constants of cubic polycrystals.* Journal of the Mechanics and Physics of Solids, 2020. **138**: p. 103899.

68. Holm, E.A. and S.M. Foiles, *How Grain Growth Stops: A Mechanism for Grain-Growth Stagnation in Pure Materials.* Science, 2010. **328**(5982): p. 1138-1141.

69. Han, J., S.L. Thomas, and D.J. Srolovitz, *Grain-boundary kinetics: A unified approach.* Progress in Materials Science, 2018. **98**: p. 386-476.

70. Thomas, S.L., et al., *Reconciling grain growth and shear-coupled grain boundary migration.* Nature Communications, 2017. **8**: p. 12.

71. Chen, K.T., et al., *Grain boundary shear coupling is not a grain boundary property.* Acta Materialia, 2019. **167**: p. 241-247.

72. Gianola, D.S., et al., *Stress-assisted discontinuous grain growth and its effect on the deformation behavior of nanocrystalline aluminum thin films.* Acta Materialia, 2006. **54**(8): p. 2253-2263.

73. Rupert, T.J., et al., *Experimental Observations of Stress-Driven Grain Boundary Migration.* Science, 2009. **326**(5960): p. 1686-1690.

74. Sonnweber-Ribic, P., et al., *Kinetics and driving forces of abnormal grain growth in thin Cu films.* Acta Materialia, 2012. **60**(5): p. 2397-2406.

75. Battaile, C.C., et al., *Simulating grain growth in a deformed polycrystal by coupled finite-element and microstructure evolution modeling.* Metallurgical and Materials Transactions a-Physical Metallurgy and Materials Science, 2007. **38A**(10): p. 2513-2522.

76. Tonks, M. and P. Millett, *Phase field simulations of elastic deformation-driven grain growth in 2D copper polycrystals.* Materials Science and Engineering a-Structural Materials Properties Microstructure and Processing, 2011. **528**(12): p. 4086-4091.

77. Tonks, M., et al., *Analysis of the elastic strain energy driving force for grain boundary migration using phase field simulation.* Scripta Materialia, 2010. **63**(11): p. 1049-1052.

78. Hoppel, H.W., et al., *Microstructural study of the parameters governing coarsening and cyclic softening in fatigued ultrafine-grained copper.* Philosophical Magazine a-Physics of Condensed Matter Structure Defects and Mechanical Properties, 2002. **82**(9): p. 1781-1794.

79.   Hoppel, H.W., et al., *An overview: Fatigue behaviour of ultrafine-grained metals and alloys.* International Journal of Fatigue, 2006. **28**(9): p. 1001-1010.

80.   Glushko, O. and M.J. Cordill, *The driving force governing room temperature grain coarsening in thin gold films.* Scripta Materialia, 2017. **130**: p. 42-45.

81.   Kapp, M.W., et al., *Structural instabilities during cyclic loading of ultrafine-grained copper studied with micro bending experiments.* Acta Materialia, 2017. **125**: p. 351-358.

82.   Goswami, R., et al., *Fatigue-Assisted Grain Growth in Al Alloys.* Scientific Reports, 2017. **7**: p. 7.

83.   Kakandar, E., et al., *Computational and experimental study of crack initiation in statistical volume elements.* MATEC Web of Conferences, 2019. **300**: p. 10001.

84.   Kakandar, E., et al., *A computational and experimental comparison on the nucleation of fatigue cracks in statistical volume elements.* International Journal of Fatigue, 2020. **137**: p. 105633.